Computer Experiments on Electric Antenna Characteristics in Space Plasma Environment

by

Yohei MIYAKE

March 2009

Acknowledgments

I would like to express my sincere and hearty appreciation to Professor Yoshiharu Omura for his continual guidance and helpful suggestions throughout the present study. I am also grateful to him for providing important inspiration for future prospects of the present study.

I wish to express my deep and cordial appreciation to Dr. Hideyuki Usui for his continual support with fruitful discussions, reliable instructions, and encouragement for the present study. I am also grateful to his careful reading of most part of the present thesis and helpful suggestions for the revision.

I am deeply grateful to Dr. Hirotsugu Kojima for his helpful discussions and advices from the viewpoint of practical aspects of the plasma wave instrument (PWI) onboard scientific satellites. I would like to appreciate Professor Kozo Hashimoto for his critical and stimulating comments regarding antenna behavior in plasmas.

I am also grateful to Emeritus Professor Hiroshi Matsumoto (President of Kyoto Univ.) for attracting me to space radio science and for giving me the opportunity to perform computer-experimental study at Research Institute for Sustainable Humanosphere (RISH), Kyoto University.

I would like to express my acknowledgments to Dr. Naoki Shinohara, Professors Hiroshi Yamakawa and Shigeo Kawasaki for their encouragement and helpful advices on the present study. I also would like to thank Dr. Koichi Shin, Dr. Yoshikatsu Ueda, Dr. Tomohiko Mitani, and Dr. Takayuki Umeda for their helpful assistance in completing this thesis. I would like to thank Dr. Osamu Sakai at the Department of Electronic Science and Engineering and Dr. Tetsuji Matsuo at the Department of Electrical Engineering for their helpful suggestions for the revision of the present thesis.

I wish to express my appreciations to Dr. Keigo Ishisaka at Toyama Prefectural University and Dr. Lennart Åhlén at Swedish Institute of Space Physics for their fruitful discussions and comments for the study in Chapter 5.

I also wish to thank Ms. Michiyo Koyama, who is a secretary to Prof. Omura, and all secretaries in our research group for their office work and encouragement. Special thanks are due to discussions with my colleagues Mr. Masafumi Shoji and other students of the space plasma simulation group.

The computations in the present study were performed with the A-KDK system of RISH and HPC2500/M9000 of Academic Center for Computing and Media Studies at Kyoto University. The present study is supported in part by a Grant-in-Aid for Research Fellows from the Japan Society for the Promotion of Science (JSPS).

Finally, I thank my family Hiroyuki, Kei, and Kenta, and my fiancé Keiko for their continual encouragement and hearty support in my private life.

Abstract

An electric antenna commonly occupies an essential part in plasma wave instruments onboard scientific spacecraft. Though principles of electric antenna measurements are fundamental, antenna behavior modified under the influence of surrounding plasmas is often problematic, because it could disturb reliable measurements of an electric field component of plasma waves. Then, strong demands arise regarding a better understanding of antenna characteristics in space plasma environment. However, the antenna behavior in plasmas is often too formidable to evaluate quantitatively by means of theoretical approaches because of complex antenna–plasma interactions. Therefore, we must establish a numerical approach for the self-consistent analysis of antenna characteristics in space plasmas. This thesis is devoted to the development of a numerical method based on the Particle-In-Cell technique and the investigation of antenna characteristics in space plasma environment that is highly disturbed by the presence of an antenna and a spacecraft.

For the self-consistent analysis of antenna–plasma interactions, we construct a numerical simulation code based on an electromagnetic Particle-In-Cell description of the plasmas. The code can include inner boundaries corresponding to perfect conducing surfaces of an antenna and a spacecraft. At the boundaries, as well as perfect conducting conditions required for electromagnetic fields, we also introduce numerical treatments for the charge and current densities computed from plasma particles interacting with the boundaries. These treatments are necessary for accurate descriptions of the charge accumulation exactly on conducing surfaces and its redistribution to realize a floating equi-potential over the surfaces. By using the constructed code, we perform two basic tests regarding plasma environment around a conducting body. One is the plasma sheath formation as a result of the spacecraft charging. The other is the dispersion relation of a sheath wave, which is a peculiar electromagnetic-wave mode propagating only in an electron-sparse sheath. For both tests, the reproduced environments show a good agreement with results obtained by previous well-proven theories.

Using the code, we begin the antenna analysis in plasmas with a simple situation. First, we apply the code to the impedance calculation in a homogeneous plasma environment and compare the result with the conventional kinetic theory. We correctly confirmed characteristic impedance changes such as an impedance resonance and a finite resistance below the plasma frequency by the computer experiment. Next, we examined the impedance of an antenna surrounded by an ion sheath that is created simultaneously with the antenna charging. We found that the sheath mainly influences reactance values below the electron plasma frequency, which is consistent with empirical knowledge that the ion sheath functions as a capacitance in the low-frequency range. Meanwhile, when we expand the sheath thickness artificially by biasing the antenna potential negatively,

it is found that the sheath capacitance less contributes to the total antenna impedance. The trend indicates that the antenna reactance recovers its free-space value in the limit of large sheath dimensions, which corresponds to dilute and hot plasma environment as in the outer magnetosphere of the Earth.

As more realistic situations in space plasmas, we focus on effects of the photoelectron emission from sunlit surfaces of an antenna and a spacecraft. To illustrate the photoelectron effects, we perform computer experiments of the electron emission from inner boundaries corresponding to sunlit conducting surfaces. The emitted electrons have higher density but lower temperature than the plasma electrons. We confirmed the positive charging of the antenna and spacecraft bodies, and the formation of an electron-rich region in the vicinity of the sunlit surfaces. It is revealed from impedance calculation that the dense photoelectrons enhance the real part, and decrease the absolute value of the imaginary part, of antenna impedance at low frequencies. The antenna impedance in the photoelectron environment is represented by a parallel equivalent circuit consisting of a capacitance and a resistance. We also show that the above resistance can be well estimated semi-analytically using the numerical results of the electron currents flowing into and out of the antenna. This suggests that the impedance change is caused by the conduction current induced by the actual motion of photoelectrons contacting with the antenna surfaces. The results also imply that the impedance varies with the spin of the spacecraft, which causes the variation of the photoelectron density around the antenna.

Finally, we introduce a numerical technique for the direct analysis of receiving antenna behavior and also develop a new model of modern electric antennas toward future satellite missions. In the new analysis technique, we set up wave fields propagating in a computational space and simulate the process of wave reception by the antenna. By using the technique, we examined the effective length of a probe-like antenna, which has a configuration such that sensing wire elements are attached at both ends of a center boom conductor. For this type of the antenna, the effective length becomes shorter than the physical separation between the centers of two sensing elements. It is found that this effect is caused by the distortion of equi-potential surfaces due to the presence of the center boom conductor. We next introduce numerical models of guard electrode and current biasing, which are planned to be installed on future electric field instruments. We performed computer experiments by using the standard setting of electrode potentials, the values of which are not optimized but determined empirically. We found that the guard electrode decreases the photoelectron-current coupling of the sensor conductor with the boom and spacecraft bodies. The effect suggests that the electrode can reduce the influence of large amount of photoelectrons emitted by the spacecraft body on electric field measurements. On the other hand, the bias current draws the sensor potential

close to the background plasma potential. The electrode and the current biasing have a small effect on antenna behavior for oscillating fields created by external plasma waves, compared with their significant impacts on the static plasma environment. This result is understood from the voltage–current characteristic curve of the sensor, the gradient of which indicates the inverse of the dynamic resistance of the sensor for the oscillating fields. Meanwhile, the observed voltage–current curve is considerably deformed by the effect of the photoelectron current coupling even though it is decreased by the operation of the guard electrode. The result emphasizes the significance of more optimal electrode potentials in order to effectively mitigate the influence of the photoelectron coupling.

Contents

List of Figures

List of Tables

Chapter 1

General Introduction

1.1 Introduction

The electric antenna is the most fundamental device for radiating or receiving radio waves. It has been an essential component for humankind's radio communication on the Earth, and even in space. In space, however, the antenna has the second important application as the sensor of naturally occurring plasma waves. Space is filled with ionized gases called plasmas, and plentiful modes of waves naturally exist in plasmas [*Stix*, 1992]. Plasma waves contain much information about the dynamic nature of space plasmas, because the collective behavior of plasma particles are highly coupled with the wave electromagnetic fields through their self-consistent motion. In this sense, measurements of plasma waves provide the diagnosis of the plasmas themselves. Moreover, since the mean free path length of most space plasmas is far larger than a geophysical scale, only plasma waves can become mediators of energy exchange in the plasmas. This emphasizes the significance of plasma wave measurements.

The earliest study of plasma waves in geospace — the region of outer space near the Earth — goes back to ground-based observations of very-low-frequency (VLF) waves in late 1800s [*Preece*, 1894]. Since then, although extensive ground-based studies were conducted for VLF waves such as whistlers [*Preece*, 1894], dawn chorus [*Allcock*, 1957], and auroral hiss [*Burton and Boardman*, 1933]. Among them, *Storey* [1953] gave the first explanation for the whistlers that they are produced by lightning and their dispersion occurs during propagation along the Earth's magnetic field as a plasma wave mode. However, the exact emission mechanism for the other signals and the precise picture of the geospace environment remained largely unknown.

Rapid progress in the understanding of the geospace environment was brought by the space age, which started with the launch of the first satellites in late 1950s. Many scientific satellites and rockets revealed the exact structure of the Earth's magnetosphere, which is formed as a result of interactions between the Earth's geomagnetic field and the

solar wind. In such exploration, in-situ observations of plasma waves played a crucial role. The magnetosphere is divided by several characteristic regions and boundary layers, each of which contains plasmas with very different parameters from the other ones [*Lui*, 1987]. Since plasma waves are very sensitive to changes of the plasma parameters, each characteristic region has its own signature of plasma waves. Therefore, one can identify the distinct regions in the magnetosphere by satellite observations of plasma waves.

Further, the existence of localized plasma waves emphasizes the importance of in-situ observations. The first class of such waves is the electromagnetic ones such as the Auroral Kilometric Radiation [*Gurnett*, 1974] and the continuum radiation [e.g., *Gurnett and Shaw*, 1973], which are confined in specific regions in the Earth's magnetosphere and cannot reach the ground due to the presence of a dense ionospheric plasma. The second class is the electrostatic wave modes, which have only an electric component as a wave field [*Stix*, 1992]. The latter class of waves, in most cases, has much slower group velocity than that of electromagnetic waves and cannot propagate long distances. The wave modes can be found only by in-situ observations. The observations of such waves are important not only for the specification of characteristic regions but also for the study of the local wave–particle interactions occurring at the observation points.

One of breakthrough achievements of such plasma wave observations was brought by waveform measurements conducted by the GEOTAIL spacecraft, which was launched in 1992. In various regions of the Earth's magnetosphere, there commonly exists a strong wave emission called broadband electrostatic noise (BEN) extending over a broad frequency range, an example of whose dynamic spectra is shown in Figure 1.1(a). Although it had been believed that the BEN emission is a superposition of waves over a broad-frequency range, exhaustive theoretical studies in terms of linear analyses cannot provide a sufficient explanation for its broadband noise spectra. The GEOTAIL observations using a Wave Form Capture (WFC) [*Matsumoto et al.*, 1994a] revealed that the real nature of BEN is a series of solitary pulses as shown in Figure 1.1(b), which was named electrostatic solitary waves (ESW) [*Matsumoto et al.*, 1994b]. The successful observations of the ESW waveforms suggest that the nonlinear evolution of an electron beam instability is ubiquitously present in the magnetospheric environments. Stimulated by this achievement, many researchers have recognized the significance of direct measurements of waveforms in space plasmas, and such measurements have been actually carried out by many scientific spacecraft after GEOTAIL. Their concern now moves on how precisely and quantitatively the instruments can capture the real forms of the plasma waves.

For above in-situ plasma wave observations, an electric antenna has been commonly used for measurements of the electric component of the wave field. Particularly for electrostatic modes, an electric antenna is a unique instrument for the direct detection of the waves. Here, an essential issue arises regarding the use of an electric antenna, that is,

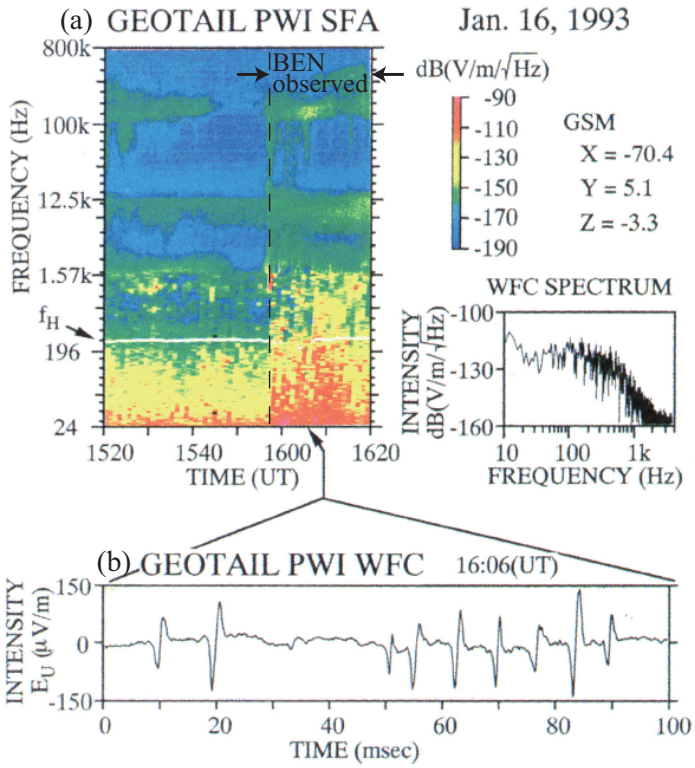

Figure 1.1: Example of (a) the dynamic spectra of BEN in the Plasma Sheet Boundary Layer and (b) its waveforms in the time domain captured by the GEOTAIL spacecraft [after *Matsumoto et al.*, 1994b].

whether or not the electric antenna immersed in space plasmas can behave equally with that on the ground. The answer is "no", because the performance of an electric antenna evidently depends on electric properties, i.e., the permittivity, of surrounding medium. However, the precise characteristics of practical electric antennas in space plasmas have not been sufficiently understood quantitatively so far due to interactions among antennas, plasma particles, and plasma waves. The major difficulty lies in the complex plasma environment much modified due to spacecraft–plasma interactions. Previously, there exist extensive theories for the antenna characteristics in plasmas [*Balmain*, 1964; *Schiff*, 1970]. Most of the theories, however, have introduced certain simplification in plasma modeling, and thus the result cannot be directly applied to realistic plasma environments, which are highly disturbed by the presence of the antenna itself and the spacecraft body. Moreover, the theories commonly treat only a very simple dipole antenna, but practical antennas which are actually onboard scientific spacecraft do not necessarily have such simple geometries.

The main objectives of the present work are the establishment of a numerical method for the quantitative analysis of electric antennas immersed in plasmas, and the investigation of antenna characteristics influenced by antenna–plasma (and spacecraft–plasma) in-

teractions. To illustrate the dynamics of plasma particles and the evolution of an antenna near field simultaneously, we performed computer experiments using the Particle-In-Cell and electromagnetic descriptions for plasmas and fields, respectively [*Birdsall and Langdon*, 1985]. This approach can provide rigorous and precise insight into antenna behavior in space plasmas. We believe that the present numerical study will contribute to more sophisticated design and calibration of electric field sensors onboard scientific satellites. In the following sections, we present some basic principles of electric field measurements in space plasmas, the advantages of the numerical approach, and the contribution of the present work.

1.2 Electric Antennas in Space Plasmas

As an introduction to electric antennas in space plasmas, we begin with a brief review of basic principles of plasma wave measurements with electric antennas. From the principles, we clarify two important antenna characteristics — the impedance and the effective length — in plasma wave measurements. Previously developed knowledge of these characteristics in plasmas is then reviewed briefly. Some limitations of previous theoretical and observational studies lead to the significance of computer experiments, which will be described in Section 1.3.

1.2.1 Basic Principles of Plasma Wave Measurement

Since early history of plasma wave measurements in space, dipole antennas have been commonly used on scientific spacecraft [*Barrington and Belrose*, 1963]. The term "dipole" in this context indicates a pair of conductive sensing elements extended from a center spacecraft. There are several types of actual geometries for the sensing elements. They are classified roughly into two groups: (a) cylindrical wire antennas and (b) spherical double probes. Figure 1.2 illustrates their geometries. For a cylindrical antenna, sensing elements are two cylinders extended from a spacecraft in opposite directions. Typical dimensions are 100 m in tip-to-tip length and 0.1–1 mm in radius. For a spherical double probe, sensing elements are two conducting spheres, which are located at the ends of booms extended from a spacecraft. Typical radius of the spheres is 1–10 cm. For both above, a differential amplifier finally provides an output signal as the voltage V_{out}, which is proportional to the voltage difference between the two sensing elements. In addition, for a spherical probe, pre-amplifiers are often mounted inside the spheres in order to provide low impedance signals to the differential amplifiers.

Practically, electric antennas actually onboard scientific spacecraft often have structures intermediate between the wire antenna and the spherical probe. Figure 1.3 shows the outline drawings of two kinds of actual electric antennas: (a) WANT and (b) PANT

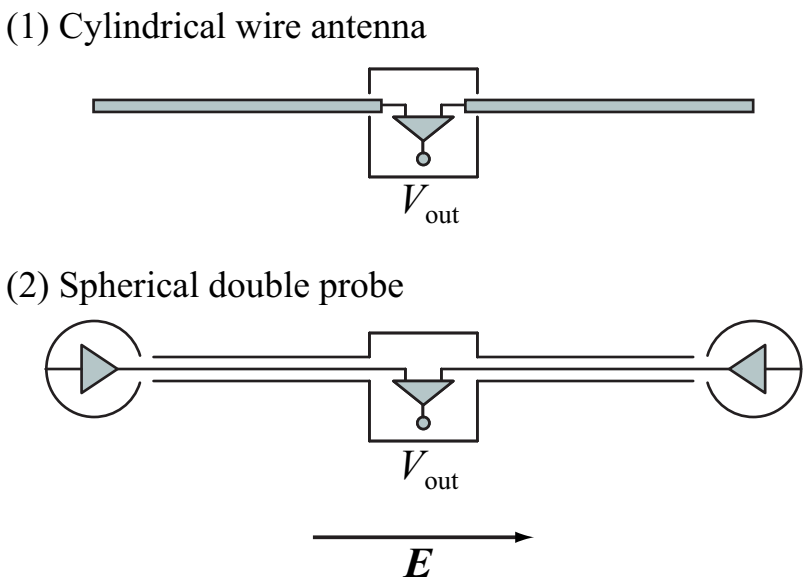

Figure 1.2: Schematic illustrations of a cylindrical wire antenna and a spherical double probe.

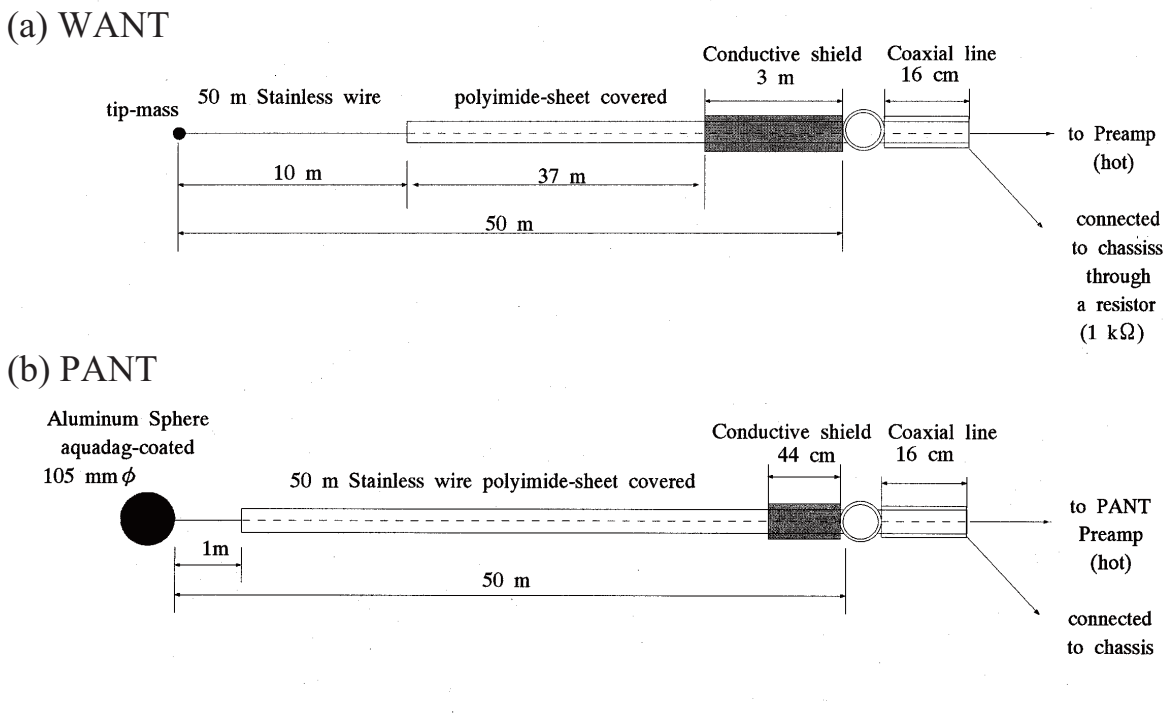

Figure 1.3: Schematic drawings of the (a) WANT and (b) PANT elements onboard the GEOTAIL spacecraft [after *Matsumoto et al.*, 1994a].

onboard GEOTAIL spacecraft, which are deployed orthogonal to each other. Although WANT and PANT are apparently similar to the wire antenna and the spherical probe, there are some differences from the antennas shown in Figure 1.2. First, for PANT, pre-amplifiers are not mounted inside the spherical probes, which indicates that the sup-

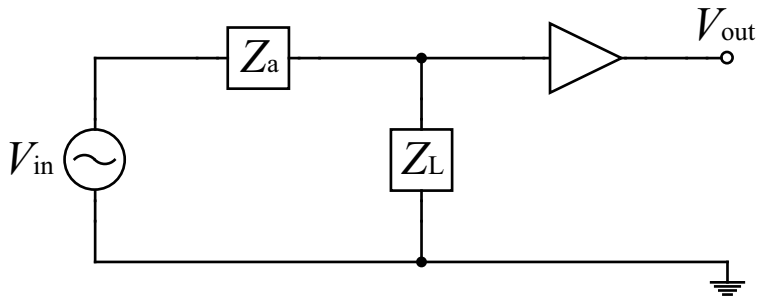

Figure 1.4: An equivalent circuit for electric field measurements using an electric antenna. V_{in} is the voltage induced by the applied electric field, Z_a is the antenna impedance and Z_L is the load impedance at the base of the antenna.

porting wires can also function as a part of sensing elements. Second, for both antennas, a portion of wires is covered with dielectric material. The dielectric coating is regarded as a capacitance separating the wires from ambient conducting plasmas. For DC electric field measurements, the coating completely insulates the wire from the ambient plasmas, and only an exposed portion can function as sensing elements. Thus as well as PANT, even WANT is considered to have probe-like behavior. Meanwhile, for higher frequencies, the capacitance appears almost short circuit. In the case, all the wire parts can function as sensing elements, and thus both WANT and PANT behave as wire antennas [*Imachi et al.*, 2002, 2007]. Thanks to this frequency-dependent behavior, both antennas can maintain an optimal sensitivity over a wide frequency range.

What we should next consider is how external electric field is related to the final output voltage V_{out}. This is characterized by two antenna characteristics, i.e., the effective length (or the "effective separation" in the case of a spherical probe) L_{eff} and the impedance Z_a. The effective length is defined as

$$L_{eff} = \frac{V_{in}}{E}, \tag{1.1}$$

where E is the electric field component along the antenna axis, and V_{in} is the open circuit voltage between the two sensing elements. This L_{eff} is generally different from the physical tip-to-tip length L_a of the antenna. The final output voltage V_{out} is then obtained by an equivalent measurement circuit shown in Figure 1.4. In the circuit, V_{in} is represented by a voltage source, and Z_a and Z_L represent the antenna impedance and the load impedance, respectively. In summary, the relation between V_{out} and E is written as

$$V_{out} = \frac{Z_L}{Z_a + Z_L} L_{eff} E. \tag{1.2}$$

From the above, it is obvious that precise knowledge of antenna effective length and impedance is essential to determine the quantitative relation between E and V_{out}.

Although the above basic principles are almost common with those for ground-based receiving antennas, there are also several differences from practical antennas on ground

such as the half-wave dipole. First, a space-based antenna is in most cases designed and actually operates as an "electrically short antenna", by which we indicate that its physical length is much shorter than, at least, the wavelength of free-space electromagnetic waves. For such a short antenna, the electric field is approximately uniform within a spatial scale of the antenna physical length, and thus the field is well described by a scalar electric potential [*Balmain*, 1964]. Note that electrostatic plasma waves can sometimes have very short wavelengths, which are comparable or shorter even compared with such a short antenna. In the situation, the antenna response to the field troublingly deviates from the long wavelength limit, which will be briefly mentioned later. The second difference from the ground-based antennas is that the space-based antenna typically operates by connecting very large Z_{L} rather than trying to achieve impedance matching. This comes from a difficulty of such matching for the space-based antennas and a design concept that gives priority to maximize the output voltage V_{out} delivered to pre-amplifiers rather than to the effective use of available power from received plasma waves.

The above differences are important key points in the design of electric antennas for plasma wave measurements. By taking the differences into consideration, we can regard the space-based dipole antenna rather as a voltmeter than as a radio antenna. Then, we can consider ideal voltmeter conditions as follows: (1) the electric field to be measured can be completely represented by a scalar potential; (2) two conducting elements, electrically insulated with each other, are floating in terms of the electric potential and have the same potentials as the local background potentials at their centers; (3) the potential difference between the two elements is directly obtained as the output voltage V_{out}. Also in practice, many electric field sensors, particularly spherical probes, are designed to meet the ideal voltmeter conditions as near as possible. However, the conditions are often violated unfortunately. The first reason is that an electrically short antenna has a large capacitance compared with a half-wave dipole. This indicates that it is usually difficult to achieve a condition $Z_{\mathrm{L}} \gg Z_{\mathrm{a}}$, which inhibits to meet the conditions (2) and (3). The change of the antenna characteristics in plasma environment also influences the conditions. In the following sections, we briefly review previous knowledge of antenna characteristics in plasmas.

1.2.2 Antenna Impedance

There are extensive theoretical and experimental studies regarding the antenna impedance in plasmas. Stimulated by a pioneering work by *Balmain* [1964], many researchers have attempted theoretical formulation based on the induced Electro-Motive-Force (EMF) method. In the method, the plasma contribution is entirely included in the plasma dielectric tensor as a function of frequency and wavenumber [*Stix*, 1992]. Various plasma models have been developed such as a cold plasma description [*Balmain*, 1964; *Oya*, 1965;

Aso, 1973], a hydrodynamic description with finite temperature [*Balmain*, 1965; *Meyer and Vernet*, 1974], and a kinetic (Vlasov) description [*Kuehl*, 1966; *Schiff*, 1970; *Nakatani and Kuehl*, 1976; *Meyer-Vernet and Perche*, 1989]. These models were applied to the impedance analysis mostly for an electrically short dipole antenna.

The most notable product obtained in the above studies is the prediction of impedance resonances occurring at plasma characteristic frequencies. This can be easily demonstrated for the simplest case of a cold, isotropic, collisionless plasma with an assumption of immobile ions. In free space, a short dipole antenna is purely capacitive; we can write its impedance as $Z = 1/j\omega C_0$, where j, ω, and C_0 denotes the imaginary unit, the angular frequency, and the free-space capacitance, respectively. In a plasma to be considered, on the other hand, the free-space capacitance should change to $\epsilon_{\rm r} C_0$, where $\epsilon_{\rm r} = 1 - \omega_{\rm pe}^2/\omega^2$ is the relative permittivity including the plasma contribution, and $\omega_{\rm pe}$ is the electron plasma frequency. The resultant impedance is then given as

$$Z = \frac{1}{j\omega C_0 + \frac{1}{j\omega L_{\rm e}}}, \tag{1.3}$$

where $L_{\rm e} = 1/\omega_{\rm pe}^2 C_0$ has a dimension of inductance. Equation (1.3) clearly indicates that the impedance shows the $L_{\rm e}C_0$ parallel resonance at the frequency $\omega = 1/\sqrt{L_{\rm e}C_0} = \omega_{\rm pe}$.

The signature of the resonance is modified for different plasma conditions and models; e.g., for anisotropic plasmas, the impedance resonance takes place at the upper hybrid frequency $\omega_{\rm UHR}$ instead of the electron plasma frequency. The knowledge about the impedance resonance has contributed to diagnostic techniques of space plasmas such as the impedance probe [*Oya*, 1966], which is widely used for electron density measurements in the ionosphere. In addition to the impedance resonance, the kinetic analysis predicted the finite resistance caused by dissipation of field energy due to its conversion to plasma kinetic energy [*Meyer-Vernet and Perche*, 1989]. This result was also applied to a diagnostic technique for plasma temperature measurements, which is called the quasi-thermal noise spectroscopy [*Meyer-Vernet et al.*, 1998].

In parallel with the theoretical studies, in-space measurements of antenna impedance have also been performed by several scientific spacecraft [*Hashimoto et al.*, 1991; *Tsutsui et al.*, 1997] and rockets [e.g., *Wakabayashi and Ono*, 2006]. As for the impedance resonance mentioned above, many sounding rockets obtained the frequency characteristic of the impedance in a frequency range near $\omega_{\rm UHR}$ in the ionosphere. They observed not only the resonance at $\omega_{\rm UHR}$ but also a sheath resonance, which is considered as a series resonance caused by the plasma inductance and the sheath capacitance [*Oya and Obayashi*, 1966]. Such resonances have been observed in various plasma environments such that the antenna length is sufficiently longer than the local Debye length.

On the other hand, in large part of the Earth's outer magnetosphere, the plasma is so dilute that the Debye length is often comparable to or even larger than the antenna

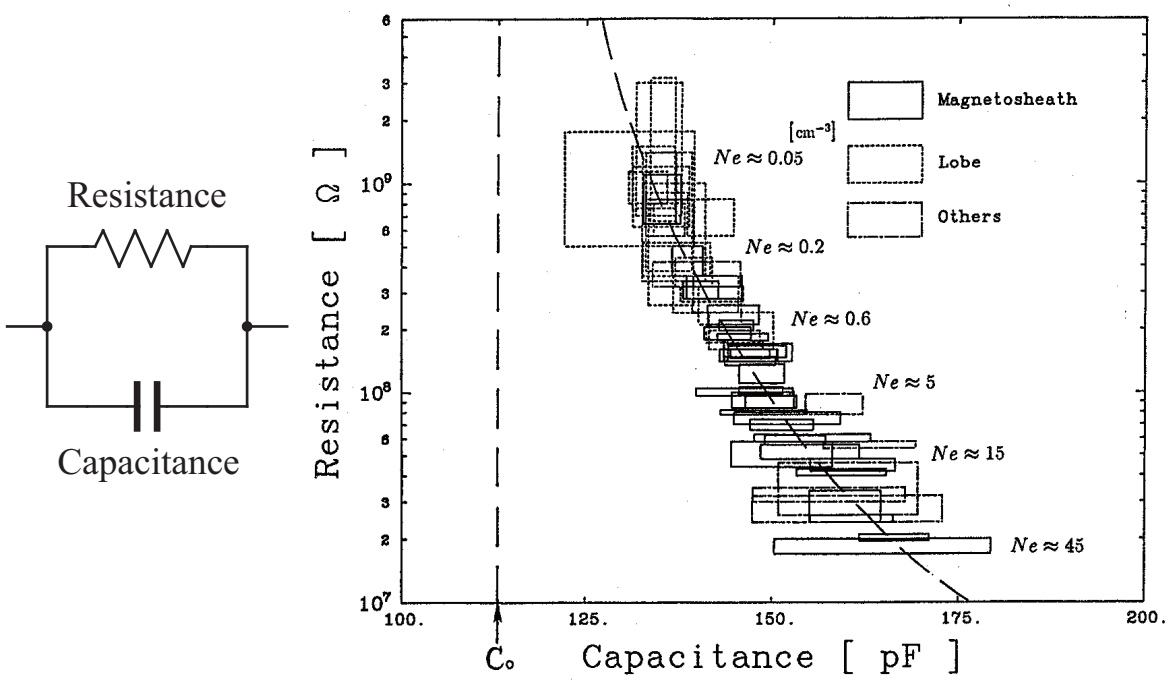

Figure 1.5: A quantitative relation between the resistance and capacitance values represented by a parallel circuit shown in the left panel, which is derived from WANT impedance measured by the 65 experiments conducted by the GEOTAIL spacecraft in the Earth's magnetosphere. The height and width between the facing sides of rectangle indicate fluctuation ranges of the resistance and capacitance values, respectively. The capacitance C_0, which is shown by the vertical dashed line, is the theoretical value for a linear dipole antenna with half-length of 50 m in free space [after *Tsutsui et al.*, 1997].

length. In such regions, the impedance resonance was hardly observed around the electron plasma frequency. Instead, the different characteristic signature was observed in lower frequency ranges [*Tsutsui et al.*, 1997], which was found to form an equivalent electric circuit consisting of a resistance and a capacitance connected in parallel. They calculated the resistance and capacitance values in various regions of the magnetosphere, the result of which is shown in Figure 1.5. As shown in the figure, they showed that especially the resistance value is strongly dependent on the change in the ambient plasma density. The GEOTAIL impedance measurements also obtained some data which implied that photoelectrons, emitted from sunlit conducting surfaces of the antenna and the spacecraft body, also influence the resistance value. Empirical knowledge about the antenna impedance in the dilute plasma environments significantly contributes to practical scenes of observation data processing; e.g., the calibration of the waveforms observed by the antenna is sometimes performed by using the representative values of the antenna impedance for each region of the outer magnetosphere [*Kojima*, 1998].

Although the extensive studies have been performed on the antenna impedance in plasmas by the theoretical and experimental approaches, some problems have remained

unresolved. For the analytical approach using the EMF method, main problems come from the need to (1) assume the current distribution on the antenna surface, and (2) describe the plasma contribution in the form of a dielectric function. Of them, the determination of the current distribution is a boundary value problem, and the problem becomes too complex to solve analytically for antennas with arbitrary lengths. This difficulty limits the analysis only to an electrically short antenna. There are a few studies which did not limit the analysis object to a short one in a case of cold plasma [*Adachi et al.*, 1977]. Also, several attempts have been conducted recently to directly derive a real form of the current distribution [e.g., *Bell*, 2006]. However, there have been still few approaches that can be applied to general plasma environments including kinetic effects.

The necessity to describe the plasma contribution as the dielectric function of frequency and wavenumber makes difficult to treat the inhomogeneous plasma environment around the antenna, because the ability to write in this form stems essentially from an assumption that the plasma is homogeneous in space [*Stix*, 1992]. In practical situations, however, the inhomogeneity of plasma environment is always important when considering the antenna characteristics. Even in absence of any active particle emission from an antenna surface such as the photoemission, an electron-sparse region called an ion sheath is created as a result of the antenna charging. In an aspect of the ion sheath effect on the antenna impedance, several theoretical analyses of the sheath impedance have been carried out for much simplified sheath configuration such as planar [*Oya*, 1965; *Balmain and Oksiutik*, 1969] and cylindrical [*Aso*, 1973] structures with a cold plasma description. However, in reality, the sheath configuration should be determined as a result of antenna–plasma interactions governed by the plasma kinetics, which is essentially inconsistent with the assumption of a cold plasma. Further, in the outer magnetosphere, photoelectrons emitted by the exposure of the antenna surface to the sunlight radiation form the dominant population of electrons around the antenna. The plasma inhomogeneity caused by photoelectrons is much more complex than that of the ion sheath because of their asymmetric emission and their attraction/repelling by the charged antenna body. Therefore, there are few studies that include effects of photoelectrons in the analysis of the antenna impedance in a self-consistent manner.

On the other hand, in-space measurements provide quite practical information about the impedance. The obtained data automatically contain effects that are difficult to treat theoretically. A difficulty of the in-space measurements lies in their high cost and inability to investigate every region and situation possibly encountered in space.

1.2.3 Effective Length

In comparison with the antenna impedance, a smaller number of studies have been performed regarding the effective length in plasma environments. Therefore, knowledge for

the effective length in free space is still used also for space-based antennas.

In free space, the effective length of a receiving antenna is usually analyzed by using the reciprocity theorem [*Jordan*, 1950], i.e., the receiving properties can be obtained by inversely analyzing its radiation properties. For a cylindrical dipole antenna that is an electrically short, it is widely known that the current distribution along the antenna is well approximated to a triangular form in a free-space case. This triangular current distribution is easily transformed to a uniform charge distribution by using the continuity equation for charge (and an initial condition that no charge is distributed before the antenna excitation). Since the centers of the charge distributions along the two antenna elements are located just at the centers of the elements, it is obvious that the equivalent dipole moment is realized by separating the charges by a distance of $L_a/2$. As a result, the effective length of the cylindrical wire dipole is $L_a/2$. The same logic can be applied to a spherical double probe. For the probe, charges on its sensing elements are obviously concentrated at the probe positions, which are separated by the distance L_a. This follows that the effective length of the spherical double probe is L_a.

Although the above idea well meets the ideal voltmeter condition (2), there are several works which reconsidered the effective length in space. *Imachi* [2007] focused on an effect of a dielectric coating of the GEOTAIL antennas by performing the rheometry experiments. He reported that $L_{\rm eff}$ of the wire antenna becomes frequency-dependent due to the separation of the antenna bodies from the conducting plasma medium; $L_{\rm eff} = L_a/2$ for high frequencies and $L_{\rm eff} = L_a$ for DC and low frequencies. The result comes from that the equivalent capacitance of the coating appears an open circuit for high frequencies, while a short circuit for DC and low frequencies, as described in Section 1.2.2.

Fuselier and Gurnett [1984] reported a peculiar effect on $L_{\rm eff}$ for short-wavelength electrostatic waves. In cases of comparable or shorter wavelength compared with antenna length, the electric field around the antenna is no longer uniform, and then $L_{\rm eff}$ deviates considerably from the free-space values. They reported that, in such a short-wavelength regime, $L_{\rm eff}$ shows a drastic dependence on the wavelengths [see also *Gurnett*, 1998, Figure 9]. This implies the difficulty in use of electric antennas for measurements of such short-wavelength waves. Although actual wavelengths are unknown in usual situations, space-based antennas are basically designed assuming that observed waves have sufficiently longer wavelength than the antenna length.

As another effect in plasma environment, it has been reported that $L_{\rm eff}$ becomes much larger than even its physical length for plasma waves propagating near the resonance cone [*Sonwalkar and Inan*, 1986; *James*, 2000; *Chugunov*, 2006]. However, to our best knowledge, there are few methods that can be generally applicable to the analysis of such irregular behavior of the effective length.

1.3 Significance of Computer Experiments

1.3.1 Role of Computer Experiments

Although the past theoretical and experimental studies significantly contributed to the understanding of basic antenna behavior in plasmas, certain difficulties remained in the directly application of the studies to practical electric field instruments onboard scientific spacecraft. Below, we again summarize limitations included in the theories.

1. In the impedance calculation using the EMF method, an assumption of a triangular current distribution on the dipole antenna surface has been commonly used to avoid the complexity of deriving the real form of the distribution.

2. Effects of plasma inhomogeneity caused by the sheath formation and the photoelectron emission around the antenna have been often neglected, or introduced in a limited way assuming a highly simplified plasma distribution.

3. The analyses have been limited only to a simple dipole antenna. Also, effects of a spacecraft body and other complex structures have been hardly introduced in the analyses.

In order to overcome these difficulties, we should explore possibilities of the utilization of numerical approaches.

Recent progress of computer facilities has enabled us to analyze antenna behavior in plasmas by means of a "computer experiment" (or a "computer simulation"). The basic idea of computer experiments is to simulate the physical behavior of antennas in complex plasma environments by discretizing the problem so that the complicated natural systems can be solved with an appropriate set of fundamental mathematical equations. The computer experiments can treat effects of inhomogeneity, lack of symmetry, and nonlinearity, and complement the limitations of the theories mentioned above. They also have advantages against space experiments such as low-cost, detailed diagnosis, and feasibility of many trials. Meanwhile, it should be noted that the limitations of theories and space experiments are traded for the resolution limitations of the numerical models.

1.3.2 Classes of Numerical Modeling

There are many different numerical approaches that could be applied to antenna problems in plasmas, each of which has its own advantages and disadvantages. The Method of Moments (MOM) is the most popular method for the antenna analysis in free space [*Harrington*, 1968], which solves integral equations for the conducting antennas combined with Galerkin's method. The method can accurately determine the antenna current distribution, which improves impedance results compared with the aforementioned EMF method.

When applying the method to plasma environments, however, one must use similar approximations to those used in theoretical methods, which makes difficult to significantly improve the results. Moreover, the method is basically the analysis in the frequency domain, and thus is difficult to treat the non-linearity contained in plasma dynamics. Another approach is the Finite Differencing (FD) techniques used to spatially and temporally discretize the antenna/plasma environment according to the differential form of underlying equations. Particularly, the Finite Difference Time Domain (FDTD) method [*Taflove*, 1995] is easier to combine with various numerical plasma models, which have been developed exhaustively in the field of plasma simulations [*Matsumoto and Omura*, 1993]. In the aspect of the antenna analysis, the following approaches can be used in order to incorporate the FDTD method with plasma models, which are listed in the order of ascending rigidness.

Recursive convolution approach

One approach to include plasma effects in the FDTD method is to treat the plasma as a dielectric media. The contribution of plasmas is included by the multiplication of the plasma dielectric function $\epsilon(\omega)$ and the electric field in the frequency domain in Ampères equation. This multiplication, when converted to the time domain, becomes a convolution of the electric field and the time domain representation of the dielectric function. When the function has certain forms such as that for a cold, unmagnetized, collisional plasma, it has been verified that the integration equation of the convolution can be computed recursively, which is more tractable than storing the historical data of the electric field to calculate the convolution [*Luebbers et al.*, 1991; *Cummer*, 1997]. The method is called the Recursive Convolution (RC) scheme.

By using with Maxwell's equations, the RC scheme can perform a full-wave analysis. This also allows the model to yield a self-consistent solution for the current distribution along the antenna. Also, there are a few works that extended the technique to magnetized plasma [e.g., *Hunsberger et al.*, 1992]. However, this technique is basically dependent on the capability to calculate the temporal dependent dielectric representation for the plasma environment. It is generally difficult to expect that the task is easily performed, e.g., for multi-species and warm plasmas. Therefore, the applicability of the scheme is very limited, which is the same disadvantage as was described for the theoretical approaches.

Fluid equation approach

The plasma fluid equations provide a complete description of Maxwellian plasma environments, when combined with Maxwell's equations and closed by additional plasma modeling such as an equation of state. The resulting system can illustrate effects of field energy emanated by antennas on the plasma environments in a self-consistent manner. In

the field of plasma simulations, the single-fluid, Magneto-Hydro-Dynamic (MHD) model has been extensively used for the study of macroscopic physical processes. For the antenna analysis, however, the two-fluid (or multi-fluid) plasma model is generally used to retain an electron inertial effect and a dispersive property of the plasmas [*Ward et al.*, 2005].

Since any kinetic effects are missing, the method cannot be applied to hot and dilute plasma environments typically seen in the outer magnetospheric regions, where plasma waves with wavelengths comparable to the antenna length are susceptible to Landau damping since the Debye length is often larger than the antenna length. Moreover, the effects of an ion sheath and photoelectrons are intractable in the method. The method is rather suitable for relatively colder and denser plasma environments such that the Debye length is sufficiently smaller than the antenna length. Recently, the fluid model is successfully applied to the interpretation of data obtained by the impedance probe in collisional, ionospheric plasmas [*Spencer et al.*, 2008].

Particle-In-Cell approach

The Particle-In-Cell (PIC) is one of the most rigorous approaches to simulate plasma dynamics coupled with associated electromagnetic fields. In the method, we modeled plasmas as a large number of macro-particles generally called "superparticles", each of which represents many real plasma particles contained within a finite volume. The individual particles in the Lagrangian frame are tracked in continuous space, while their moments such as the charge and current densities, and electromagnetic field components defined as Eulerian variables are computed simultaneously on computational mesh points [*Dawson*, 1983; *Birdsall and Langdon*, 1985]. The plasma simulations using the PIC approach is categorized into two groups: a full-particle scheme in which all the species in plasmas are treated as particles, and a hybrid scheme in which electrons and ions are generally treated as fluid and particles, respectively.

Because the equations of motion for individual superparticles are solved, the PIC method enables us to simulate the plasma dynamics including plasma kinetic effects in a self-consistent manner. Also, especially the full-particle scheme is relatively intuitive and straightforward to implement. Thanks to these features, the PIC method has been successfully applied to the analysis of various non-linear processes in collisionless space plasmas such as beam instabilities, shocks, and magnetic reconnection, as well as laser-plasma interactions in laboratory plasmas. On the other hand, it has been recognized that the method is susceptible to non-physical heating, which is caused by much smaller number of superparticles in the Debye sphere than that in real plasmas [*Ueda et al.*, 1994].

The above advantage is important also for the antenna analysis in plasmas, because the kinetics of photoelectrons as well as background plasmas under the influence of charged

antenna and spacecraft bodies is considered as an essential factor for the resulting plasma inhomogeneity. However, the application of the PIC method to the analysis of practical space-based antennas has been highly limited so far, which is primarily due to its too high computational cost. Recently, remarkable progress in supercomputer and high-performance computing gradually makes the computer experiments using the PIC scheme practical in terms of cost and time. In this sense, the establishment of the more complete methodology for the antenna analysis using the PIC scheme is worth the effort.

In the present thesis, based on the PIC technique, we primarily utilize a full-particle treatment for antenna analysis in plasmas including photoelectric effects. Particularly, we have developed a new numerical tool for the antenna analysis based on the three-dimensional Kyoto University Electromagnetic Particle COde (KEMPO). In the new numerical tool, we have adopted numerical treatments for interfaces between a plasma space and conducting bodies of the antenna, which were originally developed for the use in electrostatic particle simulations [*Hockney and Eastwood*, 1981; *Usui*, 1993]. The developed tool is applied to quantitative analysis of the characteristics of practical antennas actually aboard scientific spacecraft, which is the ultimate purpose of the present work.

1.4 Contribution of the Present Work

The present thesis describes the development of the PIC method optimized for the antenna analysis in space plasma environment, and discusses the results of computer experiments on the characteristics of electric antennas onboard scientific spacecraft. We particularly focus on effects of the plasma inhomogeneity due to antenna–plasma and spacecraft–plasma interactions. Figure 1.6 schematically illustrates the contribution of the present work. The upper panel shows the main subject treated in each chapter. The lower panel shows numerical techniques developed or introduced in the present work. It should be noted that the techniques are in part indebted to intellectual knowledge accumulated over the years in the space research group in Research Institute for Sustainable Humanosphere: RISH (former Radio Science Center for Space and Atmosphere: RASC) at Kyoto University.

In Chapter 2, we present detailed descriptions about a new numerical tool named Electromagnetic Spacecraft Environment Simulator (EMSES), which is originally developed for the self-consistent analysis of the spacecraft–plasma interactions on the full electromagnetic (EM) basis. For the analysis of electric antenna characteristics in space plasma, we must introduce a numerical model of conducting surfaces of antenna bodies. Further, the inclusion of EM effects is mandatory to treat space-based electric antennas which radiate or receive EM waves. In EMSES, we carefully coded boundary treatments for both longitudinal and transverse electric fields on perfect conducting surfaces. The im-

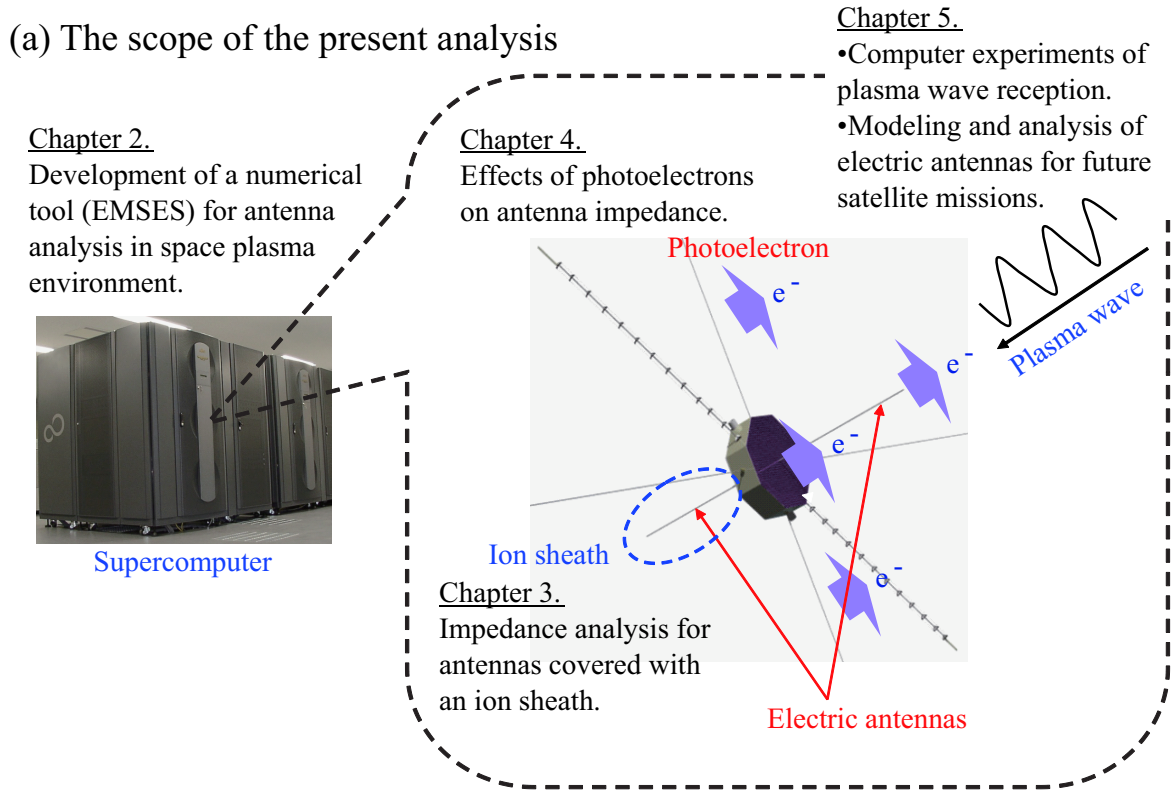

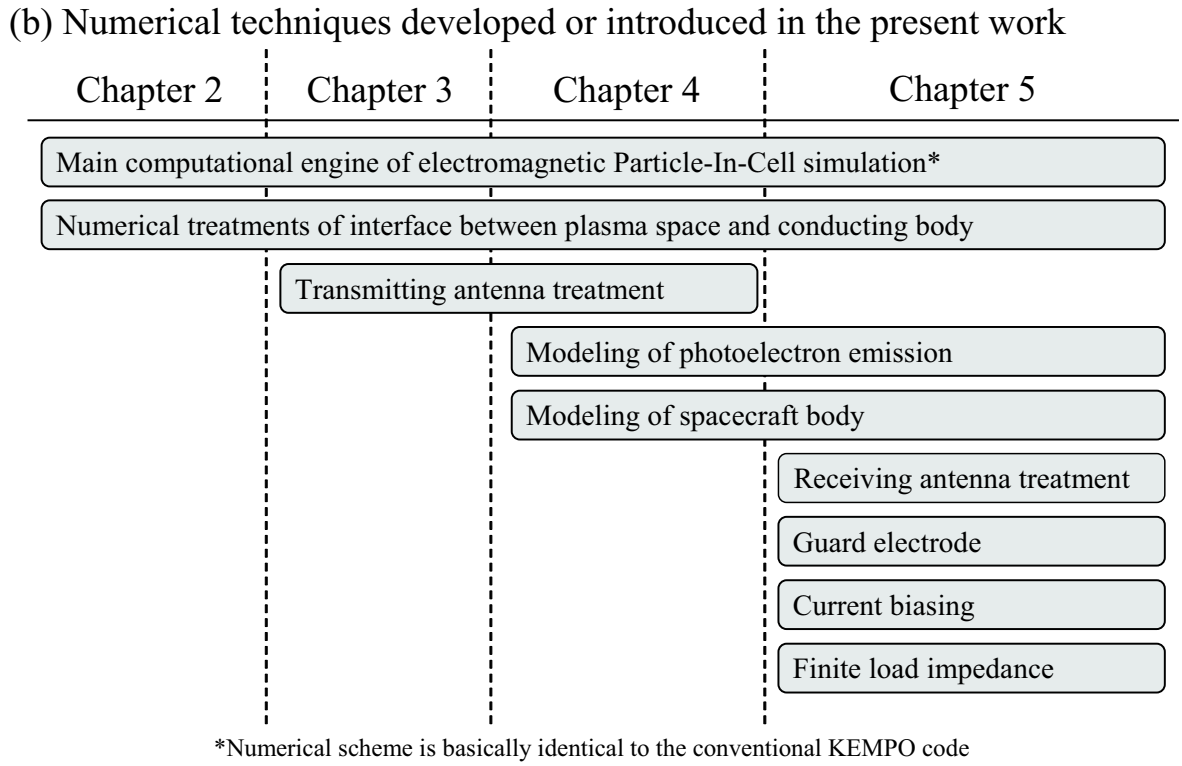

Figure 1.6: Contribution of the present work. (a) The analysis object examined in each chapter. (b) Numerical techniques developed or introduced in the present work.

portant point to notice is that the longitudinal electric field component should always satisfy Gauss's law with the charge distribution in that moment. This is not necessarily obvious in the EM-PIC simulation, because Gauss's law is not explicitly solved. This requires some additional boundary treatments also for the charge and current densities in the vicinity of the conducting bodies. The details are described in this chapter. We also validate EMSES, in which we perform test simulations for the spacecraft charging and the properties of peculiar EM wave modes in a plasma sheath.

Chapter 3 describes results obtained by computer experiments for the impedance of an electrically short dipole antenna covered with an electron-sparse region. Its major motivation is to demonstrate the application of EMSES to the antenna analysis. We particularly simulate the behavior of a transmitting antenna with low power. The obtained impedance is fundamental and useful for the validation of the present method. For the validation, we consider a very fundamental situation in which a set of dipole antenna is immersed in a Maxwellian, unmagnetized, and collisionless plasma. The plasma is so dense and low-temperature that the Debye length becomes smaller than the antenna length, which is expected to yield an impedance resonance at the electron plasma frequency. First, we validate the antenna modeling used in EMSES by examining the impedance excluding any effects of an ion sheath and comparing obtained results to the conventional kinetic theories. After that, we analyze the impedance characteristics of antennas covered with an ion sheath, which is created under the condition that an antenna has a negative floating potential. One of focal points is the structure of the sheath, which is created as a result of self-consistent computation of the antenna-plasma interactions. We also discuss the dependence of the antenna impedance on the sheath thickness.

Chapter 4 is devoted to the discussion of photoelectron effects on the impedance of electric antennas. In the outer magnetosphere of the Earth, the Debye length is often comparable to or larger than the antenna length. In this environment, photoelectrons predominantly have high density compared to the background plasma electrons and are expected to influence the antenna impedance. We first survey a plasma environment created around the spacecraft as a result of the photoelectron emission obtained by computer experiments. We then examine photoelectron effects on the antenna impedance. The numerical result shows that the dense photoelectrons influence the antenna impedance over a wide-frequency range below a certain frequency. For interpretation of the photoelectron effect, we introduce an equivalent electric circuit model for the photoelectron effect and derive an analytical estimation for the impedance modification due to the photoelectron emission. Finally, we briefly discuss the contribution of the present results to the interpretation of in-flight impedance measurement data obtained by the GEOTAIL spacecraft.

In Chapter 5, we introduce a new technique for the antenna analysis, which directly

simulates the plasma-wave reception by the antenna. In Chapters 3 and 4, we investigate antenna characteristics by simulating transmitting behavior of the antenna. In the presence of the reciprocity relation between transmitting and receiving antennas, the obtained results can be directly applied also to the receiving antennas. However, in plasma environment, the reciprocity has been strictly proved only in limited simple situations in previous works [*Ishizone et al.*, 1976]. In order to extend the analysis to receiving antennas in environment of unknown reciprocity, we have developed a plug-in routine, with which we set up wave fields propagating in the simulation region and directly simulate the process of receiving the wave fields by the antenna. We also develop a numerical model for a modern electric field instrument designed based on a "hockey puck" principle. The notable feature of the instrument is the equipment of the guard electrode that can minimize photoelectron effects which are formidable particularly for measurements of DC electric field. We need to investigate whether or not the new equipment optimized for DC measurements is suitable also for wave measurements. We first describe the plasma environment in the vicinity of the instrument as a steady-state and effects of the guard electrode and the current biasing on the environment. Next, Section 5.4.3 describes results for the effective length and the impedance of the instrument in receiving external plasma waves.

In Chapter 6, we will summarize the present study and give conclusions obtained in the present computer experiments. We also present suggestions for future works.

Chapter 2

Numerical Techniques for Antenna Analysis in Space Plasmas

2.1 Electromagnetic Spacecraft Environment Simulator: EMSES

In this chapter, we describe numerical techniques for computer experiments of electric antennas in space plasma environment. Because the code can be applied not only to the antenna analysis but also to more general problems regarding spacecraft–plasma interactions, we begin this chapter with reviewing previous numerical studies of spacecraft–plasma interactions.

Spacecraft–plasma interactions have become an issue of great importance with the rapid increase of human activities in space [*Hastings and Garrett*, 1996; *Martin* 1994] and the modeling and examination of spacecraft–plasma interactions have progressed significantly in recent years. To date, most concerns have focused on the quasi-electrostatic phenomena. For example, spacecraft charging is recognized as a significant problem, influencing the performance of spacecraft systems and the accuracy of plasma wave and particle sensors [*Garrett*, 1981; *Garrett and Whittlesey*, 2000; *Whipple*, 1981]. For the spacecraft charging problem, the National Aeronautics and Space Administration (NASA), the European Space Agency, and the Japan Aerospace Exploration Agency developed the NASA Charging Analyzer Program (NASCAP) [*Mandell*, 2006], the Spacecraft Plasma Interaction System (SPIS) [*Roussel et al.*, 2008], and the Multi-Utility Spacecraft Charging Analysis Tool (MUSCAT) [*Muranaka et al.*, 2008], respectively. Although the latest versions of the above tools partly utilize the PIC technique [*Birdsall and Langdon*, 1985], they have so far been mainly used to obtain the steady-state solution of the spacecraft charging problem. There have been exhaustive studies of the PIC technique for analyzing spacecraft–plasma interactions, but most use the ES-PIC basis [*Roussel et al.*, 2008; *Forest et al.*, 2006; *Kafafy and Wang*, 2006].

When analyzing the properties of transmitting antennas in space, we need to examine

the transient process of the interactions between the emitted RF power and surrounding plasmas even at the scale of electron dynamics. To examine such transient processes, we require a full EM-PIC simulation which can include solid spacecraft surfaces [*Usui et al.*, 2006]. In the full EM model, however, the numerical treatments of superparticles and electric fields at inner boundaries corresponding to spacecraft surfaces should be modified and new treatments should be added. Presently, there exists little literature that explicitly describes full EM treatments for the inclusion of solid bodies of spacecraft in PIC simulations.

In consideration of the above demands, we have developed a new simulation code, the Electromagnetic Spacecraft Environment Simulator (EMSES), for the self-consistent analysis of spacecraft–plasma interactions using the full EM-PIC basis [*Miyake and Usui*, 2008d]. In EMSES, spacecraft surfaces are represented by inner boundaries constructed of perfect conductors. Both EM and ES fields satisfy the appropriate conditions for perfect conducting surfaces. We also implement interface treatments for the current density induced by plasma particles impinging on or emitted from the spacecraft surfaces. Although some of the methods in the approach have been used individually in conventional simulations, the combination and the implementation of the methods to EM-PIC simulation for spacecraft environment analysis are new concepts and described for the first time in the present paper.

We describe details of EMSES in Sections 2.2 and 2.3. Then, we present test simulations for the validation of EMSES in Section 2.4. We particularly focus on two basic problems, the spacecraft charging problem and the properties of EM wave modes which propagate along spacecraft conducting surfaces.

2.2 Overview of EMSES

The plasma description used in EMSES is based on an existing EM particle code called KEMPO (see *Matsumoto and Omura* [1993] for details). In the code, the equations of motion for charged "superparticles" (introduced in Section 1.3.2) and Maxwell's equations for the EM fields are simultaneously solved in a self-consistent manner. Considering no relativistic effect, the equations of motion for each particle are given by

$$\frac{d\boldsymbol{r}}{dt} = \boldsymbol{v}, \tag{2.1}$$

$$\frac{d\boldsymbol{v}}{dt} = \frac{q}{m}(\boldsymbol{E} + \boldsymbol{v} \times \boldsymbol{B}), \tag{2.2}$$

where $\boldsymbol{r}$, $\boldsymbol{v}$, q, m, $\boldsymbol{E}$, and $\boldsymbol{B}$ represent the particle position, velocity, charge, mass, and the electric and magnetic fields, respectively. Then, the following sets of Maxwell's equations

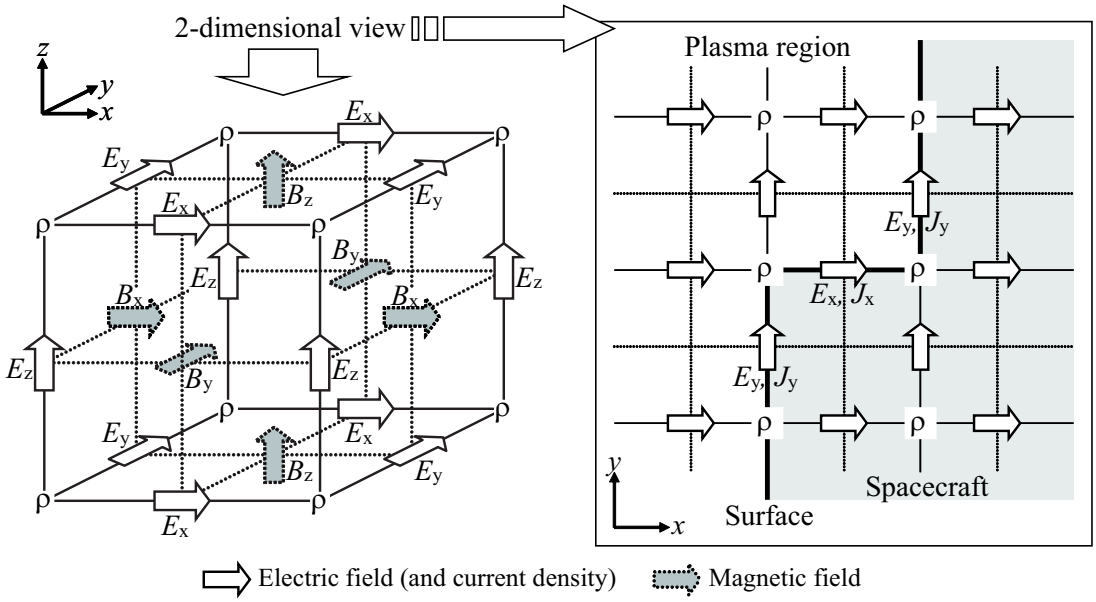

Figure 2.1: (Left panel) Assignment of field vector components and charge density about a cubic unit cell based on the Yee algorithm. The vector components of the current density are assigned at the same positions as the electric field. (Right panel) Two-dimensional view of the mesh and an example of the assignment of a spacecraft surface. The surface should be assigned such that the tangential components of the electric field are located on the surface. In both panels, solid and dashed lines represent full-integer and half-integer grid lines, respectively.

are solved as basic equations:

$$\nabla \times \boldsymbol{B} = \mu_0 \boldsymbol{J} + \frac{1}{c^2}\frac{\partial \boldsymbol{E}}{\partial t}, \tag{2.3}$$

$$\nabla \times \boldsymbol{E} = -\frac{\partial \boldsymbol{B}}{\partial t}, \tag{2.4}$$

where $\boldsymbol{J}$, ρ, μ_0, and c represent the current and charge densities, the magnetic permeability, and the speed of light, respectively.

For updating of the particle velocities, we use the Buneman–Boris scheme, which conserves the kinetic energy in the calculation of cyclotron motion [*Birdsall and Langdon*, 1985]. In the three-dimensional system, the values of the EM field components are defined at grid points, which are assigned based on the Yee algorithm [*Yee*, 1966]. The left panel of Figure 2.1 shows the field assignment. The EM fields are advanced by using the standard Finite-Difference Time-Domain (FDTD) method [*Taflove*, 1995].

Superparticles move continuously in the computational space, while the field components are defined only at grid points. Thus, in order to obtain the field terms in Eq. (2.2) for each particle, we linearly interpolate the field components defined at the adjacent eight grid points around the particle. Similarly, to obtain the source term, i.e., the current density $\boldsymbol{J}$, in Eq. (2.3), we distribute the charge flux $\rho\boldsymbol{v}$ calculated at the particle positions

to adjacent grid points, where ρ represents the charge density. For the calculation of $\boldsymbol{J}$, we employ a Charge Conservation (CC) method developed by *Umeda et al.* [2003], which assures the continuity equation for charge. By using the above schemes, the variation of the EM field values and the dynamics of superparticles are updated self-consistently.

Solid spacecraft bodies, represented as inner boundaries of conducting surfaces, are immersed in a three-dimensional simulation space. In EMSES, the geometry of the spacecraft is described by a Cartesian coordinate grid. In the right panel of Figure 2.1, we show a two-dimensional view of the grid and an example of the assignment of a spacecraft surface. Since the Yee grid has a staggered arrangement of field components, the spacecraft surfaces must be carefully assigned on the grid. When treating a perfect electric conductor, conductor surface treatments are required for the tangential components of the electric field and the charge density. Therefore, the conductor surface should be set along a grid line on which electric field components are defined, as shown in the right panel of Figure 2.1. We can see that the charge density values are also located on the spacecraft surface, which is convenient for evaluating the amount of surface charge on the spacecraft, as will be described in Section 2.3.

The impingement of plasma particles on spacecraft bodies and the emission of photoelectrons from spacecraft surfaces are primary factors in spacecraft charging. In EMSES, we consider particle impingement to occur when particles move inside the spacecraft-body region during Δt, where Δt represents the time step width. After that time, we regard them as being absorbed in the body. At this stage, we no longer solve the equations of motion for the absorbed particles. Instead the charge of the absorbed particles is accumulated on the spacecraft surface and contributes to the longitudinal component of the electric field.

For particle emission from the surface, we use the conventional particle-loading scheme [*Birdsall and Langdon*, 1985; *Cartwright et al.*, 2000]. We first determine the initial positions and velocities of emitted particles. We then start to solve their motion. In this situation, charges of the same quantity and opposite sign of the emitted particles remain at the spacecraft surfaces and contribute to the spacecraft charging. The detailed treatments for the charge accumulation are presented in the next section. At present, we simply determine the number of emitted particles per Δt as an input parameter and assume the Maxwellian for the velocity distribution. However, depending on what kinds of particles (e.g., photo- and secondary electrons) we want to model, we require more realistic modeling for the flux and the velocity distribution of the emitted particles, which is left as future work and not discussed in the present thesis.

We incorporated the aforementioned main functions in the simulation code. Figure 2.2 shows a diagram of the procedures in one computational cycle. Processes (procs.) 1, 3, 6, and 10, shown by white boxes in Figure 2.2, are conventional and are also included

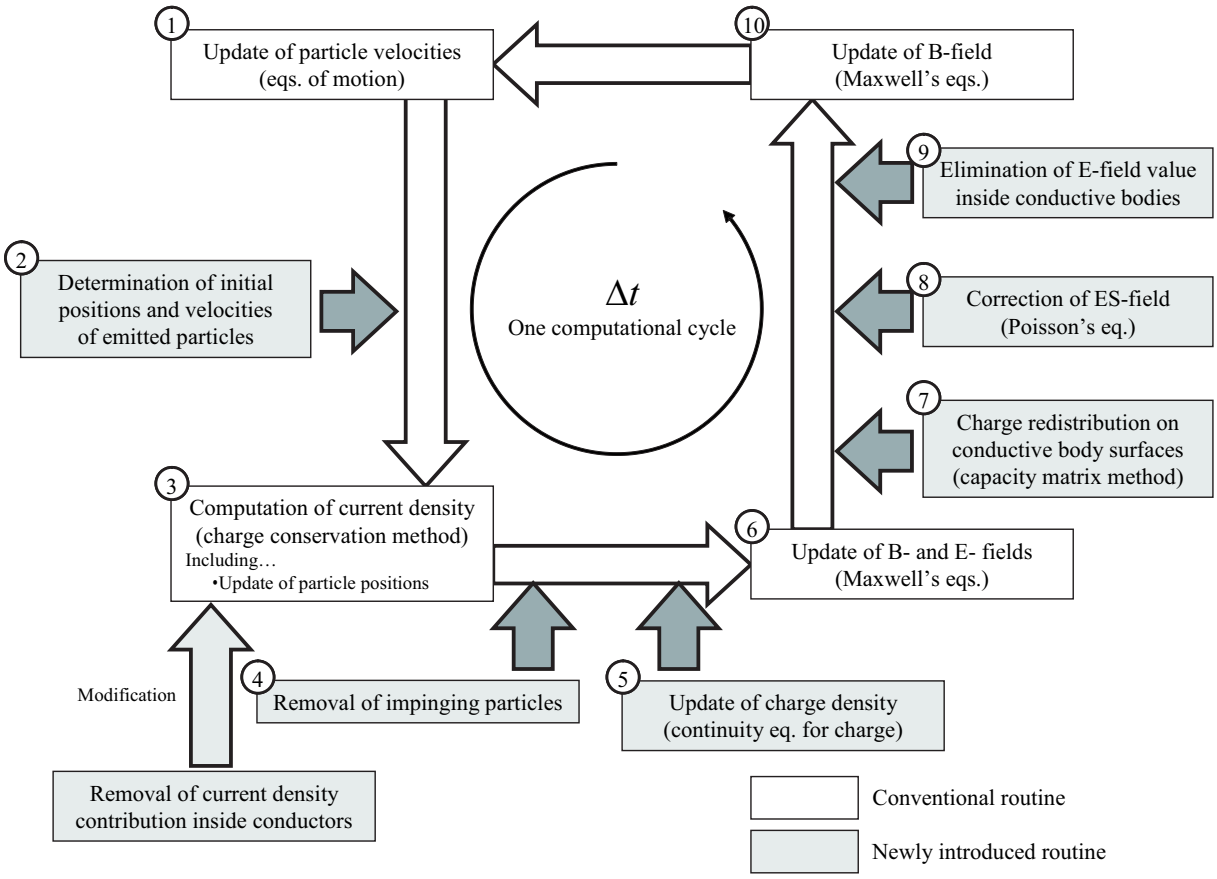

Figure 2.2: Block diagram of main routines included in one computational cycle.

in the KEMPO code; the methods of their computations are detailed in the literature [*Matsumoto and Omura*, 1993; *Umeda et al.*, 2003]. The procedures shown by shaded boxes are newly introduced in EMSES to treat conducting solid-body regions immersed in plasma. We can categorize the procedures into treatments of superparticles (procs. 2 and 4) and those for field components (procs. 7, 8, and 9). In addition, proc. 5 is necessary because charge density data are used in proc. 7. We also introduce a modification to the CC scheme (proc. 3) in calculating the current density contributed by particles impinging on or emitted from the spacecraft body.

In the next section, we present the details of the treatments for the EM field and charge density at a conducting spacecraft surface. The corresponding procedures in Figure 2.2 are procs. 3, 5, 7, 8, and 9.

2.3 Numerical Treatment of Conducting Spacecraft Surface

2.3.1 Longitudinal Electric Field Associated with Surface Charge Distribution

This section considers the electric field at the conducting surfaces of a spacecraft. Generally, electric fields obtained by Maxwell's equations include ES as well as EM components. For a uniform plasma, it has been theoretically confirmed that the electric fields can be correctly updated if the current density at each grid point in the simulation model satisfies the charge continuity equation. However, once conducting surfaces are introduced as inner boundaries in the simulation system, electric fields, particularly the longitudinal (ES) component, at the surfaces must be carefully solved in consideration of the interface between the plasma and a conducting body. Since the ES component must satisfy Gauss's law in which the charge density is a variable, we must treat the charge distribution on the surface such that the characteristics of the conducting materials are maintained at the interface.

In Figure 2.3, we summarize the procedures which, directly or indirectly, modify the surface charge and the ES field component associated with the charge. For discussions hereafter, we define the following symbols for the electric field and charge density. The total electric field $\boldsymbol{E}$ includes the transverse component $\boldsymbol{E}_{\mathrm{T}}$ and the longitudinal component $\boldsymbol{E}_{\mathrm{L}}$. The longitudinal component $\boldsymbol{E}_{\mathrm{L}}$ is composed of two components $\boldsymbol{E}_{\mathrm{Lp}}$ and $\boldsymbol{E}_{\mathrm{Ls}}$, which are related respectively to the charge densities ρ_{p} produced by plasma particles and ρ_{s} produced by surface charge on the spacecraft.

As shown in Figure 2.3, there are two mechanisms by which ρ_{s} and $\boldsymbol{E}_{\mathrm{Ls}}$ are modified. First, ρ_{s} and $\boldsymbol{E}_{\mathrm{Ls}}$ vary due to particles impinging on or emitted from spacecraft surfaces, which occurs during Δt. We define the variation of ρ_{s} and $\boldsymbol{E}_{\mathrm{Ls}}$ by this mechanism as $\Delta\rho_{\mathrm{s}}$ and $\Delta\boldsymbol{E}_{\mathrm{Ls}}$. In EMSES, $\Delta\rho_{\mathrm{s}}$ and $\Delta\boldsymbol{E}_{\mathrm{Ls}}$ are taken into account by using the current density $\boldsymbol{J}$ induced by the particle impingement and emission. In the following section, we present the necessary treatments for $\boldsymbol{J}$ around a spacecraft surface to reproduce the accumulation of ρ_{s} on each grid point of the surface correctly. Then, we describe in Section 2.3.3 how $\Delta\rho_{\mathrm{s}}$ and $\Delta\boldsymbol{E}_{\mathrm{Ls}}$ are computed in procs. 5 and 6.

Next, ρ_{s} and $\boldsymbol{E}_{\mathrm{Ls}}$ should be modified again to realize an equipotential on the conducting spacecraft surface. This variation is represented as $\delta\rho_{\mathrm{s}}$ and $\delta\boldsymbol{E}_{\mathrm{Ls}}$ in the figure. In the code, the charge redistribution is explicitly reproduced in procs. 7 and 8. We present a detailed description for the modification in Section 2.3.4.

	Numerical treatments actually conducted in the routines	Effects on ρ_s and $\boldsymbol{E}_{Ls}$	Description
3. Computation of current density	• Charge Conservation method • Body surface treatments of $\boldsymbol{J}$		2.3.2
5. Update of charge density	$\rho^{n+1} = \rho^n - \Delta t(\nabla \cdot \boldsymbol{J}^{n+1/2})$	$\rho_s \leftarrow \rho_s + \Delta\rho_s$	2.3.3
6. Update of E-field	$\boldsymbol{E}^{n+1} = \boldsymbol{E}^n + \Delta t\left\{c^2\nabla \times \boldsymbol{B}^{n+1/2} - \frac{1}{\epsilon_0}\boldsymbol{J}^{n+1/2}\right\}$	$\boldsymbol{E}_{Ls} \leftarrow \boldsymbol{E}_{Ls} + \Delta\boldsymbol{E}_{Ls}$	
7. Surface Charge redistribution	• Capacity Matrix method • $\rho \leftarrow \rho + \delta\rho_s$	$\rho_s \leftarrow \rho_s + \delta\rho_s$	2.3.4
8. Correction of ES-field	• $\nabla \cdot (\delta\boldsymbol{E}_{Ls}) = (\delta\rho_s)/\epsilon_0$ • $\boldsymbol{E} \leftarrow \boldsymbol{E} + \delta\boldsymbol{E}_{Ls}$	$\boldsymbol{E}_{Ls} \leftarrow \boldsymbol{E}_{Ls} + \delta\boldsymbol{E}_{Ls}$	

Figure 2.3: List of routines which treat the charge distribution ρ_s on a conducting spacecraft surface and the electric field $\boldsymbol{E}_{Ls}$ associated with the charge.

2.3.2 Current Density Treatment on Spacecraft Surface

Since $\boldsymbol{J}$ is responsible for $\Delta\rho_s$ and $\Delta\boldsymbol{E}_{Ls}$, as described in the previous section, we should pay careful attention to a boundary treatment when computing $\boldsymbol{J}$ in the vicinity of the conducting surface. As mentioned in Section 2.2, we adopt the CC method for the computation of $\boldsymbol{J}$ at each grid point. The basic concept of the CC method is that the charge flux $\rho\boldsymbol{v}$ of each particle is computed from the start and end points of the particle movement during Δt.

A spacecraft surface is defined along a grid line, and hence we consider the two cases of a particle crossing a grid line and crossing the spacecraft surface. Figure 2.4(a) shows a diagram of the CC method when calculating $\boldsymbol{J}$ for a particle trajectory crossing a grid line. In this case, we compute the charge flux separately for each of the two trajectory segments, i.e., fluxes 1 and 2, which correspond to before and after crossing the grid line, respectively. Then, as shown in the figure, the contribution of the particle motion is distributed to the current density components: J_{x1}, J_{x3}, J_{y1}, J_{y2} for charge flux 1 and J_{x2}, J_{x4}, J_{y2}, J_{y3} for charge flux 2.

On the other hand, when the grid line corresponds to a spacecraft surface, J_{x2}, J_{x4},

and J_{y3} must be zero. If J_{x2}, J_{x4}, and J_{y3} have non-zero values, the values of ρ_1 and ρ_2, which are defined inside the conducting body as shown in Figure 2.4(b), can change. This means that the charge accumulates inside the body rather than on its surface, which is unphysical in the present case of a body made of a perfect electric conductor. To prevent this undesirable effect we employ a treatment that does not distribute the contribution of charge flux 2 to adjacent grid points. Namely, we select only the contribution of the trajectory before crossing the solid body surface and discard that after the crossing. Coding of this treatment is straightforward because the trajectory has already been decomposed in the CC method at the grid line corresponding to the conducting surface.

The boundary treatments proposed above can also be applied to particle emission from a spacecraft surface. In proc. 2, we set a temporary position of an emitted particle inside the solid body region, i.e., at a depth of $R_{\mathrm{u}}|v_{\mathrm{n}}|\Delta t$, where v_{n} and R_{u} represent the normal velocity component of the particle and a uniform random number varying from 0 to 1, respectively. Note that the placed particle inevitably leaves the body region during Δt in proc. 3. Although the charge flux computed by the particle motion has a trajectory even inside the spacecraft body, we select only the contribution of the trajectory outside the body in the same manner as for the particle impingement case.

The above treatment for emitted particles reproduces the fact that emission occurs exactly on the spacecraft surface. Furthermore, by setting an initial depth as $R_{\mathrm{u}}|v_{\mathrm{n}}|\Delta t$, we can simulate that particle emission occurs at a time $t = t_0 + R_{\mathrm{u}}\Delta t$, where t_0 represents the physical time at the beginning of the computational cycle. The use of the random number R_{u}, which varies for each emitted particle, produces a temporally smooth emission.

2.3.3 Charge Accumulation on Spacecraft Surface

In proc. 5, we update a profile of the total charge density $\rho = \rho_{\mathrm{p}} + \rho_{\mathrm{s}}$ by explicitly solving the continuity equation for charge, the time-difference form of which is given as follows:

$$\rho^{n+1} = \rho^n - \Delta t(\nabla \cdot \boldsymbol{J}^{n+1/2}), \tag{2.5}$$

where the superscripts denote the time step level.

Although the impinging particles are regarded as being absorbed in proc. 4 and no longer exist as superparticles in the simulation system, we compute $\boldsymbol{J}^{n+1/2}$ in consideration of the motion of the impinging particles in proc. 3. Of course, $\boldsymbol{J}^{n+1/2}$ induced by particles emitted from a spacecraft surface is also considered. Therefore, the charge accumulation on the spacecraft surface, i.e., $\Delta\rho_{\mathrm{s}}$ is automatically taken into consideration.

In proc. 6, the electric field is computed by solving the time difference form of Ampère's law, which is given as

$$\boldsymbol{E}^{n+1} = \boldsymbol{E}^n + \Delta t \left\{ c^2 \nabla \times \boldsymbol{B}^{n+1/2} - \frac{1}{\epsilon_0} \boldsymbol{J}^{n+1/2} \right\}, \tag{2.6}$$

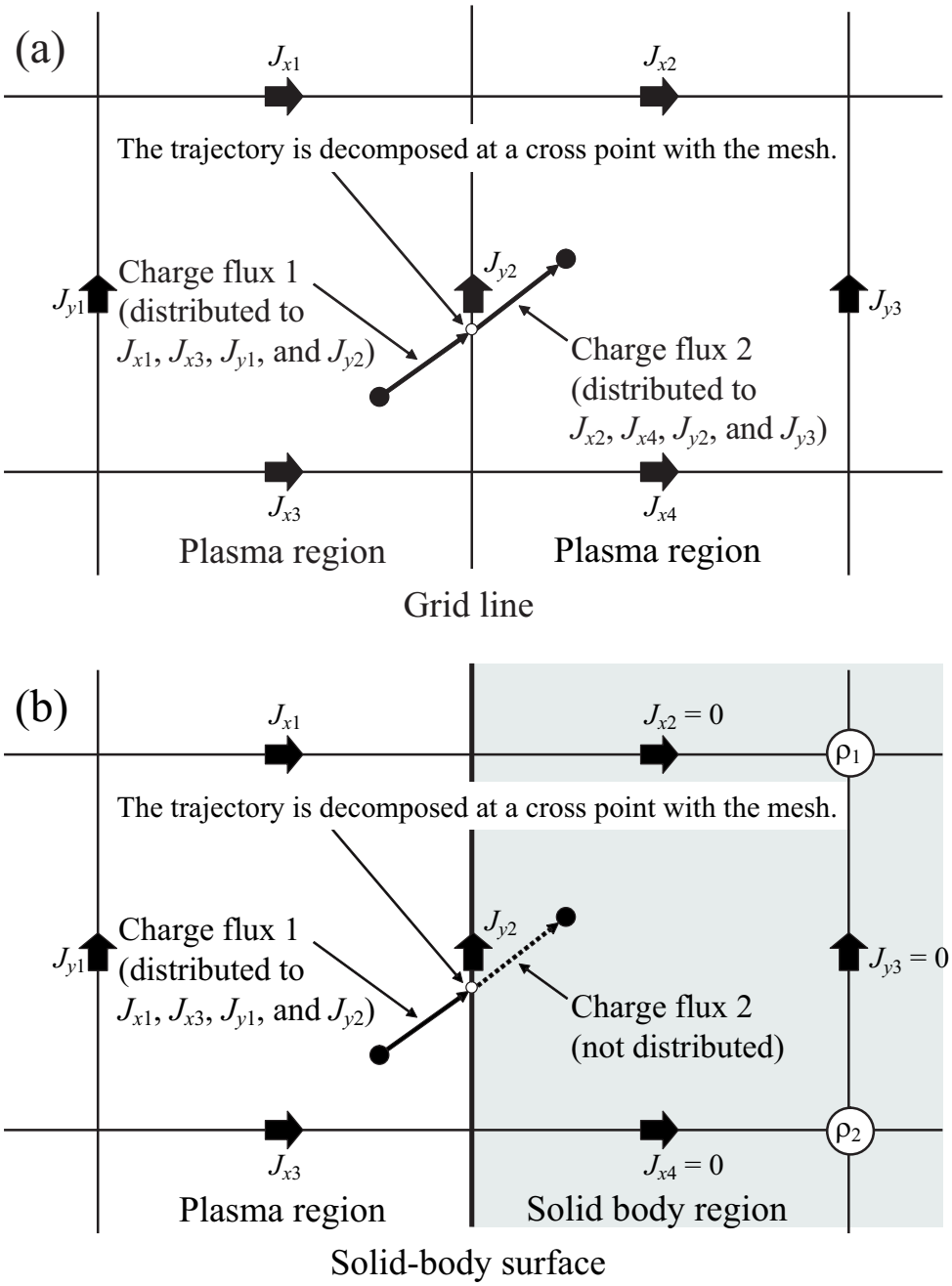

Figure 2.4: Two-dimensional diagrams of example trajectory decompositions crossing (a) a grid line and (b) a solid-body surface during Δt. When the particle crosses the solid-body surface, the charge flux located inside the body is discarded and does not contribute to current density computation.

where ϵ_0 represents the permittivity in vacuum. Equation (2.6) clearly has an "update form" for $\boldsymbol{E}$.

In order to show the automatic inclusion of $\Delta\boldsymbol{E}_{\rm Ls}$ by Eq. (2.6) in proc. 6, we consider $\Delta\rho_{\rm s}$ due to $\boldsymbol{J}^{n+1/2}$ induced by the particle impingement. From Eq. (2.5), $\Delta\rho_{\rm s}$ and $\boldsymbol{J}^{n+1/2}$ are related as $\Delta\rho_{\rm s} = -\Delta t(\nabla\cdot\boldsymbol{J}^{n+1/2})$. By taking the divergence of Eq. (2.6) and substituting the above equation, we obtain

$$\nabla\cdot\boldsymbol{E}^{n+1} = \nabla\cdot\boldsymbol{E}^{n} + \frac{\Delta\rho_{\rm s}}{\epsilon_0} \tag{2.7}$$

$$= \nabla\cdot(\boldsymbol{E}^{n} + \Delta\boldsymbol{E}_{\rm Ls}), \tag{2.8}$$

where we use Gauss's law $\nabla\cdot\Delta\boldsymbol{E}_{\rm Ls} = (\Delta\rho_{\rm s})/\epsilon_0$. The resulting equation clearly indicates that proc. 6 can automatically include the contribution of $\Delta\boldsymbol{E}_{\rm Ls}$ in the computation of Eq. (2.6). It should be noted that the actually solved equation in EMSES is not Eq. (2.8) but Eq. (2.6).

2.3.4 Charge Redistribution on a Conducting Surface

After obtaining $\rho_{\rm s}$ and $\boldsymbol{E}_{\rm Ls}$ immediately after the particle impingement and emission, we next redistribute the charge on the conducting surface in proc. 7. To obtain a new surface charge distribution that realizes an equipotential solution, we used the Capacity Matrix method [*Hockney and Eastwood*, 1981], the basic concept of which is given in the Appendix A. Here we briefly present the procedures conducted in EMSES for a case of one conducting body immersed in a plasma with a certain floating potential.

As described in Appendix , the correction of the electrical potential $\delta\phi_{\rm s}$ on a conducting surface is related to the surface charge density $\delta\rho_{\rm s}$ by a capacity matrix C as follows:

$$\delta\rho_{{\rm s},i} = \sum_{j=1}^{N_{\rm B}} C_{ij}\delta\phi_{{\rm s},j}, \quad (i = 1,\ldots,N_{\rm B}), \tag{2.9}$$

where i and j are indices of grid points on the conducting surface, and $N_{\rm B}$ represents their total number.

After proc. 6, the surface potential $\phi_{{\rm s},j}$ has not yet taken the same value for all j, and hence the surface does not have an equipotential. When an equipotential value $\phi_{\rm c}$ should be formed, Eq. (2.9) can be rewritten as

$$\delta\rho_{{\rm s},i} = \sum_{j=1}^{N_{\rm B}} C_{ij}(\phi_{\rm c} - \phi_{{\rm s},j}), \quad (i = 1,\ldots,N_{\rm B}). \tag{2.10}$$

However, $\phi_{\rm c}$ is unknown at this stage. To obtain $\phi_{\rm c}$, we use the condition that the total charge accumulated on the body surface is conserved throughout the redistribution of the surface charge, which is represented as

$$\sum_{i=1}^{N_{\rm B}} \delta\rho_{{\rm s},i} = 0. \tag{2.11}$$

This gives ϕ_c as

$$\phi_c = \frac{\sum_i \sum_j C_{ij}\phi_{s,j}}{\sum_i \sum_j C_{ij}}. \tag{2.12}$$

We then calculate a profile of $\delta\rho_{s,i}$ by solving Eq. (2.10) for all i with the obtained ϕ_c, which produces the complete set of the surface charge correction $\delta\rho_s$.

Finally, in proc. 8, we correct the profile of $\boldsymbol{E}_{Ls}$ using the obtained $\delta\rho_s$. We first obtain the correction of the longitudinal electric field $\delta\boldsymbol{E}_{Ls}$ by solving Poisson's equation. Then, a modified profile $\boldsymbol{E}'_{Ls}$ is computed as $\boldsymbol{E}'_{Ls} = \boldsymbol{E}_{Ls} + \delta\boldsymbol{E}_{Ls}$.

2.3.5 Transverse Electric Field Component

We also require a conducting surface treatment for the transverse component $\boldsymbol{E}_T$. $\boldsymbol{E}_T$ defined inside the conducting body region is set to zero. As for a conducting body surface, only the tangential component of the $\boldsymbol{E}_T$ values should be eliminated. These treatments are provided in proc. 9 after the treatments of the longitudinal electric field and the surface charge.

The above treatments were originally developed for charge-free computations such as FDTD simulations in free space, i.e., for situations where a divergence-free condition is always assured with respect to an electric field component [*Taflove*, 1995]. However, we can apply the treatments to the present non-charge-free simulation. By proc 9, the tangential component of $\boldsymbol{E}_L$ has become zero at the conducting surface, and the non-zero electric field should consist of only $\boldsymbol{E}_T$. Therefore, we can eliminate the electric field value without any influence on $\boldsymbol{E}_L$.

2.4 Test Simulations

2.4.1 Conducting Body Charging in a Maxwellian Plasma

In this section, we present a test simulation of the charging process of a conducting body immersed in a Maxwellian plasma using EMSES. As described in the previous section, EMSES can handle ES as well as EM phenomena. Therefore we here choose a simple case of spacecraft charging governed by the ES field, to validate EMSES by comparing the result with that obtained by previous theoretical studies [*Mott-Smith and Langmuir*, 1926; *Laframboise*, 1966]. A validation for EM phenomena will be presented in Section 2.4.2.

Figure 2.5 shows the three-dimensional simulation model for the current test. A conducting sphere is immersed in a Maxwellian plasma consisting of mobile electrons and ions. Since EMSES only supports a Cartesian coordinate grid, the actual conductor configuration is a roughly approximated sphere. In the current test, the radius a of the approximated sphere is about $0.25\lambda_D$, where λ_D represents the Debye length for the surrounding plasma. In the condition, the sheath size, which is a few Debye lengths, is

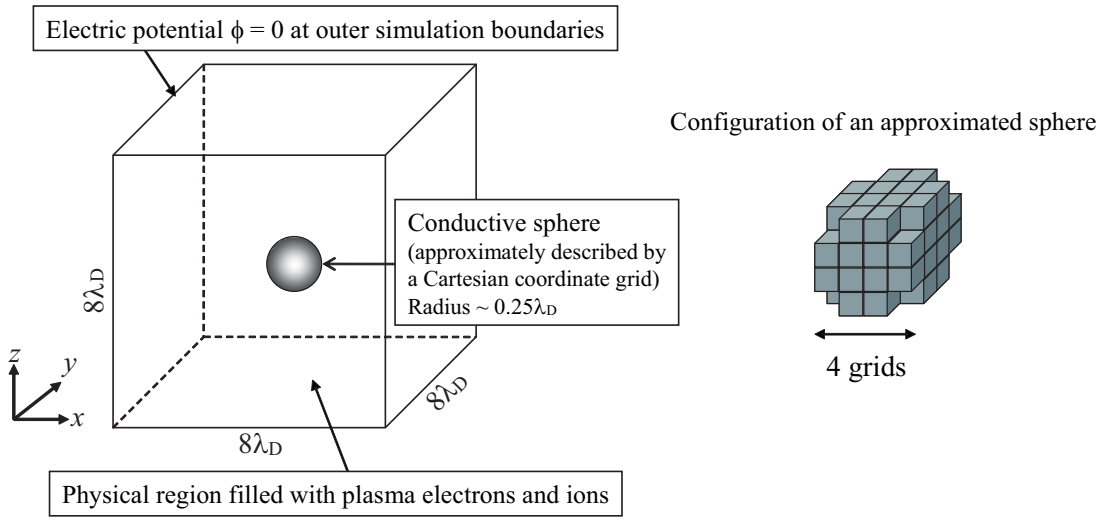

Figure 2.5: Three-dimensional simulation model for testing the charging of a spherical conducting body.

supposed to become sufficiently greater than a, and thus we can use the Orbital-Motion-Limited (OML) theory, which is the thick-sheath theory developed by *Mott-Smith and Langmuir* [1926] as a counterpart of the comparison.

The number of superparticles is set at 64/cell for each of electrons and ions. We assume the mass ratio $m_\mathrm{i}/m_\mathrm{e} = 100$ for the electron mass m_e and the ion mass m_i. Although the ratio is smaller than the real electron–proton mass ratio and has an impact on a resulting floating potential, we can test the basic behavior of the code in the comparison with the theoretical result obtained using the same parameter. We also assume $T_\mathrm{e}/T_\mathrm{i} = 1$, where T_e and T_i represent the electron and ion temperatures, respectively.

Using the model given above, we run a simulation with EMSES to obtain equilibrium solutions of the floating potential and the sheath environment. The electric potential profile at the steady state is displayed in Figure 2.6. We plot a potential curve along an axis that penetrates the center of the conductor. From the potential curve, the equilibrium floating potential of the conductor is found to be $\phi_\mathrm{f} = -1.50 k_\mathrm{B} T_\mathrm{e}/e$ assuming a reference potential as an averaged potential in the background plasma region. Here, k_B and e are Boltzmann's constant and the electric unit charge, respectively.

Theoretically, the equilibrium floating potential is obtained from the balance between the electron current I_e and the ion current I_i flowing into the conductor. In the OML theory, these currents are expressed as functions of the conductor potential ϕ. For the small spherical conductor, the currents are given as

$$I_\mathrm{e}(\phi) \quad = \quad S n_0 e \sqrt{\frac{k_\mathrm{B} T_\mathrm{e}}{2\pi m_\mathrm{e}}} \exp\left(\frac{e\phi}{k_\mathrm{B} T_\mathrm{e}}\right) \tag{2.13}$$

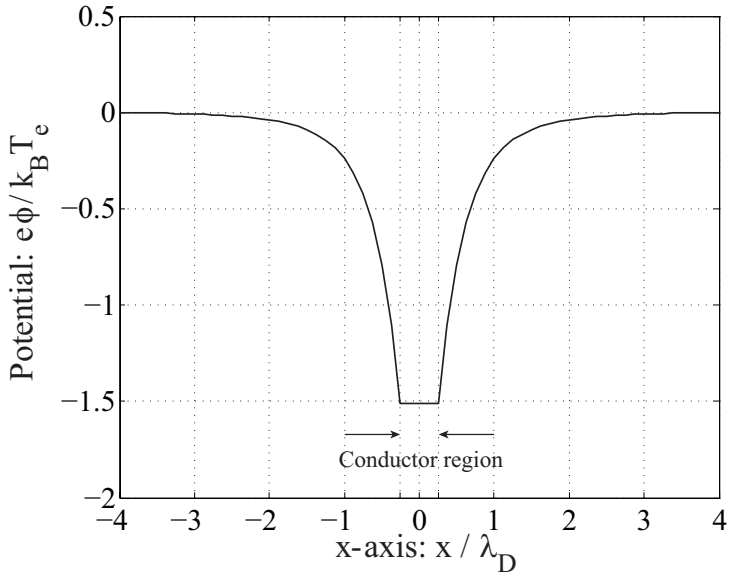

Figure 2.6: One-dimensional profile of the time-averaged electric potential along an axis penetrating the center of a spherical conducting body.

$$I_{\rm i}(\phi) \;=\; Sn_0 e\sqrt{\frac{k_{\rm B}T_{\rm i}}{2\pi m_{\rm i}}}\left(1-\frac{e\phi}{k_{\rm B}T_{\rm i}}\right), \tag{2.14}$$

where $S = 4\pi a^2$ represents the surface area of the sphere. From the condition of $I_{\rm e}(\phi_{\rm f}) = I_{\rm i}(\phi_{\rm f})$, we obtain the equilibrium floating potential analytically as $\phi_{\rm f} = -1.42 k_{\rm B}T_{\rm e}/e$. The present test shows that for the small conducting sphere, even approximated by the limited number of orthogonal grid points, EMSES can calculate the floating potential correctly with an accuracy of 5–6 %.

Next, we focus on the sheath profile created around the conductor. There are a few theoretical approaches for the evaluation of the density profile in the sheath, particularly for ions. *Laframboise* [1966] derived a semi-analytical solution of the electron and ion densities around a spherical conductor. According to the theory, the electron density profile can be calculated by using the given potential profile in the sheath as follows:

$$\begin{aligned} n_{\rm e} \;=\;& e^{-\chi} - \frac{e^{-\chi_{\rm f}}}{\sqrt{\pi}}\left\{\sqrt{\chi_{\rm f}-\chi} + G\left(\sqrt{\chi_{\rm f}-\chi}\right)\right\} \\ & + \sqrt{1-{\rm x}^2}\cdot\frac{e^{-\chi_{\rm f}}}{\sqrt{\pi}}\left\{\sqrt{\chi_{\rm f}-\kappa} + G\left(\sqrt{\chi_{\rm f}-\kappa}\right)\right\}, \end{aligned} \tag{2.15}$$

$$\kappa \;=\; \frac{\chi - {\rm x}^2\chi_{\rm f}}{1-{\rm x}^2}, \tag{2.16}$$

where χ and $\chi_{\rm f}$ represent the normalized local and floating-body potentials $e\phi/k_{\rm B}T_{\rm e}$ and $e\phi_{\rm f}/k_{\rm B}T_{\rm e}$, respectively, and x is the non-dimensional inverse radial position a/r. The

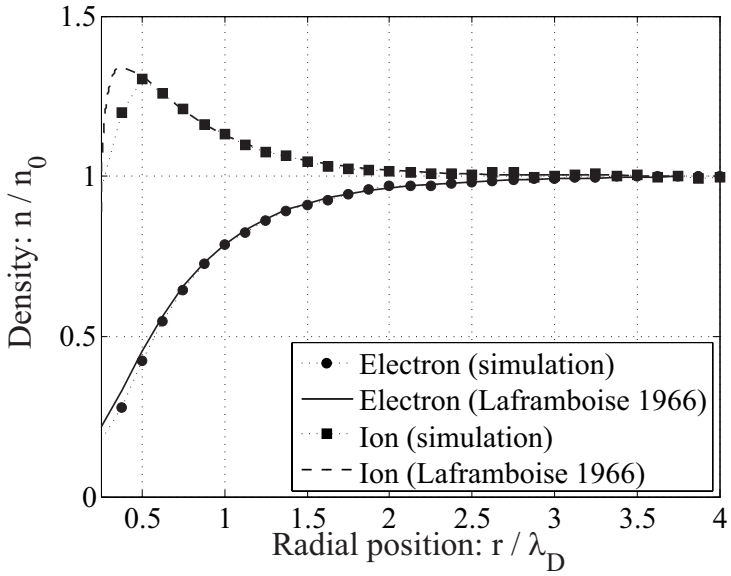

Figure 2.7: Electron and ion density profiles as a function of the radial position r. The profiles are obtained by EMSES and the semi-analytical approach developed by *Laframboise* [1966].

function $G(\xi)$ in Eq. (2.15) is defined using the error function $\mathrm{erf}(\xi)$ as

$$G(\xi) = \frac{\sqrt{\pi}}{2} e^{\xi^2} \left\{1 - \mathrm{erf}(\xi)\right\}. \tag{2.17}$$

Meanwhile, the semi-analytical expression of the ion density is given as

$$\begin{aligned} n_{\mathrm{i}} &= \sqrt{\frac{1-\mathrm{x}^2}{\pi}} \left\{\sqrt{-\kappa} + G\left(\sqrt{-\kappa}\right)\right\} \\ &+ \frac{1}{\sqrt{\pi}} \left\{\sqrt{-\chi} + G\left(\sqrt{-\chi}\right)\right\}. \end{aligned} \tag{2.18}$$

We calculate the density profiles using Eqs. (2.15) and (2.18) with the potential profile shown in Figure 2.6, and compare the semi-analytical profiles with the profiles numerically obtained by EMSES. In Figure 2.7, we plot electron and ion density curves obtained by EMSES and the semi-analytical approach. The profiles clearly show that the electron density decreases as the conductor surface is approached, while the ion density increases. Within $\sim 3\lambda_{\mathrm{D}}$ from the surface, the ion density is greater than the electron density. This region, in which the charge neutrality is broken, is a so-called ion sheath.

Figure 2.7 clearly shows that, except for the ion density at the closest grid points to the conducting surface, the sheath profile obtained by EMSES agrees well with that obtained by the semi-analytical approach. Near the conducting surface the semi-analytical ion density shows drastic change, which seems difficult to illustrate precisely with the limited number of grid points presently used in EMSES. To reproduce the finer ion density profile,

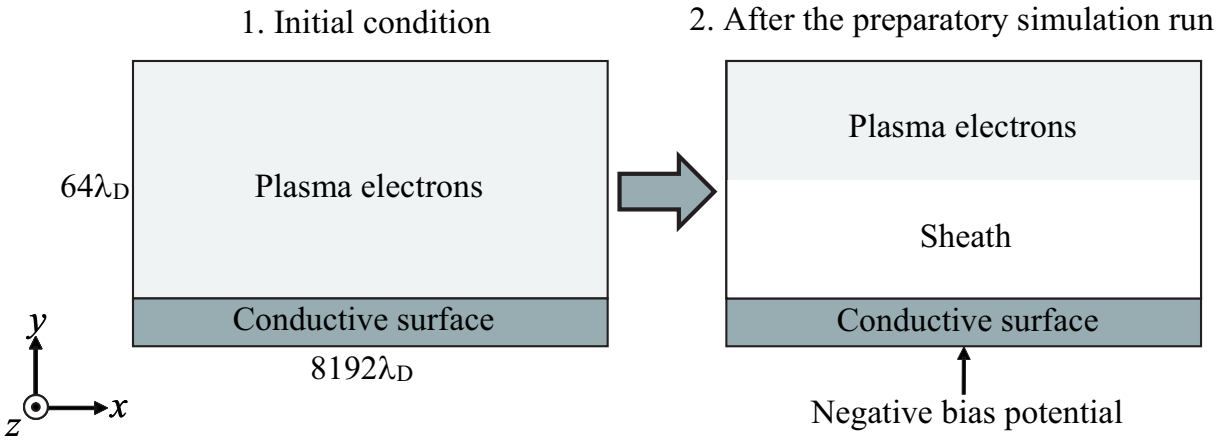

Figure 2.8: Two-dimensional simulation model for testing the dispersion relation of sheath waves. (a) Initially, we distribute plasma electrons uniformly except for on the conducting body and run a preparatory simulation, in which the conducting body potential is gradually biased negatively. (b) After the simulation, a stable profile of the plasma sheath is obtained as the right panel. Using the stable sheath, the dispersion relation of sheath waves is analyzed.

we require more grid points in the vicinity of the surface. However, the limitation of the grid points hardly perturbs the density profiles apart from the surface, and the correct sheath structure is overall obtained successfully by EMSES. Hence, the test outlined in this section confirms that EMSES has the capability to examine ES plasma environments, such as the sheath around a conductor.

2.4.2 Dispersion Relation of Sheath Waves

In order to validate EMSES for EM analysis, we focus on the EM environment in the vicinity of the conducting surface. We particularly examine the dispersion relation of EM wave modes called sheath waves, which propagate along the conducting body surface in a plasma sheath. For simplicity, we consider a sheath created on a planar conducting surface. The sheath consists of a thick electron-free region and a thin transition region. In the transition region, the electron density continuously varies from 0 to the background plasma density. It is known that the frequency range for the sheath waves is below the electron plasma frequency [*Laurin et al.*, 1989; *Morin and Balmain*, 1991; *Lüuttgen and Balmain*, 1996]. For comparison, we refer to a theory for the sheath waves described by *Lüttgen and Balmain* [1996]. They employed a cold plasma approximation and assumed a spatial step function for the electron density at the sheath–plasma interface. In the present test, we focus only on the isotropic case for simplicity.

Before examining the sheath wave properties, we performed a preparatory simulation for the formation of a plasma sheath. The model of a plasma sheath in two-dimensional

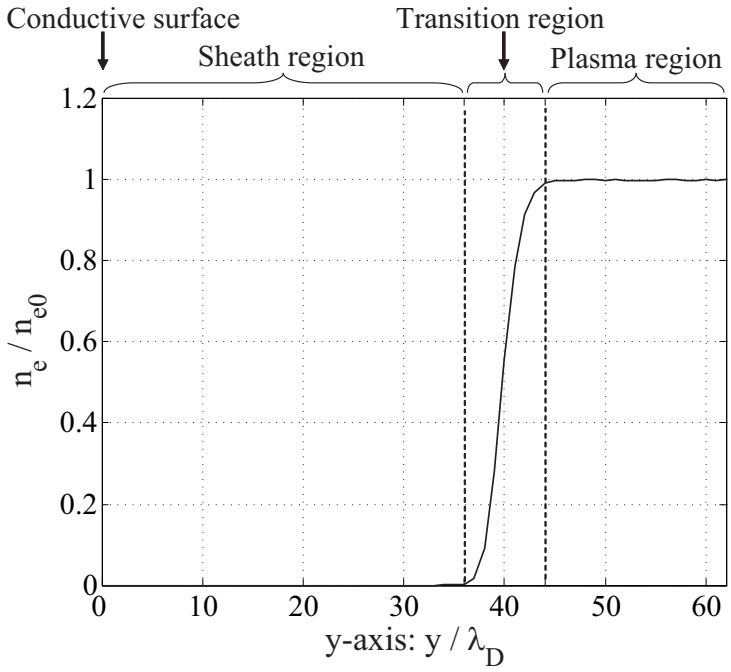

Figure 2.9: One-dimensional profile of the electron density of the stable plasma sheath as a function of distance from the conducting surface.

simulation space is shown in Figure 2.8. We consider a situation wherein plasma electrons impinge on a conducting surface in the $-y$ direction. Initially, we distribute the background plasma electrons uniformly in the background plasma region as shown in the left panel and start a simulation run. In the simulation, we apply a negative bias potential to the conducting surface and increase the potential value gradually over time. By this treatment, the sheath region is artificially expanded during the simulation run. The structure of the expanded sheath is saved at the end of the preparatory simulation and used in a simulation for the analysis of sheath wave properties. Note that we only solve the electron dynamics in the current analysis, because our interest is in the frequency range governed by the electron dynamics. For the boundary in the $+y$ direction, we employ a free boundary condition.

Figure 2.9 shows the electron density profile of the created sheath. It is confirmed that an electron-free region, the thickness of which is about 4.5 times the sheath–plasma transition region, is formed when a bias potential is applied: $\phi_\mathrm{b} \sim -800 k_\mathrm{B} T_\mathrm{e}/e$. For comparison with the theory, we introduce the effective sheath thickness s, which is defined as the distance between the conducting surface and the center of the sheath–plasma transition region. In the present simulation, $s = 40\lambda_\mathrm{D}$ is obtained.

Next, we run a simulation to analyze the dispersion relation for wave modes that exist in the sheath region. In the simulation, we maintain a constant bias potential of the

Table 2.1: Simulation parameters for the analysis of sheath waves. The values of $\omega_{\rm pe}$ and c are given in the normalized unit system used in EMSES.

Parameter	Value
Time step Δt	$0.025\,\omega_{\rm pe}^{-1}$
Grid spacing Δr	$0.05\,c\omega_{\rm pe}^{-1}$
Number of grid points $N_x \times N_y$	8192×64
Initial number of superparticles representing electrons	$128 N_x N_y$
Debye length $\lambda_{\rm D}$	$0.05\,c\omega_{\rm pe}^{-1}$
Electron plasma frequency $\omega_{\rm pe}$ (reference)	1
Speed of light c (reference)	20

conducting surface so as not to vary the created sheath structure. The parameters used in the present simulation are given in Table 2.1, in which we give the parameter values by setting the electron plasma frequency at $\omega_{\rm pe} = 1$ and the speed of light at $c = 20$ as references.

According to *Lüttgen and Balmain* [1996], EM waves, which are allowed to propagate in a sheath region, are transverse-magnetic (TM) mode. Therefore, we can obtain the dispersion relation for the waves by taking the Fourier transformation of the B_z component in the x direction and time. In performing the Fourier transformation, we use B_z data obtained only in the electron-free region.

The obtained dispersion relation is plotted in Figure 2.10. The result clearly shows a dispersion branch below $\omega_{\rm pe}$, which would not exist if there was no sheath because waves would be evanescent in the frequency range. It has been reported that the sheath wave cutoff frequency is $\omega_{\rm c} = \omega_{\rm pe}/\sqrt{2}$ [*Lüttgen and Balmain*, 1996]. The resultant dispersion curve shows an asymptotic characteristic for the cutoff frequency. Considering this agreement, we conclude that the dispersion curve obtained with EMSES can represent a sheath wave mode.

In the theory of sheath waves, the dispersion relation for the isotropic case is given as

$$\tanh(\alpha_{\rm s} s) = \frac{k_1}{K_0 \alpha_{\rm s}}, \tag{2.19}$$

where

$$\begin{aligned} \alpha_{\rm s}^2 &= k^2 - \beta_0^2 \\ k_1^2 &= k^2 - \beta_0^2 K' \\ K_0 &= K' = 1 - \omega_{\rm pe}^2/\omega^2 \\ \beta_0 &= \omega c, \end{aligned} \tag{2.20}$$

and ω and k represent wave frequency and a complex propagation constant, respectively [*Lüttgen and Balmain*, 1996]. We set $s = 40\lambda_{\rm D}$ and solve Eq. (2.19) numerically for the

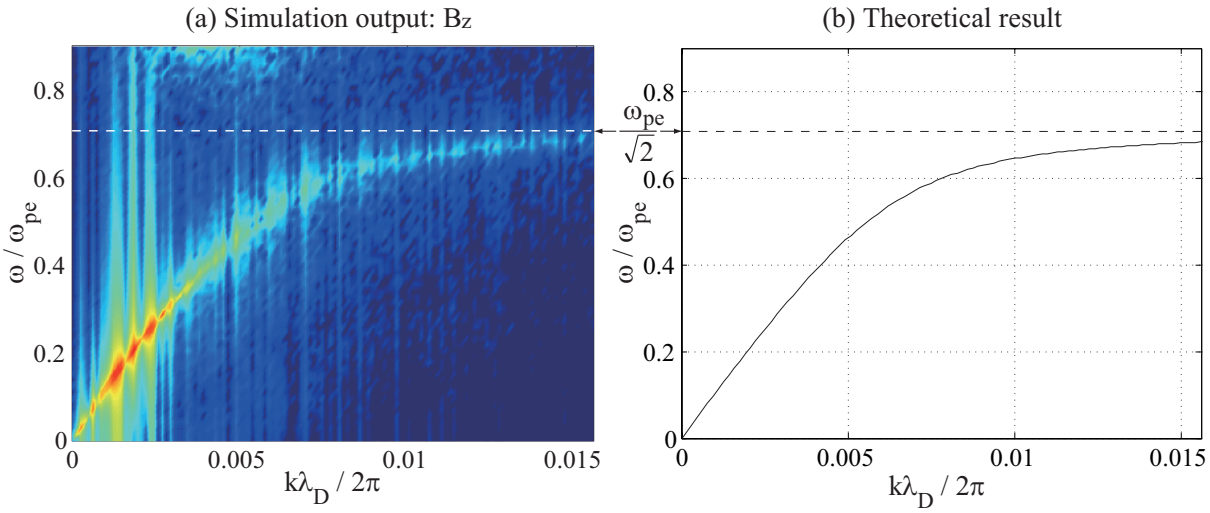

Figure 2.10: (a) ω–k diagram obtained in the simulation of the sheath environment. (b) Theoretical dispersion curve of the sheath wave for an isotropic plasma.

real part of k, the wave number. The resultant dispersion relation is plotted as a solid line in the right panel of Figure 2.10. The resultant dispersion curve agrees well with the theoretical curve.

The good agreement between the simulation and the theory confirms the validity of EMSES. Of course, we should consider the differences in the presuppositions between the simulation and the theory. Unlike the simplified assumption of the sheath structure introduced in the theory, the sheath examined in the simulation has a transition region where the density gradually changes. Also, the theory does not include any effects of non-linear responses of the electrons to the exiting EM field, unlike the simulation. However, the present simulation condition of a much thinner transition region than the electron-free region should minimize the influence of the transition region on the sheath wave properties. Moreover, because we run the present simulation without any external wave source, which is a very quiet condition, non-linear effects of the plasma electrons can be negligible. By testing under these conditions, we conclude that EMSES successfully reproduces the EM environment in the plasma region in the vicinity of a conducting surface.

In more practical situations in space, e.g., in a condition where a conductor has a floating potential, the transition region can dominate the entire sheath structure, as shown in the result described in Section 2.4.1. For such a case, the theoretical approach is difficult to apply to sheath wave problems, because the step-function model for the sheath structure cannot be employed. The property of sheath waves in such a case is a very interesting subject for future research using EMSES.

2.5 Summary

By combining boundary treatments for conducting spacecraft surfaces with the EMPIC simulation technique, we have developed EMSES for self-consistent analysis of spacecraft–plasma interactions on the EM basis.

The major additions introduced in EMSES relate to boundary conditions required for the longitudinal and transverse components of the electric field. For the longitudinal component, (1) we consider the contribution of charge accumulation at the conducting surface caused by impinging or emitted particles and (2) we redistribute the charge so that the perfect conducting surface has an equipotential. The former requirement (1) is realized automatically in the updates of the charge density and the electric field using the current density data. For this, we have adopted a special treatment for the current density calculated around the spacecraft surface, such that the charge accumulation at exact locations on the spacecraft surface is successfully realized. For item (2), we applied the conventional Capacity Matrix method, which assures perfect-conductor conditions for the longitudinal electric field component. With respect to the transverse electric field component, we simply set the field values to zero for components inside and tangential to the spacecraft surfaces. The above treatments are appropriately taken in a computational cycle of the EM-PIC simulation of EMSES.

The methods presented here provide the basis for self-consistent reproduction of the EM as well as ES environments in the presence of conducting spacecraft bodies. The application of EMSES to more specific problems is possible by introducing an additional numerical model, e.g., an electric field antenna on a scientific spacecraft. Future work can be devoted to expanding the applicability of the code to various problems including broad scale length ranges by introducing appropriate modifications, e.g., a locally-refined mesh [*Fujimoto and Machida*, 2006] in the vicinity of the spacecraft or regions governed by plasma dynamics of small scale, in order to conduct computations within a practical time.

Chapter 3

Impedance of a Dipole Antenna Surrounded by an Ion Sheath

3.1 Introduction

When a plasma contacts with solid surfaces of an antenna with a plasma potential, there must be a flow of electrons and ions into the surfaces. In a usual situation of a plasma consisting of equal numbers of electrons and positive ions, the electrons are far more mobile than the ions. It follows that the antenna charged negatively with respect to the plasma potential. Then, the negative potential at the surfaces recovers the plasma potential through a positively charged region formed between the antenna surfaces and the neutral plasma region. This non-neutral, positively charged region is called a sheath, particularly an ion sheath, because the positive charging is usually realized by an ion-rich condition. The potential difference created between the antenna surfaces and the neutral plasma region allows the flow of electron and ions into the surfaces to be balanced. As a result, the equilibrium potentials are formed for the antenna.

An ion-sheath effect on antenna impedance has received a great deal of attention for its application to rocket exploration of the ionosphere using the impedance probe [*Oya*, 1966]. Since an ion sheath has much different electrical properties than a background plasma, it can obviously modify the characteristics of an electric antenna surrounded by the sheath. Actually, some rocket observations have indicated that the sheath has prominent influences on the antenna impedance [*Oya and Obayashi*, 1966]. As briefly described in Section 1.2.2, the presence of an ion sheath introduces an impedance resonance called a sheath resonance. Furthermore, it is generally known that a low-frequency capacitance of the probe equals to a capacitance of the ion sheath itself. Since some researchers have tried to make use of such a sheath capacitance for the temperature diagnosis of ionospheric electrons [*Oya and Aso*, 1969], precise knowledge of the ion-sheath effect has become an increasingly important issue.

Since the presence of an ion sheath is an even more inevitable problem for bounded

plasmas, there exists plentiful literature regarding sheath properties in the field of laboratory and processing plasmas [e.g., *Lieberman and Lichtenberg*, 1994]. Also, the dynamic properties of the ion sheath have been studied in the field of active experiments [e.g., *Calder et al.*, 1993]. Meanwhile, in an aspect of the ion sheath effects on the antenna impedance of space-based antennas, it has been simply regarded as a vacuum layer in a frequency range in which ions are assumed to be immobile. However, even if one uses the immobile ion assumption, the inclusion of inhomogeneity caused by the ion sheath leads to much complication in theoretical derivation of the antenna impedance. Therefore, most previous theoretical analyses of the antenna impedance have been carried out only for much simplified sheath configuration such as planar and cylindrical structures. Recently, *Béghin and Kolesnikova* [1998] proposed a numerical approach using the Surface-Charge-Distribution (SCD) method, which can consider all of the boundary surfaces involving ion-sheath interfaces around antenna and satellite bodies with complex geometries. Even in the SCD method, however, the ion-sheath interfaces should be given as parameters of the numerical tool.

In comparison with the above approaches, the Particle-In-Cell method clearly has large advantage for detailed investigations of ion-sheath properties; since the dynamics of individual electrons and ions is solved simultaneously in the approach, we can obtain a self-consistent solution for the structure of an ion sheath. The structure of an ion sheath has already been investigated using an ES-PIC method in previous studies [*Tu et al.*, 2008]. In the present chapter, we focus on an ion-sheath effect on antenna characteristics rather than the sheath structure itself by examining the impedance of an electric antenna surrounded by an ion sheath using an EM-PIC approach (EMSES developed in the previous chapter).

Before the sheath analysis, this chapter has an important role to demonstrate the application of EMSES to an antenna analysis. Therefore, we first examine the dipole antenna impedance without considering any effects of an ion sheath and compare obtained results to the conventional kinetic theories [e.g., *Schiff*, 1970; *Meyer-Vernet and Perche*, 1989]. We particularly focus on the impedance of a low-power transmitting antenna. The impedance calculation is fundamental and useful for the validation. The transmitted power is small enough not to disturb the boundary environment of the simulation box so that numerical errors caused by the boundary effects are minimized. We consider a very simple situation in which a set of dipole antenna is immersed in Maxwellian, unmagnetized, and collisionless plasma. The plasma is so dense and low-temperature that the Debye length becomes smaller than the antenna length. After the validation of EMSES, we analyze the impedance characteristics of antennas covered with an ion sheath, which is created under the condition that an antenna has a floating potential [*Miyake et al.*, 2008a]. We focus on the impedance change due to the inclusion of the ion sheath effect. We also discuss the dependence of sheath capacitance on the sheath thickness by

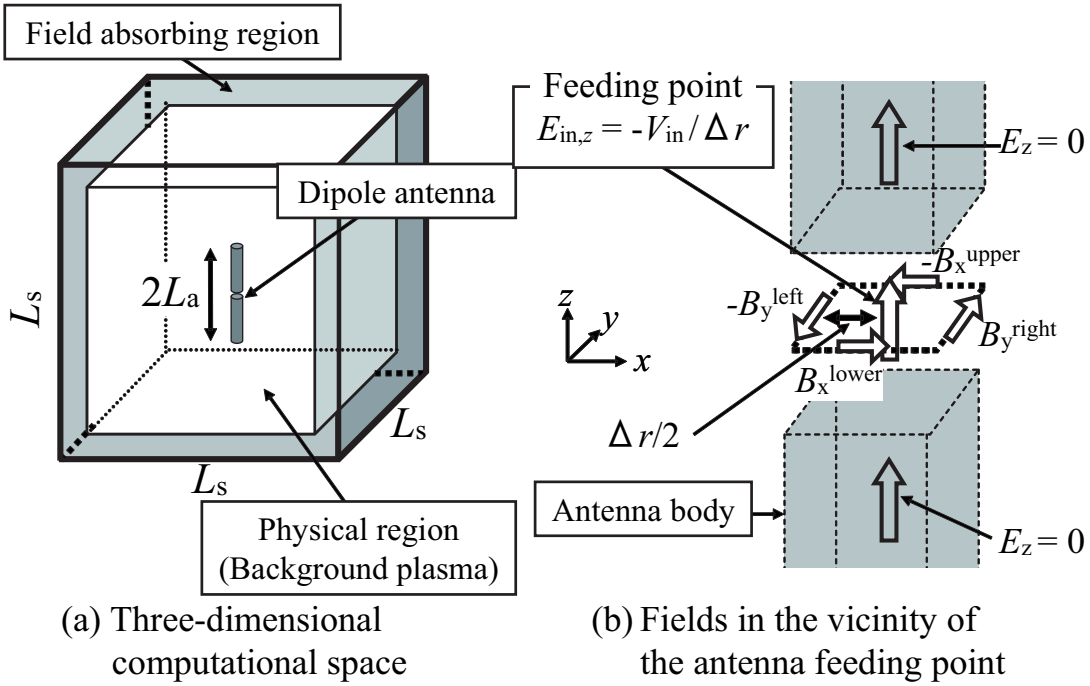

Figure 3.1: Model of the numerical simulation. (a) The dipole antenna is placed at the center of the simulation box. (b) The electric field $E_{\mathrm{in},z} = -V_{\mathrm{in}}/\Delta r$ is provided at the gap between two antenna elements.

the simulations with different DC bias potentials.

3.2 Application of EMSES to the Antenna Analysis

3.2.1 Simulation Model

The simulation system is shown in Figure 3.1. We consider a three-dimensional simulation box and place a dipole antenna at its center. The simulation box is uniformly filled with mobile electrons and ions with finite thermal velocities at the initial state of a simulation run. Since our interest in the present study is in antenna impedance in a frequency range near the electron plasma frequency, the motion of ions has little effects on the antenna impedance itself. However, ion dynamics cannot be neglected to achieve a steady-state profile of the plasma environment around the antenna. We assumed that the ion species is a proton and employed the real mass ratio of the protons to the electrons, i.e., 1836, in the present analysis.

The boundary condition of the simulation box should be carefully selected in order to realize an isolated system. In the present analyses, two types of boundary conditions are

utilized: the boundary conditions for EM and ES components. For EM component, field absorbing region for the outgoing wave is necessary to realize an isolated system. We set the field absorbing region based on Masking method [*Tajima and Lee*, 1981] consisting of 8 grids from the edge of the box in order to prevent the field reflection at the boundary. When we solve Poisson's equation for ES component, the Neumann condition is used. The particles which reach the edge of the simulation region are reflected back into the region. In the current analysis, we set the edge of the simulation box sufficiently far from the sheath region. This indicates that the perturbation of plasma density around the antenna never reaches the outer boundaries of the simulation box. In this condition, since the flux escaping from the simulation box is equal to the particle flux in the unperturbed background plasma, the reflecting boundary condition for particles can be substituted for a particle-loading scheme that is known as a rigorous open boundary condition for escaping particles. By combining the above treatments, we realized the isolated system of the simulation.

3.2.2 Antenna Treatment

In the present analysis, we assumed that the antenna bodies are made of perfect conductors for simplicity. Although the basic ideas for the introduction of perfect conductors in the simulation system have been already described in the previous chapter, we also employ a number of particular treatments optimized for the antenna analysis, which might contain slight difference from those described in Chapter 2. For example, in order to model the antenna conducting bodies, we set the values of electric field $E_z = 0$ defined along only one column of grid points, except for the gap between the two antenna elements, as shown in Figure 3.1. This treatment is to realize a very thin wire dipole antenna in the EMSES code.

Another important issue that should be carefully considered is treatments for particles which impinge into the antenna bodies. In the present chapter, we use two types of the treatments. In the first treatment, the antenna surfaces are perfectly transparent with respect to the plasma particles, which can pass through the antenna location. This treatment corresponds to a mesh-like antenna model that was widely used in previous related studies [e.g., *Schiff and Fejer*, 1970]. Note that, if this model is used in the particle simulation, inhomogeneous plasma environment such as an ion sheath is not naturally created. We, therefore, used the model for antenna analyses in uniform plasma.

In the second treatment, the physical existence of the antenna body is taken into consideration by introducing the internal non-plasma boundaries in the simulation system. The most important feature of this treatment is that a sheath is created as the result of plasma-body interactions, and thus this treatment is more practical than the first treatment. We, therefore, applied the second concept to cases of the ion-sheathed antenna.

Practically, since the minimum spatial unit is one cubic cell with Δr^3 volume, the cross-section of antenna is assumed to be one zone squared with Δr^2 area, where Δr is a grid spacing in the EMSES code. In the present simulation model, the antenna line is composed of a series of the cubic cells, and particles whose centers move into the cell boundary are absorbed in the antenna. The charge collected by the antenna is redistributed on the grid line in the antenna body on which the z-components of the electric field E_z are defined (see Figure 3.1), so that an equipotential solution on the antenna body is realized. For this purpose, we use the Capacity Matrix method as explained in Section 2.3.4. After we redistribute the surface charge, we correct the electrostatic field by solving Poisson's equation considering the modified surface charge. By this treatment, the contribution of collected particles on the charging of the antenna body can be precisely evaluated. For the outside of the antenna territory, the particle motion is advanced by linearly interpolating the field values at the particle position from the adjacent grid points, which is the scheme commonly used in PIC plasma simulations [e.g., *Matsumoto and Omura*, 1993].

One of the most significant functions added to EMSES for the antenna analysis is a treatment of an antenna feeding point, which is located at the gap between two antenna bodies. We analyzed the impedance characteristics of the transmitting antenna with a small applied signal. To simulate the transmitting antenna, we used the delta-gap feeding technique [e.g., *Luebbers et al.*, 1992]. In this method, the dipole antenna is fed with an input voltage $V_{\rm in}$, which is realized by providing an electric field $E_{{\rm in},z}$ at the gap between two antenna elements as follows:

$$E_{{\rm in},z} = -\frac{V_{\rm in}}{\Delta r}. \tag{3.1}$$

To obtain the input impedance of the antenna, we need to know the current $I_{\rm in}$ at the antenna feeding point. $I_{\rm in}$ is obtained by the rotation of the magnetic field around the feeding point. Numerically, $I_{\rm in}$ is computed with

$$I_{\rm in} = \left\{ (B_x^{\rm lower} - B_x^{\rm upper}) + (B_y^{\rm right} - B_y^{\rm left}) \right\} \frac{\Delta r}{\mu_0}, \tag{3.2}$$

where μ_0 represents the permeability in vacuum, and $B_x^{\rm lower}$, $B_x^{\rm upper}$, $B_y^{\rm right}$, and $B_y^{\rm left}$ are the magnetic fields which are defined at the adjacent grids to the feeding point, as shown in the right panel of Figure 3.1. $V_{\rm in}$ and $I_{\rm in}$ are first obtained in the time domain and are then transformed to the frequency domain by Discrete Fourier Transform (DFT). The input impedance Z of the antenna is obtained from

$$Z(\omega) = \frac{V_{\rm in}(\omega)}{I_{\rm in}(\omega)}, \tag{3.3}$$

where $V_{\rm in}(\omega)$ and $I_{\rm in}(\omega)$ represent the voltage and current, respectively, at the feeding point in the frequency domain.

Table 3.1: Simulation parameters for the analysis of antenna impedance. The values are given in a normalized unit system used in EMSES.

Parameter	Symbol	Value
System		
Grid spacing	Δr	1
Time step	Δt	0.02
Speed of light	c	25
System length	L_s	64
Number of superparticles per cell		512
Dipole antenna		
Frequency at which the antenna operates as the half-wave dipole	$\omega_{\rm half}$	$\sim$3.3
Antenna half length	l_a	12
Antenna width in x and y directions (See Figure 3.1 for an antenna configuration.)		1
Background plasma electrons		
Plasma frequency	$\omega_{\rm pe}$	1
Inertial length	$c/\omega_{\rm pe}$	25
Thermal velocity (variable)	v_0	1–2
Debye length (variable)	$\lambda_{\rm D}$	1–2

In order to obtain the antenna characteristics over a large frequency range in a single run of the simulation, we utilized a broad spectrum pulse given as $V_{\rm in} = V_a(d/dt)$ $[(t/T)^4 \exp(-t/T)]$ where V_a and T are parameters of the pulse, and t/T represents the normalized time. The dominant spectral frequency ω_d of the pulse is given as $\omega_d = 0.152 \times 2\pi/T$ and was set close to the electron plasma frequency.

One should note that the antenna surface current is not artificially given but obtained by calculating the rotation of the magnetic field around the antenna body. The profile of the magnetic field around the antenna body is self-consistently solved so that the electric field satisfies the appropriate boundary conditions in the antenna body as explained above. As a result, we can evaluate the antenna impedance without any assumptions on the current distribution on the antenna surface.

3.2.3 Common Parameters for the Antenna Analysis

Table 3.1 shows common parameters used in the present simulations. A grid spacing and a time step are determined appropriately so that the Courant condition for the light-wave mode is safely satisfied. In the present analysis, we have $64\times64\times64$ cells and 512 particles per cell; namely $64 \times 64 \times 64 \times 512 = 134{,}217{,}728$ particles in the entire system.

In the present paper, we set our goal to examine the impedance characteristics in collisionless-isotropic plasma environment. The parameters listed in Table 3.1 are given

in a renormalized unit system used in the simulation tool. In this case, the outputs are obtained as the ratio of the antenna impedance to the characteristic impedance of free space $\sqrt{\mu_0/\epsilon_0}$, where ϵ_0 represents the permittivity in vacuum. The impedance values in the real physical unit are calculated using the relation $\sqrt{\mu_0/\epsilon_0} = 120\pi\,\Omega$. Hence, all the results for the impedance are given in the unit of Ω in the present paper.

One of the important parameters is the ratio of the antenna length to the free-space wavelength in the frequency range of interest. In the present study, the frequency range of our interest is near the electron plasma frequency and is located well below the frequency at which the antenna operates as a well-known half-wave dipole. From this point of view, we treat the "electrically short antenna" in comparison with the free-space wavelength. In practice, the "electrically short antenna" regime is valid in most of solar-terrestrial regions except in very dense plasmas (10^5–$10^6\,/\mathrm{cm}^3$) in ionosphere, where the electron plasma frequency is so large that the free-space wavelength at the frequency becomes in the order of 10–100 m.

The ratio of the antenna length to the Debye length of the background plasma is also important. The impedance resonance in plasma becomes remarkable when the antenna length is significantly larger than the Debye length, as was predicted by the previous theory [*Meyer-Vernet and Perche*, 1989]. We, therefore, chose the plasma parameters so that the antenna has a length greater than the Debye length in the present study.

3.3 Antenna Impedance in Uniform Plasma

3.3.1 Comparison with the Conventional Theory

In order to validate the developed EM-PIC simulation tool, we examined the antenna impedance by using the transparent-antenna modeling, with which an ion sheath is not created around the antenna as described in Section 3.2.2. The results are compared with the conventional kinetic theory which was developed by e.g., *Schiff* [1970]. In the theory the impedance is formulated based on the induced Electro-Motive-Force (EMF) method using Maxwell's equations and the linearized Vlasov equation as basic equations in the quasi-static limit. The formula for the antenna impedance Z in a plasma is then written as

$$Z = \frac{j}{(2\pi)^3\omega\epsilon_0|I_0|^2}\int \frac{(\boldsymbol{k}\cdot\boldsymbol{J}_\mathrm{s})(\boldsymbol{k}\cdot\boldsymbol{J}_\mathrm{s}^*)}{\boldsymbol{k}\cdot(\epsilon_\mathrm{p}\cdot\boldsymbol{k})}\,d\boldsymbol{k}, \tag{3.4}$$

where $\boldsymbol{J}_\mathrm{s}$, I_0, ω, and $\boldsymbol{k}$ are the antenna current distribution, the antenna current evaluated at the antenna feeding point, the frequency, and the wave number vector, respectively. The asterisk denotes the complex conjugate. In order to adopting the normalized parameters

listed in Table 3.1, we used the normalized form of Eq. (3.4) that is given as

$$\begin{aligned} \frac{Z}{Z_0} &= \frac{j}{(2\pi)^3}\int \frac{(\boldsymbol{y}\cdot\boldsymbol{J}_{\rm n})(\boldsymbol{y}\cdot\boldsymbol{J}_{\rm n}^*)}{\boldsymbol{y}\cdot(\epsilon_{\rm p}\cdot\boldsymbol{y})}\,d\boldsymbol{y}, \\ \boldsymbol{J}_{\rm n} &= \frac{\boldsymbol{J}_{\rm s}}{|I_0|}, \\ \boldsymbol{y} &= \frac{c}{\omega}\boldsymbol{k}, \end{aligned} \tag{3.5}$$

where $Z_0 = \sqrt{\mu_0/\epsilon_0}$ and c represent the characteristic impedance of free space and the speed of light, respectively. In Eqs. (3.4) and (3.5), $\epsilon_{\rm p}$ is the plasma dielectric tensor and can be decomposed to the longitudinal and transverse components $\epsilon_{\rm L}$ and $\epsilon_{\rm T}$ as scalar values in an isotropic case [*Stix*, 1992]. Of them, the longitudinal component becomes a dominant factor characterizing the impedance change in the plasma environment from the free-space value [*Schiff*, 1970]. Hence, we consider only contribution of $\epsilon_{\rm L}$, which is given in the kinetic theory as

$$\epsilon_{\rm L} = 1 - \frac{\omega_{\rm pe}^2}{k^2 v_0^2} Z_{\rm p}'\left(\frac{\omega}{k v_0}\right), \tag{3.6}$$

where v_0, $\omega_{\rm pe}$, and $Z_{\rm p}$ represent the electron thermal velocity, the electron plasma frequency, and the plasma dispersion function, respectively, as discussed by *Fried and Conte* [1961]. Note that $\epsilon_{\rm L}k^2 = 0$ gives the dispersion relation for plasma longitudinal waves.

For the theoretical comparisons with the simulation results, we adopted the assumption of the triangular current distribution on the antenna surface in analytically evaluating Eq. (3.4). In the parameters used in the present analysis, the antenna length is smaller than the electron inertial length $c/\omega_{\rm pe}$. Physically, $c/\omega_{\rm pe}$ means the skin depth of an evanescent wave mode below $\omega_{\rm pe}$. When $c/\omega_{\rm pe}$ is much larger than the antenna length, the triangular current approximation is known to be appropriate in the computation of the conventional theory for the antenna impedance [*Bell et al.*, 2006]. In upper panels of Figure 3.2, we plot the theoretical curves in solid lines. Panels I-(Re) and I-(Im) show the resistance and reactance, which are the real and imaginary parts, respectively, of the impedance. In Panel I-(Im), we also superimpose the theoretical value of free-space antenna reactance, which is evaluated by the formula $(-1/\pi\omega\epsilon_0 l_{\rm a})[\ln(l_{\rm a}/a) - 1]$ where $l_{\rm a}$ and a represent the half length (not the tip-to-tip length $L_{\rm a}$) and the radius of the dipole antenna, respectively [*Schelkunoff and Friis*, 1952]. The impedance value is plotted as a function of a normalized frequency $\omega/\omega_{\rm pe}$.

Meanwhile, we run EM-PIC simulations using the parameters listed in Table 3.1 and computed the antenna impedance by the method presented in Section 3.2. Note that the form of the current distribution was never assumed but evaluated self-consistently in the simulations. We examined a case with the Debye length of background plasma: $\lambda_{\rm D} = l_{\rm a}/12$. The obtained simulation results are shown in solid lines in Panels II-(Re)

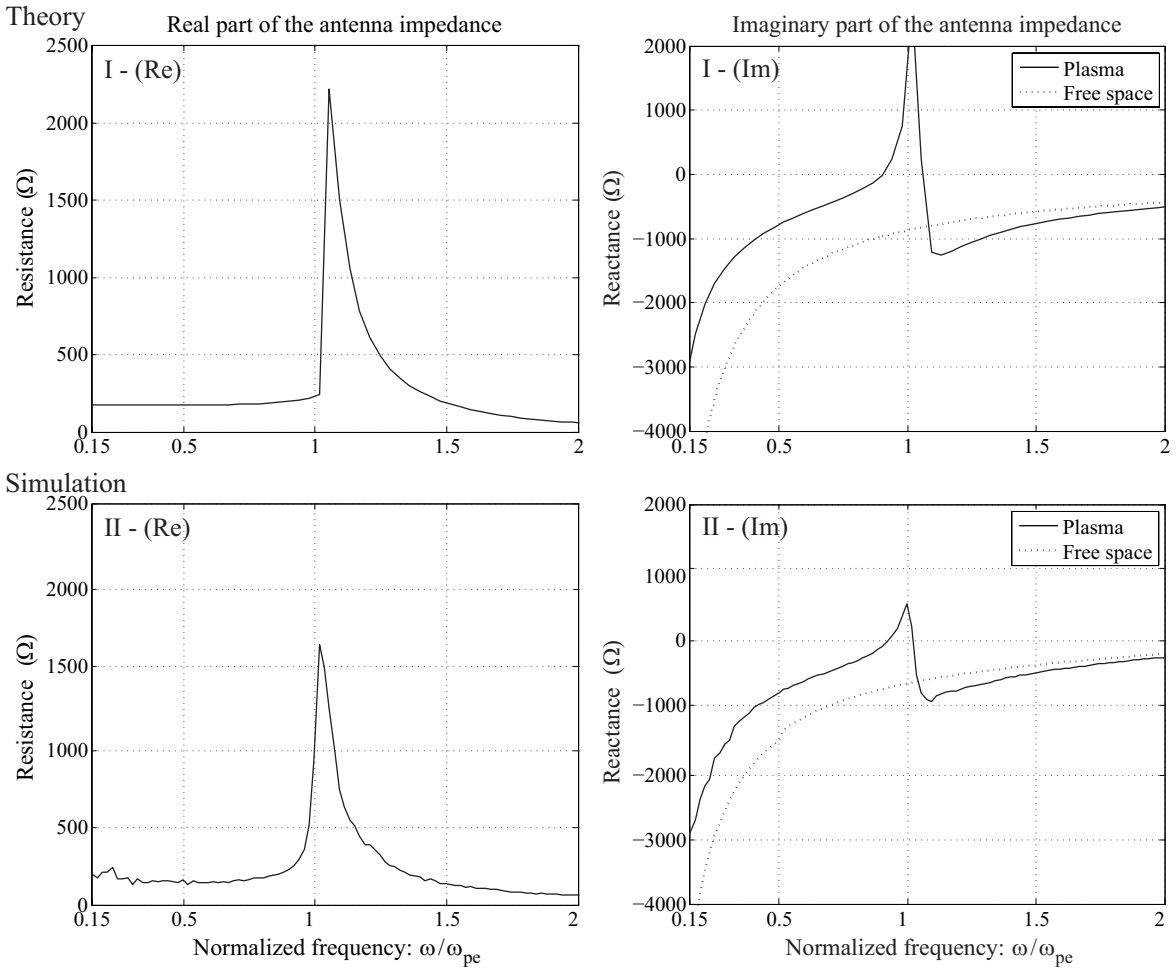

Figure 3.2: Comparison of the antenna impedance in uniform plasma obtained by the conventional kinetic theory and the EMSES code. Upper panels (I-(Re) and I-(Im)) represent the theoretical result of antenna resistance and reactance, respectively, for the case of $\lambda_{\rm D} = l_{\rm a}/12$. Lower panels (II-(Re) and II-(Im)) represent the EM-PIC results of antenna resistance and reactance, respectively. The dotted lines in panels I-(Im) and II-(Im) represent the free-space reactances, which are calculated theoretically and numerically (with a free-space FDTD simulation), respectively.

and II-(Im) of Figure 3.2 in the same manner as the theoretical curves. Also in Panel II-(Im), we superimpose the free-space value of antenna reactance that is obtained by the simulation of the free-space case.

As clearly shown in comparison between the solid lines in the upper and lower panels, the impedance profiles basically show agreement between the theoretical and simulation results. The major points of the agreements are, (1) the resistance has a finite and constant value below $\omega = \omega_{\rm pe}$, (2) the reactance value is larger than the free-space value below $\omega = \omega_{\rm pe}$, (3) the drastic variation of the impedance values is observed near $\omega = \omega_{\rm pe}$, and (4) the impedance tends to the free-space value well above $\omega = \omega_{\rm pe}$. The interpretations of these effects will be described briefly in the preceding subsection. On the other hand,

a discrepancy is clearly seen between the theoretical and EM-PIC results near $\omega = \omega_{pe}$. The intensity of the impedance resonance is greater in the theoretical results than those of EM-PIC simulation, which is seen in both real and imaginary parts but more remarkable for the imaginary part. The possible reason causing this discrepancy will be discussed in Section 3.5. Although the above disagreement is found, we basically confirm that the physical behavior of the antenna impedance in the plasma can be qualitatively evaluated by the developed tool.

3.3.2 Dependence of Antenna Impedance on Debye Length

In order to examine the dependence of the antenna impedance on the Debye length of the surrounding plasma, we performed an additional EM-PIC simulation for the case of $\lambda_D = l_a/6$. The obtained result for $\lambda_D = l_a/6$ case is superimposed as dashed lines in addition to $\lambda_D = l_a/12$ case in Figure 3.3. One should note that we did not change the plasma density in these two cases. In this situation, doubling the Debye length indicates quadrupling the temperature at the constant density.

As shown in Figure 3.3(a), the resistance has a finite and almost constant value for each case in the frequency range lower than ω_{pe}. In free space, the resistance should be less than $5\,\Omega$ for $\omega < \omega_{pe}$ and the given antenna length [*Stutzman and Thiele*, 1997] since there is few radiation of the electromagnetic wave from the electrically short antenna. In kinetic plasma, however, the conversion of field energy excited by the antenna into the kinetic energy of the plasma electrons causes the dissipation, which leads to the equivalent resistance for $\omega < \omega_{pe}$ [*Kuehl*, 1967]. The result confirms that wave-plasma interactions around the antenna are correctly evaluated in the present simulation. We can also see that the resistance is larger in the case of $\lambda_D = l_a/12$ corresponding to the smaller Debye length case. This dependence was also confirmed by the conventional kinetic theory although not displayed.

Near $\omega = \omega_{pe}$, the large peak of the resistance value is observed, which is particularly remarkable in the case of $\lambda_D = l_a/12$. In the case of $\lambda_D = l_a/6$, the similar signature is recognized, but the peak value is lower than the case of $\lambda_D = l_a/12$. This characteristic variation of the impedance value has been referred as the impedance resonance. The enhancement of the impedance value corresponds to the presence of the poles $\boldsymbol{k}\cdot(\epsilon_L\cdot\boldsymbol{k}) = 0$ in the analytic expression of Eq. (3.4), which also gives the dispersion relation of the plasma wave mode. The impedance resonance, therefore, is considered to have much relevance to the strong interactions between the antenna and the plasma wave mode. In the present case the corresponding plasma wave is the Langmuir wave. The reduction of the peak value due to a high temperature, which corresponds to the case of the larger Debye length, was also confirmed by the theory. Another feature we can find near $\omega = \omega_{pe}$ is that the peak frequency of the resonance is shifted to higher frequency for the case of

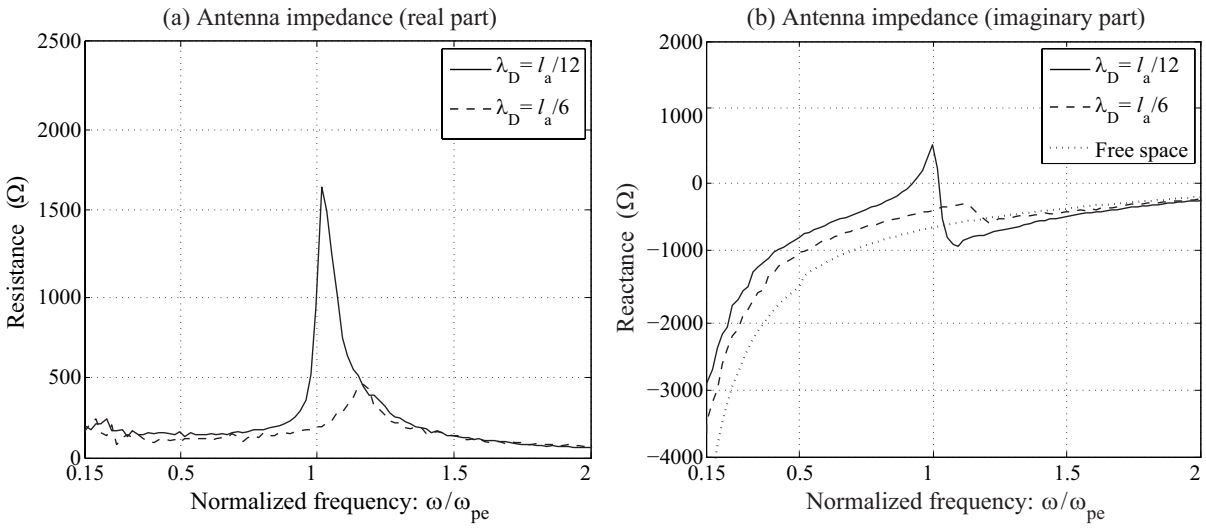

Figure 3.3: Antenna resistances (left panel) and reactances (right panel) in a uniform plasma in cases of the small and large Debye lengths. The dotted line in the right panel represents the free-space reactance.

$\lambda_D = l_a/6$ in comparison with the case of $\lambda_D = l_a/12$. This resonance shift was not shown in the conventional theory. There are several possible reasons for this frequency shift, which will be discussed in Section 3.5.

As to the reactance shown Figure 3.3(b), the absolute value of the reactance below $\omega = \omega_{pe}$ is smaller than its free-space value. This means that the antenna capacitance, defined as $C = -1/(\omega X)$, where X is the reactance, becomes greater in the plasma than in free space. The simulation results show that the antenna capacitance is larger for $\lambda_D = l_a/12$ case than for $\lambda_D = l_a/6$ case. This feature can be explained by an analogy with a capacitor separated by dielectric material with a large permittivity. In Eq. (3.6), the real part of the derivative of the plasma dispersion function Z_p takes a negative value in a low-frequency limit [*Fried and Conte*, 1961]. Therefore, the value of the dielectric function ϵ_L in the finite-temperature plasma is larger than unity at the low-frequency range. If we apply to an analogy that an antenna consists of two elements separated by a dielectric with a permittivity larger than ϵ_0, it makes sense that the antenna capacitance is larger in the plasma in the low-frequency range. When we consider large v_0 which implies a situation of high temperature of plasma, the corresponding ϵ_L approaches to unity, and the capacitance tends to its free-space value.

Near $\omega = \omega_{pe}$, the reactance also shows the signature of the impedance resonance, at which the reactance is maximum. The remarkable feature found in the simulation results is that the intensity of the impedance resonance is much weakened in the case of $\lambda_D = l_a/6$. As mentioned in the interpretation of the resistance peak near $\omega = \omega_{pe}$, the impedance resonance is considered to be caused by the strong wave-antenna interactions. The plasma wave component that has a wavelength smaller than the local Debye length

is readily damped, and thus large λ_D/l_a leads to the reduction of wave components which can interact with the antenna. Therefore, in the case of $\lambda_D = l_a/6$, the impedance resonance becomes weaker than the $\lambda_D = l_a/12$ case. The same tendency was shown in the theoretical calculations.

In the frequency range above ω_{pe}, the antenna impedance should recover its free-space value simply because the plasma dielectric function recovers its free-space value in the frequency range well above ω_{pe}. This signature is confirmed in the theoretical results (see Panels I-(Re) and I-(Im)). Also in the EM-PIC results, it is confirmed that the resistance and the reactance tend to approach their values in free space in both cases of the Debye length. Therefore, the impedance behavior above ω_{pe} is correctly evaluated by the developed EM-PIC tool.

3.4 Analysis on an Ion-sheathed Antenna

In previous studies on antenna impedance [e.g., *Oya*, 1965], simplified models were commonly used for the plasma environments around antennas; e.g., an ion sheath created around the antenna surface was assumed to have an abrupt jump in electron density at the interface between the sheath and the uniform plasma. However, for higher accuracy and applicability to complex plasma environments which will be encountered in real space missions, it is important to establish a method of including the ion sheath of which the structure is solved by self-consistent analysis in consideration of antenna-plasma interactions. By taking advantages of the PIC simulation, we performed the impedance analysis simultaneously solving the dynamics of an ion sheath created around the antenna body. The analysis consists of two steps. First, we run a simulation without the delta-gap feeding with sufficient time steps so that the static structure of an ion sheath is created. In Section 3.4.1, we present the static structure of the created ion sheath obtained as a steady state. After that, we proceed to impedance analysis using the delta-gap feeding technique, maintaining the created sheath structure. The result of the impedance analysis is described in Section 3.4.2.

3.4.1 Structure of an Ion Sheath

As a steady state, we obtained floating potential values $\phi_F = -3.4k_BT_e/e$ and $-2.9k_BT_e/e$ for the cases of $\lambda_D = l_a/12$ and $l_a/6$, respectively. Here, k_B, T_e, and e represent Boltzmann's constant, the electron temperature, and the electric unit charge, respectively. In an isothermal plasma, i.e., $T_e = T_i$ where T_i represents the ion temperature, *Fahleson* [1967] theoretically evaluated the floating potential as $\phi_F = -(k_BT_e/e)\ln\sqrt{m_iT_e/m_eT_i} \sim -3.8k_BT_e/e$ in a condition that conductor dimensions are sufficiently larger than λ_D. Here, m_e and $m_i = 1836m_e$ represent the mass of electrons and protons, respectively. In the

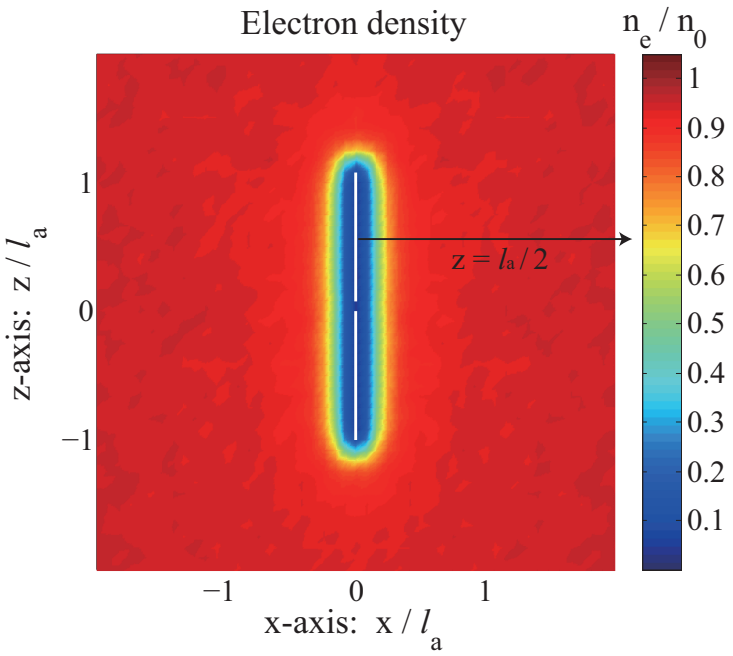

Figure 3.4: Spatial profile of the normalized number density of electrons in the x-z plane, which includes the center of the antenna in the case of $\lambda_D = l_a/12$. n_0 represents the background level of the electron number density.

present case, however, the antenna radius is small and comparable to λ_D. Therefore, *Fahleson*'s theory may not be applicable. Although the floating potential of a cylindrical conductor with a comparable radius to λ_D is generally difficult to formulate, its magnitude becomes smaller than that obtained with *Fahleson*'s theory and should decrease with the ratio of the conductor's radius to λ_D [*Mott-Smith and Langmuir*, 1926]. These tendencies basically agree with those obtained in the current simulations stated above.

Figure 3.4 shows the spatial profile of electron number density for the case of $\lambda_D = l_a/12$ in the x-z plane, which includes the center of the antenna. We depict white lines at the location of the dipole antenna in the figure. An electron sparse region, shown in black, is clearly found around the dipole antenna. On the other hand, ion density was confirmed to increase around the antenna due to the attraction by the negative charged antenna but less perturbed than electron density. Since charge neutrality is broken and ions become relatively rich in this region, we call it an ion sheath. In order to examine the spatial variation of the electron density in the ion sheath region in detail, the one-dimensional density distribution is shown in Figure 3.5. The density is measured along the direction perpendicular to the antenna from its surface at the midpoint of the upper antenna element. The solid and dashed lines correspond to the cases of $\lambda_D = l_a/12$ and $l_a/6$, respectively. Unlike the simplified models of the ion sheath commonly used in previous studies, the electron density varies gradually in the sheath region between 0 and 1 of the normalized distance. Note that the Debye length affects the spatial gradient of the

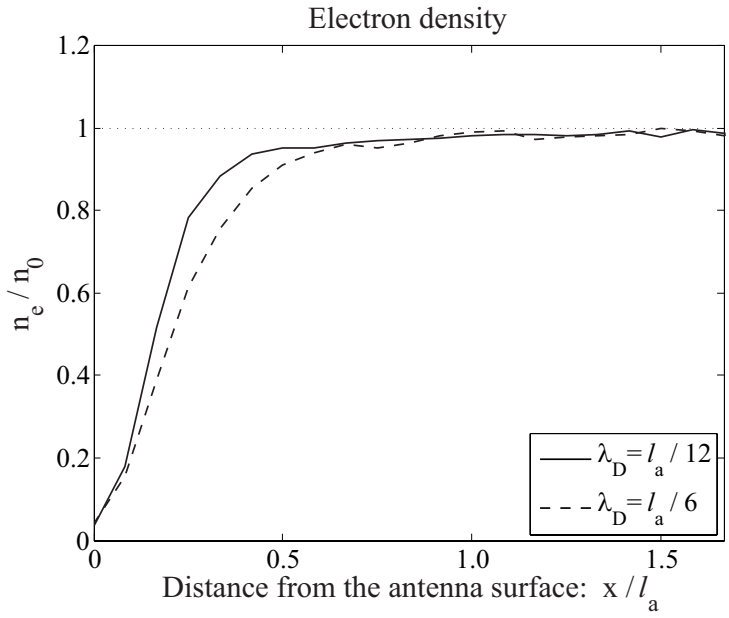

Figure 3.5: Profiles of the number density of electron measured along the direction perpendicular to the antenna from its surface (on the axis of $z = l_a/2$ shown in Figure 3.4). The solid and dashed lines correspond to the cases of $\lambda_D = l_a/12$ and $\lambda_D = l_a/6$, respectively.

electron density at the interface between the sheath and the uniform plasma. Comparing the solid and dashed lines, we find that the spatial gradient is steeper for the case of the smaller Debye length with the lower temperature.

3.4.2 Impedance of an Ion-Sheathed Antenna

The antenna impedance in the ion-sheath environment was computed by the developed tool by adopting the method described in Section 3.2. During the antenna-impedance analysis using the delta-gap feeding technique, we confirmed that the ion-sheath environment was hardly perturbed since the applied signal at the antenna feeding point was sufficiently small.

Figure 3.6 shows the sheath effects on the antenna impedance in the case of $\lambda_D = l_a/12$. The solid, dashed, and dotted lines indicate the results for the ion-sheathed, uniform plasma, and free-space cases, respectively. As in the uniform plasma case, the signature of the impedance resonance is seen around $\omega = \omega_{pe}$ for the ion-sheathed antenna. There are, however, some differences between the solid and dashed lines in the figure. As the frequency increases from the resonance frequency, i.e., $\omega \sim \omega_{pe}$, the resistance value decays to its free-space value, which is found in both the uniform plasma and the ion-sheathed cases. However, as shown in Figure 3.6(a), the resistance decays faster in the ion-sheathed

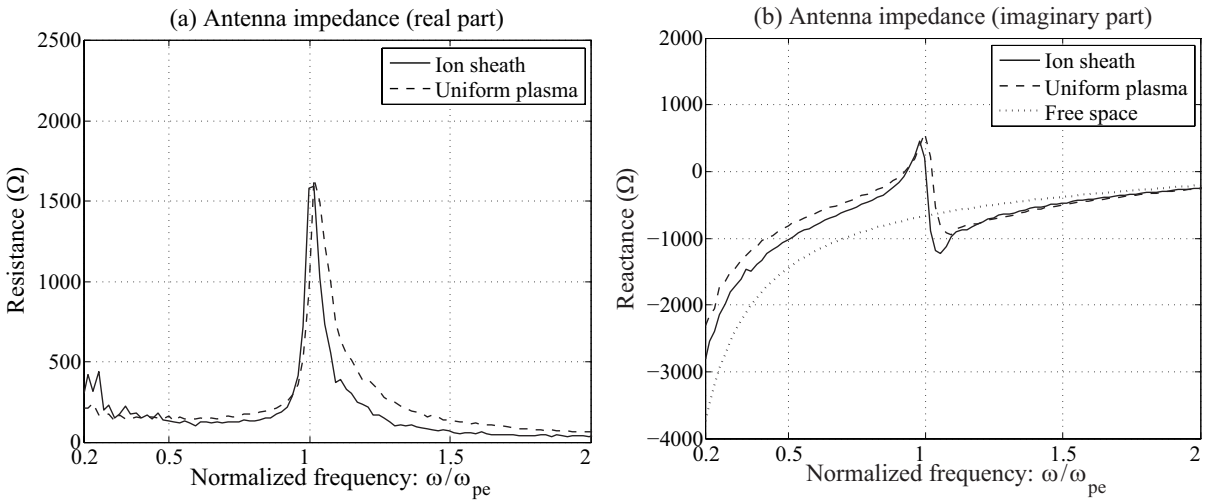

Figure 3.6: Antenna resistances (left panel) and reactances (right panel) including and not including ion sheath effects for the case of $\lambda_D = l_a/12$. The dotted line in the right panel represents the free-space reactance.

case than in the uniform plasma case.

Below $\omega = \omega_{pe}$, as shown in Figure 3.6(b), the absolute value of reactance is large for the ion-sheath environment in comparison with the uniform plasma case. In order to interpret these results, we show the results in terms of the antenna capacitance $C = -1/(\omega X)$ in Figure 3.7, in which the values are given as a product of C and ω_{pe}, so that they have the units of $1/\Omega$. As clearly shown in Figure 3.7, the capacitance C has almost a constant value in the frequency range well below $\omega = \omega_{pe}$ in all cases. Particularly, the value of C is smaller for the ion-sheath case than that of the uniform plasma case. This reduction of C is caused by the presence of the ion sheath formed around the antenna and is an important effect which has been reported in previous antenna studies [e.g., *Oya*, 1965]. Since mobile electrons are extremely scarce in the ion sheath compared to the background plasma, the ion sheath behaves as a vacuum gap that separates the antenna surface from the background plasma. Therefore, as a simple model, the ion sheath can be considered as a capacitance between two coaxial conductors. In analogy, the inner and outer conductors correspond to the antenna body and the background plasma. The reactance caused by the sheath is added to the antenna impedance and clearly affects the total capacitance value of the antenna. In other words, the capacitance of the coaxial conductors is connected to the plasma capacitance in series so that the total capacitance in the case of the ion sheath is smaller. A discussion of the relation between the sheath structure and the antenna capacitance will be presented in the next section.

It has been considered that the ion-sheath effects described above become less significant as the Debye length becomes larger in comparison with the antenna length, as mentioned in the work of e.g., *Béghin et al.* [2005]. We also examined the ion-sheath

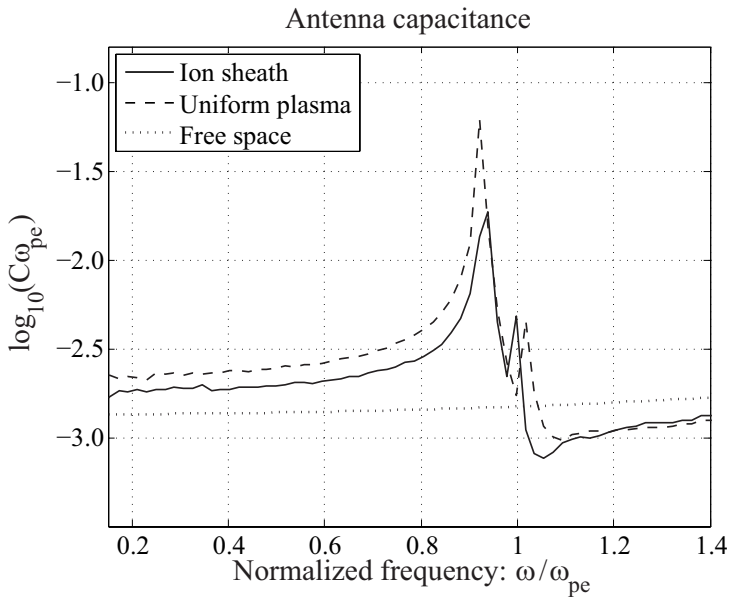

Figure 3.7: Antenna capacitance in $1/\Omega$ (see text). The solid, dashed, and dotted lines represent the antenna capacitance in an ion sheath, a uniform plasma, and free space, respectively.

effects on the antenna impedance for the case of larger Debye length $\lambda_D = l_a/6$ and confirmed that the ion-sheath effects were correctly weakened compared to $\lambda_D = l_a/12$ case. However, the fact, that the impedance modification due to the ion-sheath effects can be observed in $\lambda_D = l_a/6$ case, shows the importance of the precise modeling of an ion sheath even in situations of the Debye length in the same order of the antenna length.

3.4.3 Dependence of Antenna Impedance on the Sheath Structure

Several previous studies [*Balmain and Oksiutik*, 1969; *Aso*, 1973] formulated the impedance of ion-sheathed antennas by assuming that the total antenna impedance was represented by the impedance of the sheath plus that of the plasma connected in series. In these formulations, the impedance of the sheath region was obtained as a function of the sheath thickness. In this section, we examine the effects of the sheath thickness on the antenna impedance by performing additional simulations. For this purpose, we applied a DC bias potential to the antenna. By changing the bias potential as a simulation parameter, the sheath structure around the antenna changes, and thus we can examine various sheath environments without any changes in the background plasma parameters. In the present section, we examined two cases with different bias potentials: (a) $\phi_a = 4\phi_F$ and (b) $\phi_a = 16\phi_F$, where $\phi_F = -3.4k_BT_e/e$ is a floating potential obtained in the analysis

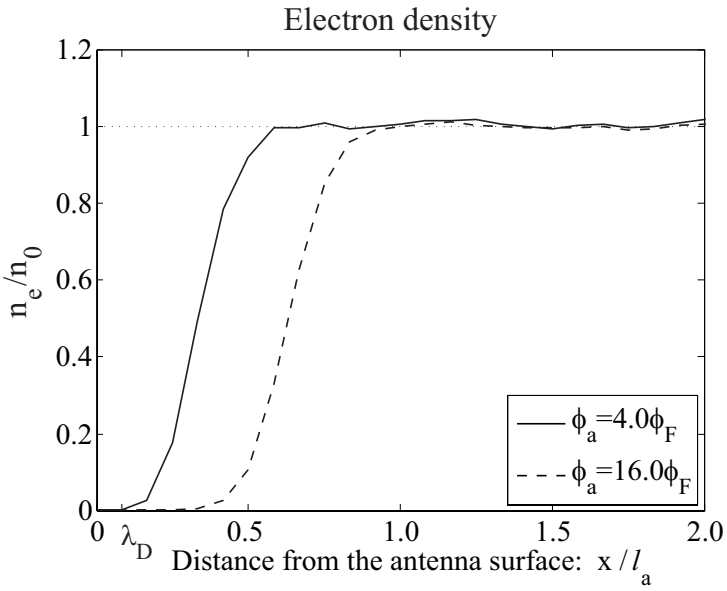

Figure 3.8: Profiles of the number density of electrons measured along the direction perpendicular to the antenna from its surface for the cases of $\phi_a = 4\phi_F$ (solid line) and $\phi_a = 16\phi_F$ (dashed line).

described in Section 3.4.1 for $\lambda_D = l_a/12$. In both cases, λ_D was fixed to $l_a/12$, and the other parameters were set as listed in Table 3.1. Note that the condition of the current balance between electrons and ions at the antenna surface is not necessary in the present analysis. In this situation, the motion of ions has little effects on the analysis. We, therefore, uniformly distributed immobile ions as a background charge in order to reduce the computational memory and time required for the analysis.

Figure 3.8 shows the electron density distribution measured along the direction perpendicular to the antenna. The solid and dashed lines correspond to the cases of (a) $\phi_a = 4\phi_F$ and (b) $\phi_a = 16\phi_F$, respectively. Ion sheaths are created for both cases, but their sizes are different. The electron-free region expands in the case (b) compared to the case (a) due to the electron evacuation by the antenna potential. Note that the spatial gradient of density at the interface between the sheath and the uniform plasma is almost the same in these two cases. In the previous section, we found that the spatial gradient of the density is affected by λ_D. In the present analysis, λ_D is common between the two cases. Therefore, it is reasonable that the thickness of the electron-free region increases for the larger antenna potential without the change in the spatial gradient of the density.

The antenna capacitance $C = -1/(\omega X)$ is shown in Figure 3.9. The signature of impedance resonance is observed in the capacitance value near $\omega = \omega_{pe}$. One can find in Figure 3.9 that the intensity of the resonance depends on the sheath thickness; it is larger for the case (a) than for the case (b). As described in Section 3.3, the impedance resonance is due to the interaction between the antenna and the plasma wave. Therefore, the

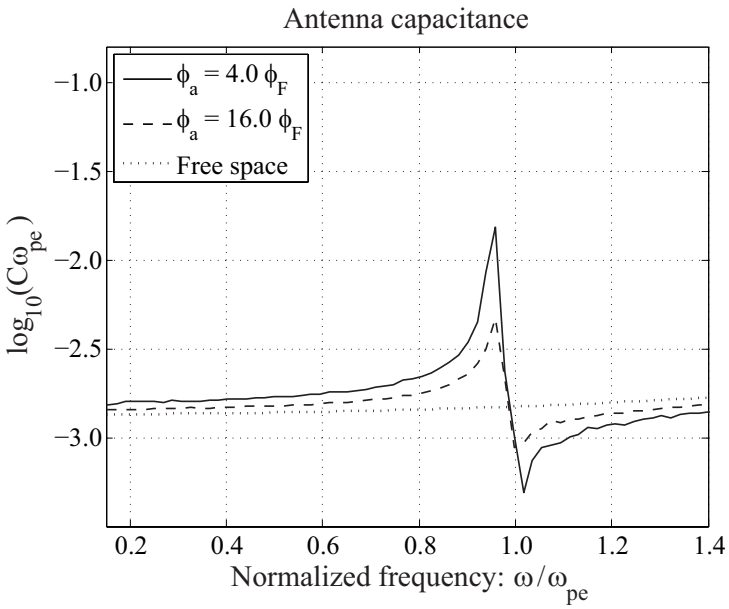

Figure 3.9: Antenna capacitance in $1/\Omega$. The solid, dashed, and dotted lines represent the capacitance in the cases of $\phi_a = 4\phi_F$, $\phi_a = 16\phi_F$, and free space, respectively.

observed dependence of the resonance intensity suggests that the thick sheath separates the antenna from the plasma and then can weaken the interaction between the antenna and the plasma wave. The sheath thickness also affects the impedance well below ω_{pe}. As shown in Figure 3.9, the capacitance curves have nearly-plateau parts. The plateau value is larger for the thin sheath and tends to approach the free-space value as the sheath expands. This can be explained by a simple analogy with the two coaxial conductors: the larger the gap between the conductors, the smaller the capacitance.

The dependence of the low-frequency capacitance on the sheath thickness as described above was reported in the previous studies [e.g., *Balmain and Oksiutik*, 1969; *Aso*, 1973]. They modeled the ion sheath which was divided into a vacuum region and a transition region in which the electron density increased linearly with respect to its ambient plasma level. The total impedance was calculated as a summation of the local impedances corresponding to each region. We confirmed that the theory basically agrees well with the present simulation outputs for the case of the thin sheath. However, as the sheath width becomes larger, the theoretical result doesn't approach to the free-space antenna impedance although the antenna capacitance should recover its free-space characteristic in the limit of wide sheath. Therefore, the theory is not applicable to the large sheath in comparison with the antenna dimensions. Furthermore, since the formulation of the local impedances was performed using the cold plasma approximation, any effects of a finite temperature on the sheath impedance cannot be treated in the theory. The present numerical method, therefore, has advantages in obtaining the complex characteristics of antenna impedance in inhomogeneous, kinetic plasma environments.

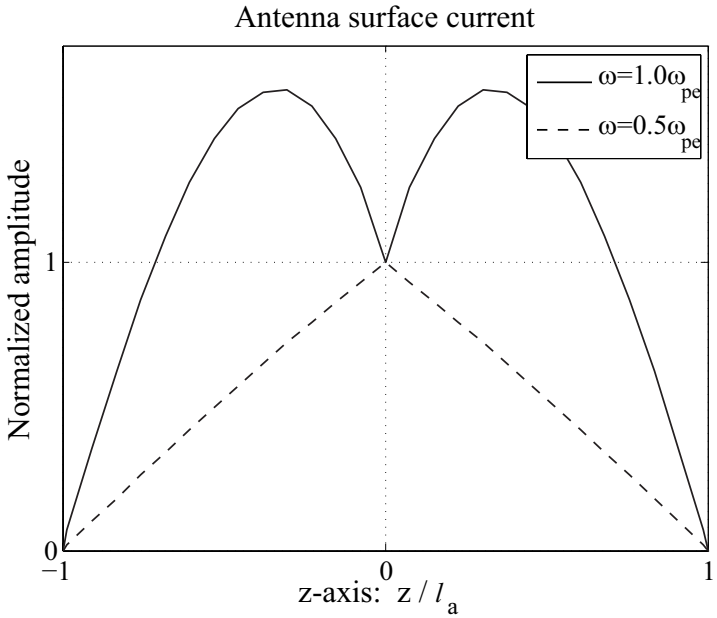

Figure 3.10: The normalized amplitude of the antenna surface current observed in the case of $\lambda_D = l_a/12$. The solid and dashed lines correspond to the observation frequencies $\omega = 1.0\omega_{pe}$ and $\omega = 0.5\omega_{pe}$, respectively.

3.5 Discussion

In Section 3.3, we presented the EM-PIC simulations of the antenna impedance in uniform plasma and compared the results with those theoretically obtained. It was confirmed that the EM-PIC simulation results overall agree with the conventional theory. However, we found that the intensity of the impedance resonance, particularly for the imaginary part, is greater in the theoretical results than those obtained in the EM-PIC simulations.

The difference found in the impedance resonance may be caused by the difference of the modeling of the current distribution on the antenna surface. In the developed EM-PIC tool, the form of the current distribution is not assumed unlike the theory but evaluated as a result of the self-consistent computation of the antenna near-field as mentioned in Section 3.2.2. Figure 3.10 shows the antenna surface current distributions observed in the EM-PIC simulation results for the case of $\lambda_D = l_a/12$. The solid and dashed lines correspond to the profiles at the observation frequencies of $\omega = 1.0\omega_{pe}$ and $\omega = 0.5\omega_{pe}$, respectively. The current distribution at $\omega = 1.0\omega_{pe}$, at which the strong impedance resonance was confirmed to occur, is clearly different from the triangular form. On the other hand, in absence of the impedance resonance, i.e., at $\omega = 0.5\omega_{pe}$, the triangular-like distribution is recovered. This implies that the strong resonance between the antenna and the surrounding plasma can affect the form of the current distribution. The non-triangular current distribution can be a possible reason for the impedance difference between the EM-PIC and theoretical results at the resonance frequency although the detailed mecha-

nism of the formation of the non-triangular current distribution has not been sufficiently resolved yet. The observed non-triangular form is very important issue since the current distribution on the antenna surface affects not only the impedance but also other important antenna characteristics such as the effective length. However, the behavior of the resonance is quite complex, and further investigation of this issue is beyond scope of the present paper. The detailed analysis on this issue will be described in another paper.

In the results of the EM-PIC simulations the resonance frequency observed for $\lambda_{\mathrm{D}} = l_{\mathrm{a}}/6$ case is shifted to higher frequency in comparison with $\lambda_{\mathrm{D}} = l_{\mathrm{a}}/12$ case. This shift may be caused by the limited size of simulation box even though we realized an isolated system. We briefly discuss this issue here. The signature of the impedance resonance is resulted from the antenna-wave interactions as described in Section 3.3. In the present plasma environment, the longitudinal plasma wave mode that can exist in the simulation system is only the Langmuir mode, of which the dispersion relation is given as $\omega^2 = \omega_{\mathrm{pe}}^2 + 3k^2v_0^2$. Therefore, the resonance signature at very near $\omega = \omega_{\mathrm{pe}}$ should reflect the contribution of the interactions between the antenna and the Langmuir wave with large wavelength. However, in the present analysis, the size of the physical region in the simulation box is limited to $48\lambda_{\mathrm{D}}$ due to the high computational cost of the EM-PIC simulation, and the plasma wave components that have wavelength larger than the size of the physical region cannot be supported in the simulation system. In addition, even for the wave components that can be supported in the system, wave components of wavelength much larger than the thickness of the absorbing layer are difficult to be completely absorbed by the absorbing layer. In this case, there is possibility that some wave components near the electron plasma frequency are reflected into the physical region from the simulation box edge. These limitations may have an influence on the EM-PIC results at the resonance frequency particularly for $\lambda_{\mathrm{D}} = l_{\mathrm{a}}/6$ case. The larger physical space in the simulation box is desirable in the future analysis to obtain the impedance value in a greater accuracy at frequencies close to the electron plasma frequency.

Another point we should pay careful attention to is that we utilized a broad spectrum pulse emission from the antenna feeding point in order to compute the antenna impedance. Feeding too large energy can cause destruction of the electron density distribution in the sheath region in equilibrium. This effect is undesirable because we focus on the antenna impedance under the steady state of the sheath environment in the present study. We confirmed that the sheath structure obtained as the steady state of the plasma environment was not corrupted by the pulse emission. This is because the electric energy of the applied signal was set to $0.11\,E_{\mathrm{sh}}$, where E_{sh} is calculated as an integral of the electrostatic energy in the sheath region, and was sufficiently small. We also checked several simulation results as a simple test by changing the amplitude of the applied signal and confirmed that almost the same results of impedance value were obtained in all cases

except near the impedance-resonance frequency. Even near the resonance frequency, the difference of the impedance value was less than 3 % when we doubled the signal amplitude. This implies the linear voltage-current characteristic is overall maintained in the wide frequency range. For the detailed analyses at the resonance frequency, this effect should be minimized by using a pulse with smaller amplitude in future studies.

In the present section, we presented several key points of the EM-PIC simulation tool that should be carefully considered to improve the present state of the accuracy of the impedance analysis. However, the limitations described in the present section can be basically resolved by using larger computational resources. The larger memory enables us to take a larger size of the simulation box. The amplitude of the emitted broad spectrum signal can also be reduced by introducing a larger number of the superparticles. This is because a numerical noise, which is originated from the smaller number of macro-particles used in the simulation than that of real electrons, can be reduced, and thus a better signal-noise ratio can be realized by increasing the number of the superparticles. We believe that by performing large-scale computations, we can minimize the artificial effects on the EM-PIC results and analyze the antenna characteristics in a greater accuracy.

3.6 Conclusion

In order to investigate the antenna characteristics including the plasma kinetic effects in a self-consistent manner, we have applied the EMSES code to the antenna analysis. In the present study, we focused on the impedance of a low-power transmitting antenna because this basic property is useful for the validation of the EMSES application to the analysis. EMSES was first validated by examining the wire-antenna characteristics in a homogeneous kinetic plasma. The obtained antenna impedance showed good agreement with the analytic results based on the conventional theory at frequencies below and above the electron plasma frequency. Near the electron plasma frequency, the dependence of the impedance-resonance intensity on the plasma temperature was qualitatively consistent with that expected analytically, although the peak values of the impedance resonance showed a discrepancy between the EM-PIC and theoretical results.

The present tool was next applied to the analyses of the ion sheath effects on the antenna impedance. Since the sheath dynamics were simultaneously solved during the analyses, the effects on the antenna impedance was included in a more self-consistent manner than the previous works that assumed simplified structure of the ion sheath. As was predicted by the previous theories, the low-frequency capacitance was confirmed to be decreased by the presence of the ion sheath. The signature of the impedance resonance is also modified by the ion sheath. Particularly, it was revealed that the resonance is weakened when one applies a negative large bias potential, which leads to a thick ion

sheath around the antenna. To understand the more detailed physical mechanism of the present results, further analyses of the energy distribution of electrons and the wave propagation properties in the sheath region are required. The PIC simulation method is effective for such detailed diagnosis [*Usui et al.*, 2004]. The larger scale analyses will enable us to investigate the physical properties of the ion sheath in greater detail in the future.

By examining the antenna impedance in the simple situations with and without the ion-sheath effects, we successfully demonstrated the present state of the validity and the effectiveness of EMSES. On the other hand, the present test revealed some limitations of the developed tool, which showed several important factors that we should improve in further development of the tool. Although the proposed approach is costly in the respect that it requires large computational resources and time, we believe that realistic and practical modeling is effective for obtaining the complex antenna characteristics in plasmas as well as for evaluating the validity of other low-cost methods.

Chapter 4

Analysis of Photoelectron Effect on the Antenna Impedance

4.1 Introduction

The photoelectron emission resulting from the sunlight illumination of conducting antenna/spacecraft surfaces much influences the characteristics of a space-based antenna immersed in a tenuous plasma. Since photoelectrons play a critical role also in determining spacecraft potential, their number and current densities have been extensively investigated by laboratory measurements [*Grard*, 1973] and in-flight measurements with various spacecraft such as GEOS-1, ISEE-1, GEOS-2, and GEOTAIL [*Pedersen et al.*, 1984; *Schmidt and Pedersen*, 1987; *Nakagawa et al.*, 2000]. Their typical density is in the order of $10^2 - 10^3\,\mathrm{cc}^{-1}$ and easily dominates over that of background plasma electrons at almost all regions outside the plasmapause of the Earth. Thus, photoelectrons become a problematic issue in various situations of electric field measurements.

Investigations of photoelectron effects have been carried out mostly for measurements of quasi-static electric field [*Pedersen et al.*, 1984]. The electric potential of an electric antenna or a double probe is determined by a balance condition between currents carried by escaping photoelectrons and impinging background electrons. Therefore, an asymmetric condition of the photoemission between two antenna elements immediately leads to generation of spurious or noise electric fields, which are serious sources of measurement errors. Hence, a special attention has been paid to achieve the symmetric fashion of the photoemission from an early history of the DC electric field instrument design [*Pedersen et al.*, 1998]. Meanwhile, photoelectrons also provide a favorable and necessary condition for the probe measurements of the static electric field in tenuous magnetospheric plasmas. In order to conduct reliable measurements minimizing effects of spurious currents (e.g., from probe supports), a probe and a surrounding plasma are well coupled with sufficiently lower magnitude of impedance than that of an input impedance. This comfortable coupling can be achieved only by the photoemission in the tenuous plasma environment [e.g.,

Pedersen et al., 1984]. In this manner, because the photoelectron emission is an essential factor as well as being a troubling factor, utmost care has been taken for the photoelectron effects in the static electric field measurements.

In contrast with the presence of several helpful lessons for measurements of static electric field as mentioned above, photoelectron effects on the frequency response of electric antenna characteristics, e.g., the impedance, have been poorly resolved in the current status. As introduced in Chapter 1, the previous theories of the antenna impedance have in most cases treated only homogeneous plasmas, or ion-sheathed plasma environment with an assumption of its highly simplified structure. A cloud of photoelectrons often have much more complex structure than that of an ion sheath. The complexity comes from the fact that photoelectrons are emitted only from sunlit conducting surfaces, and the photoelectron flux depends strongly on the incident angle of the sunlight. Also, the orbits of the photoelectrons, which have relatively low energy ($\sim$eV), are easily changed due to antenna/spacecraft charging. The resulting complex distribution of photoelectrons is too difficult to treat in the previous antenna theories.

Another limitation of the previous theories comes from the modeling of antenna surfaces. It is expected that a photoelectron current flowing out/into the antenna surfaces affects not only static but also RF properties of antennas in some situations. To include the contribution of such a current, the antenna surfaces should be treated as solid surfaces. However, in the previous works, the antenna is assumed to be a thin conductive wire that is completely transparent to the fluid plasma medium, and the contribution of the currents directly flowing out/into the surface cannot be considered self-consistently, as introduced in Section 3.2.2. This limitation is serious particularly in the antenna analysis in the photoelectron environment compared with an ion-sheathed environment, because high-density electrons contact with antenna surfaces in the photoelectron environment while much smaller amount of electrons contact in the ion-sheathed environment.

On the other hand, some of in-flight impedance measurement results have shown clear signatures apparently influenced by the presence of photoelectrons. One of the most prominent data was a spin-synchronized impedance change obtained for the WANT element onboard the GEOTAIL spacecraft [*Tsutsui et al.*, 1997]. Because a photoelectron flux from the wire antenna strongly depends on the angle between the antenna and the sunlight direction, it is expected that the amount of photoelectrons around the antenna is also synchronized with the spacecraft spin. Therefore, the spin-synchronized impedance change strongly suggests that the impedance depends on the photoelectron amount around the antenna.

In order to prove such a photoelectron effect, we should perform computer experiments, which reproduce complex photoelectron environment created around the spacecraft. In this chapter, we concentrate on investigations of the frequency responses of space-based

antenna impedance in the presence of photoelectrons [*Miyake and Usui*, 2008b]. We focus on a tenuous and warm plasma environment typically observed in the outer magnetosphere of the Earth. The terms "tenuous and warm" indicate in this context that the Debye length is comparable to or larger than the antenna length. We model the photoelectron emission from the antenna surface and investigate its effects on the antenna impedance. We also include the geometry of the spacecraft body in the simulation model. In future missions currently being planned by the Japanese community of solar terrestrial physics, spin-axial electric field antennas are planned to be implemented to realize three-dimensional measurements of electric field. In order to retain attitude stability and low weight, the spin-axial antennas must be sufficiently shorter than the conventional wire antenna. The characteristics of such a short antenna must be investigated by considering spacecraft body effects prior to its design.

In Section 4.2, we describe simulation model and parameters used in the present analysis. We also explain the modeling of photoelectrons briefly. In Section 4.3, we present simulation results obtained by the present antenna analysis. We first survey a plasma environment around the spacecraft in the presence of the photoelectron emission. We then focus on a photoelectron effect on the antenna impedance. Section 4.4 is devoted to the interpretation of the obtained simulation results by introducing an equivalent electric circuit model. Finally, in Section 4.5, we discuss the contribution of the present simulation results to the interpretation of in-flight impedance measurement data obtained by the GEOTAIL spacecraft.

4.2 Simulation Model

The model of the present antenna analysis is shown in Figure 4.1. The present analysis focuses on the characteristics of antennas deployed along the spin axis of a spacecraft. Although such an antenna has been rarely aboard previous scientific spacecraft due to difficulties in attitude stability and deployment mechanics, it will become necessary for three-dimensional measurements of electric fields in future magnetospheric exploration projects such as the SCOPE (Scale COupling in the Plasma universE) mission [*Schwartz et al.*, 2008]. As shown in Figure 4.1, the spacecraft body has the shape of an octagonal plate that is described within the regular Cartesian grid system. Two antenna branches are deployed from opposite sides of the spacecraft surfaces. The antenna branches are represented as thin wires, the cross-sections of which are $\Delta r \times \Delta r$ square, where Δr represents the grid spacing and is the minimum spatial unit length in the simulations. Therefore, the surface area exposed to a surrounding plasma is given as $S = 4l_{\mathrm{a}}\Delta r + \Delta r^2 = 49$ for each antenna branch, where l_{a} represents the length of one antenna branch (different from the tip-to-tip length L_{a}). For simplicity, all surfaces of the antenna branches and the

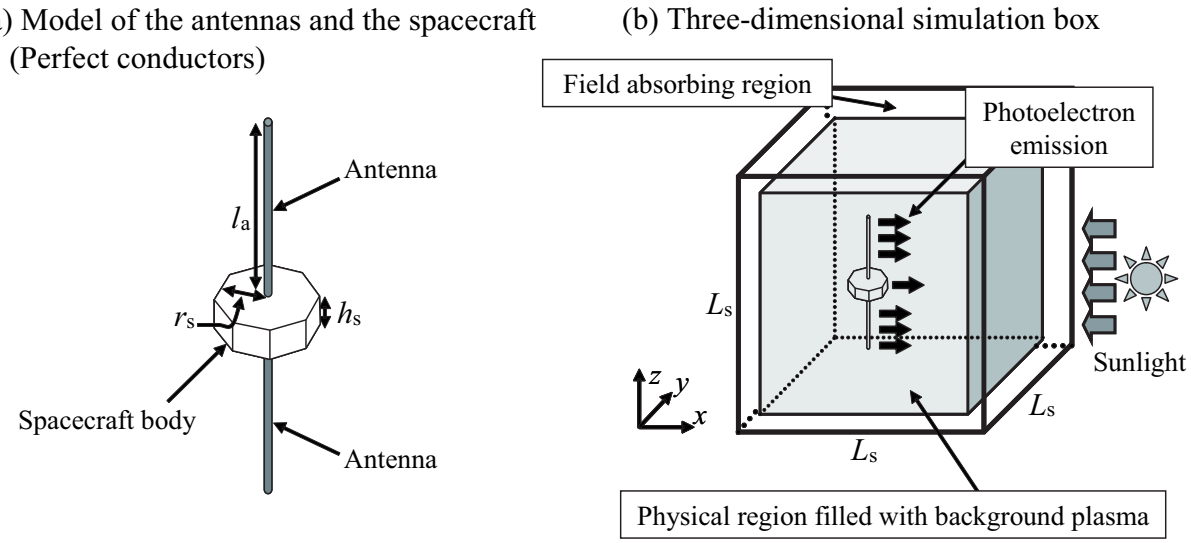

Figure 4.1: Three-dimensional simulation model for the antenna analysis in a photoelectron environment.

spacecraft are assumed to be constructed of perfect conductors. The perfect conducting assumption does not describe a real situation precisely. Antennas are often coated with thin dielectric materials. However, the effect of this coating on the antenna characteristics can be neglected because only the conductive parts of the deployed branches should work as an electrical antenna. The antennas are connected to the amplifier through very high impedance in actual situations. Taking this into consideration, in the present model, we assume the joints between the antennas and spacecraft to be completely insulated electrically.

We place the spacecraft model in the center of a three-dimensional simulation box, which is uniformly filled with background plasmas composed of electrons and protons with finite thermal velocity. The box size is set to $\sim 11\lambda_D$ on each side, where λ_D represents the Debye length. The boundary conditions for outer edges of the simulation box are basically identical to those used in the previous chapter, which is selected so as to realize an isolated system. As shown in Figure 4.1, we set an absorbing boundary layer consisting of 20 grids from the edges of the box. We use the Neumann condition in solving Poisson's equation. Particles escaping from the outer boundaries are reflected.

The parameters for the background plasmas and the photoelectrons are listed in Table 4.1, which is given in the normalized unit system used in the simulation code. In the present analysis, we choose the parameters considering an electric field antenna that is placed in the outer magnetosphere such as the magnetosheath. As shown in Table 4.1, we use the real mass ratio $m_i/m_e = 1836$, where m_i and m_e represent the mass of electrons and protons, respectively. The background plasma parameters are chosen such that they

Table 4.1: Simulation parameters for the analysis of antenna impedance in a photoelectron environment. The values are given in the normalized unit system used in the EMSES code. e represents the electron unit charge.

Parameter	Symbol	Value
System		
Grid spacing	Δr	1
Time step width	Δt	0.005
Speed of light	c	100
System length	$L_{\rm s}$	128
Electron charge-to-mass ratio	$\lvert e/m_{\rm e}\rvert$	1
Number of superparticles (electron)		64/cell
Number of superparticles (ion)		32/cell
Background plasma		
Electron plasma frequency	$\omega_{\rm pe}$	1
Ion plasma frequency	$\omega_{\rm pi}$	0.023
Mass ratio	$m_{\rm i}/m_{\rm e}$	1836
Electron thermal velocity	$v_{\rm te}$	12
Ion thermal velocity	$v_{\rm ti}$	0.28
Debye length	$\lambda_{\rm D}$	$\sim$12
Electron differential flux	$\Gamma_{\rm e}$	$e\Gamma_{\rm e}\sim$4.8
Photoelectron		
Current density	$e\Gamma_{\rm ph}$	$\sim 2.4\times10^{2}$ (case a) $\sim 6.0\times10^{1}$ (case b)
Thermal velocity	$v_{\rm tp}$	6
S/C body and antennas		
Length of one antenna branch	$l_{\rm a}$	12
Frequency at which the antenna operates as the half-wave dipole	$\omega_{\rm half}$	$\sim$13
Antenna surface area	S	49
Photoemitting antenna surface area	$S_{\rm ph}$	12
S/C dimensions (see Figure 4.1)	$h_{\rm s}$	2
	$r_{\rm s}$	2

yield a quasi-neutral plasma. We also assume that the background plasma is isothermal. Also in the present chapter, our interest is on the characteristics of "an electrically short antenna" near the electron plasma frequency $\omega_{\rm pe}$. To realize the electrically short antenna, we set $\omega_{\rm half}\sim 13\omega_{\rm pe}$, where $\omega_{\rm half}$ represents the frequency at which the antenna operates as a half-wavelength dipole. An important difference from the previous chapter is the parameter setting for a ratio between $l_{\rm a}$ and $\lambda_{\rm D}$. In the previous chapter, we examined a dipole antenna with sufficiently larger antenna length than the Debye length. However, actually in the outer magnetosphere, $\lambda_{\rm D}$ typically becomes comparable to or larger than $l_{\rm a}$. In the present analysis, we choose the background plasma parameters such that $\lambda_{\rm D}$ is equal to $l_{\rm a}$.

On the other hand, we choose the photoelectron differential flux as $\Gamma_{\rm ph} = 50\Gamma_{\rm e}$, where $\Gamma_{\rm e}$ is the differential flux of background plasma electrons. The energy is set to be a quarter of that of the background electrons. By choosing the above photoelectron parameters, we expect that the local photoelectron density becomes of the order of 10^1–$10^2 n_0$, where n_0 represents the background electron density, and the Debye length obtained from the photoelectron density becomes much shorter than $l_{\rm a}$. This relation between the Debye length for photoelectrons and $l_{\rm a}$ is the case in the outer magnetosphere of the Earth.

In the simulation, we select conductive surfaces illuminated by sunlight as inner boundaries from which photoelectrons are assumed to be emitted. Then, we inject electrons from the inner boundaries corresponding to the sunlit surfaces, which simulates the photoelectron emission. For the particle injection, we used a conventional scheme described in e.g., *Birdsall and Langdon* [1985]. For simplicity, the velocity distribution for the photoelectrons is modeled as a single Maxwellian. In the present study, we assume that the sun illuminates the spacecraft body and the antennas from the direction perpendicular to the antennas, i.e., from the $+x$ direction in Figure 4.1. We also examine the plasma environment in the absence of the photoelectron emission, for comparison.

In the analysis of the plasma environment around the antenna, we initially distribute background plasmas uniformly throughout the simulation box. Then, we start a simulation with electron emission from the sunlit surfaces of the antenna and the spacecraft. In order to obtain the static environment, we run the simulation with sufficient time steps prior to the antenna analysis, until the plasma density around the spacecraft as well as the electric potential of the antenna and the spacecraft reaches a steady state.

After obtaining the steady state of the plasma environment, we switch to analysis of the antenna impedance. We simulate a transmitting antenna with low power by adopting the delta-gap feeding technique as was conducted in Chapter 3. Figure 4.2 shows the field assignment in the vicinity of the gap between the upper antenna and the spacecraft body. The method for the calculation of antenna impedance is basically the same as explained in Section 3.2.2, i.e., $Z(\omega) = V_{\rm in}(\omega)/I_{\rm in}(\omega)$, where the assignment of voltage $V_{\rm in}$ and current $I_{\rm in}$ is indicated in Figure 4.2. The present antenna model has two feeding points between the spacecraft body and the upper/lower branches of the antenna. Therefore, the voltages and currents defined at the two feeding points are independently obtained as simulation outputs. Then, we independently analyze the impedance for each of the two antenna branches. In the present analysis, since we only treat symmetric photoelectron environment, the upper and lower antennas should have the same impedance. Hereinafter, all results of antenna impedance are obtained for the upper antenna.

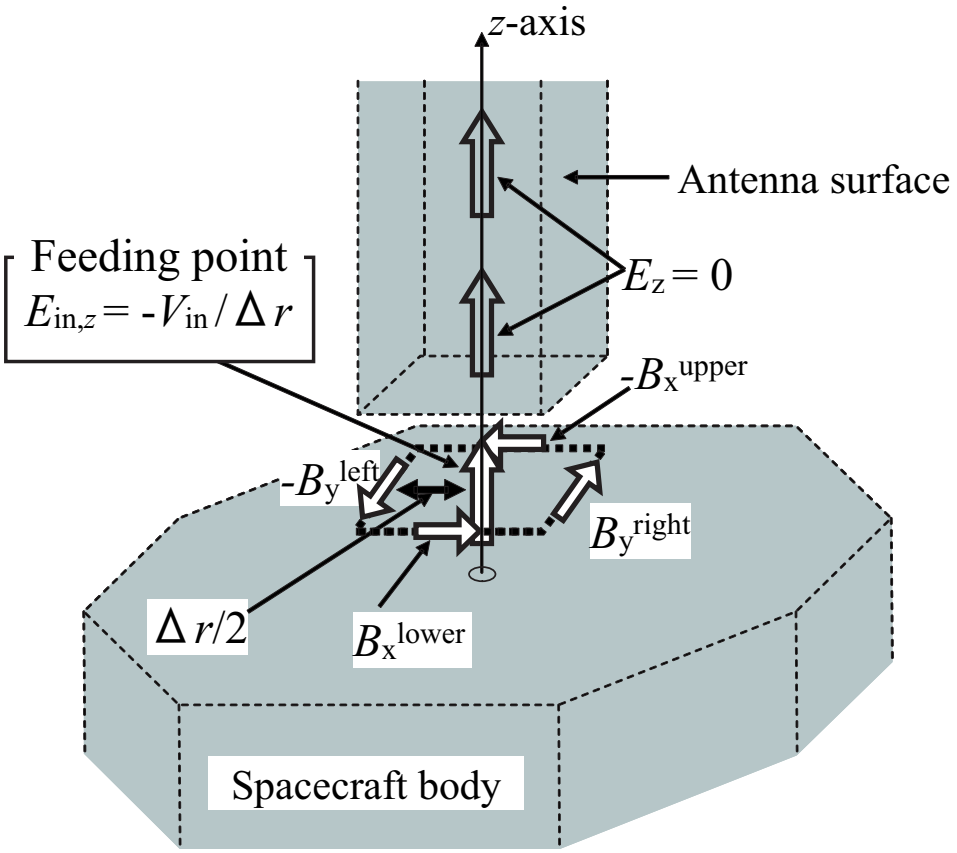

Figure 4.2: Field assignment in the vicinity of the antenna feeding point. In the antenna analysis, we feed the input voltage $V_{in} = -E_{in,z}\Delta r$ at the feeding point. Then, we observe the current I_{in} at the feeding point, which is calculated by using the magnetic field components, namely, B_x^{lower}, B_y^{right}, B_x^{upper}, and B_y^{left}.

4.3 Simulation Results

4.3.1 Spacecraft Environment with Photoelectron Emission

Figure 4.3 shows a time history of the current magnitude I_e and I_{ph} for background electrons and photoelectrons that impinge on and escape from the antenna surfaces, respectively. At an initial state of the simulation, I_{ph} is much greater than I_e, which leads to positive charging of the antenna. Then, the positive potential of the antenna reduces I_{ph}. Because the background ion current I_i is negligibly small in comparison with that of electrons, the steady state of the antenna floating potential is realized when I_{ph} and I_e balance. As shown in Figure 4.3, the magnitude of the currents at the steady state is $I_{ph} = I_e \sim 1.7I_{e0}$. Here, I_{e0} is the background electron current at an initial state when the antenna potential is equal to that of the background plasma, and is given as $Se\Gamma_e$ where e is the electron unit charge. In a case of no photoelectrons, I_e and I_i should balance to form a steady state. Although not displayed, it is confirmed that the current magnitude

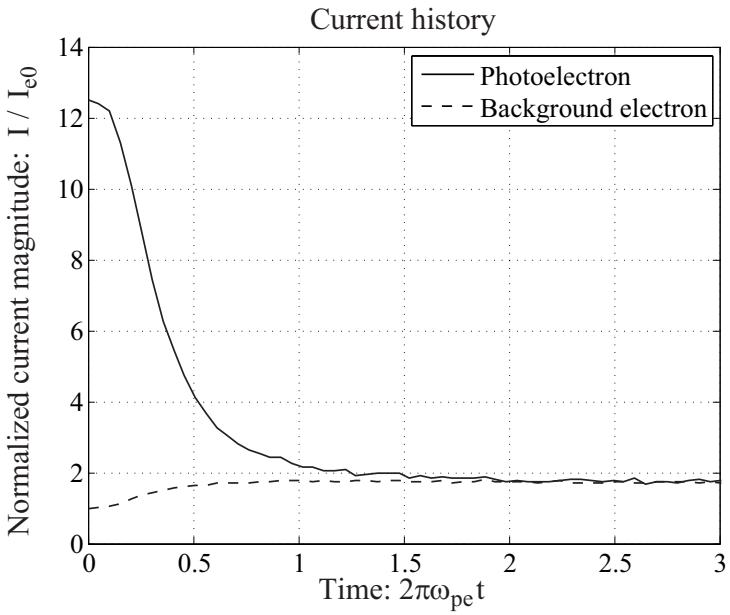

Figure 4.3: Time histories of photo- and background electron currents flowing out of and into the antenna surfaces, respectively. The vertical axis is normalized to $I_{e0} = Se\Gamma_e$, which is the background electron current flowing into the surfaces when the antenna potential is equal to that of the background plasma.

at the steady state is $I_e = I_i \sim 7.0 \times 10^{-2} I_{e0}$.

Figure 4.4 shows the electric potential distribution at the steady state of the simulations along an axis that penetrates the center of the spacecraft body and the antenna. For the case of no photoelectrons, floating potentials $-2.5k_BT_e/e$ and $-3.5k_BT_e/e$ are obtained for the spacecraft and the antenna bodies, respectively. Here, k_B and T_e are the Boltzmann's constant and the background electron temperature, respectively. The resultant potential for the spacecraft agrees well with the theoretical value $-2.5k_BT_e/e$ for a spherical conductor whose dimension is significantly smaller than λ_D [*Mott-Smith and Langmuir*, 1926; *Fahleson*, 1967].

For the case with photoelectrons, the floating potentials for the spacecraft and the antenna bodies are $3.2k_BT_{ph}/e$ and $6.4k_BT_{ph}/e$ (i.e., $0.8k_BT_e/e$ and $1.6k_BT_e/e$), respectively, where T_{ph} represents the photoelectron temperature. We successfully reproduced the positive charging in the case with photoelectrons. Using the conventional theory [*Schmidt and Pedersen*, 1987], we can analytically calculate the magnitude of the potential as $2.0k_BT_{ph}/e$ for the spacecraft body. Although in the theory we considered a considerably simplified situation in which only a single conductor emits photoelectrons in the plasma unlike the actual simulation model, the resultant potential of the spacecraft is in the same order as that of the theoretical potential. Therefore, it is confirmed that the present numerical results are basically consistent with the plasma theories.

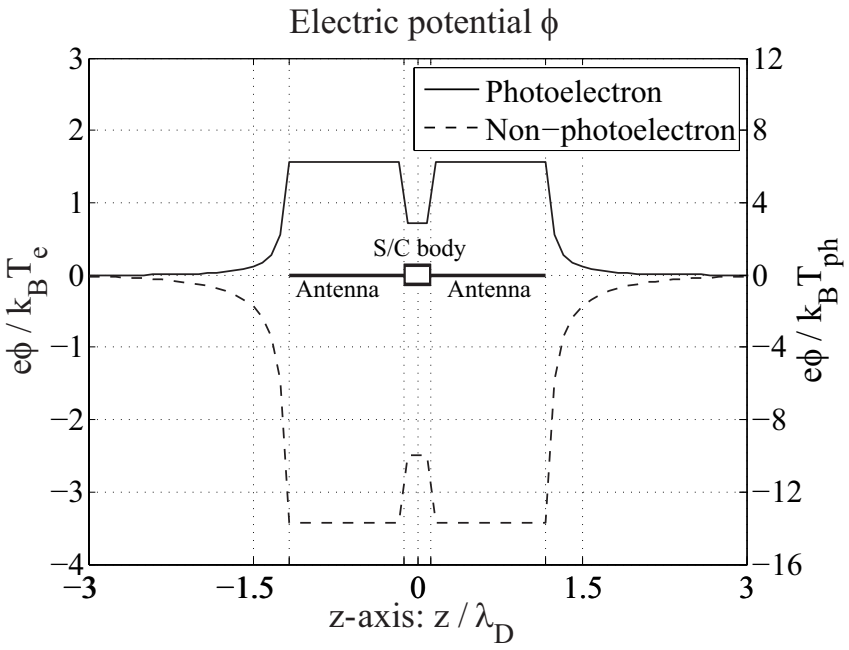

Figure 4.4: Spatial profile of the electric potential measured along the z-axis that lies on the antenna surfaces and penetrates the center of the spacecraft body. The solid and dashed lines represent the photoelectron and non-photoelectron cases, respectively. The left and right vertical axes are normalized using the background electron temperature T_{e} and the photoelectron temperature T_{ph}, respectively.

Figure 4.5 shows contour plots of the electron number density in cases with and without photoelectron emission at the steady state. The electron density is measured in the x-z plane, which slices the center of the antennas and the spacecraft. The electron density level is plotted in accordance with the gray scale in these figures, with the highest value in white and the lowest value in black. Note that the sunlight illuminates the right-hand side of the antennas and the spacecraft in Figure 4.5(b).

In the non-photoelectron case, an electron-sparse region surrounds the spacecraft body and the antennas, as shown in Figure 4.5(a). Recalling that the spacecraft and the antennas have negative potential in the absence of photoelectrons, this electron-sparse region is easily understood because the negatively charged surfaces repel the surrounding electrons. In contrast, although not displayed, we confirmed that the ion density changes only slightly from the background density level, except for a region very close to the conducting surfaces. Thus, an ion-rich region, referred to as an ion sheath, is created around the spacecraft and the antennas in the sunless condition. On the other hand, in Figure 4.5(b), the plasma environment is changed drastically by the photoelectron emission. In this case, a photoelectron cloud with high electron density is created in the vicinity of the sunlit surfaces of the antennas and the spacecraft body. Although most of the emitted photoelectrons are located in front of the sunlit side of the surfaces, some

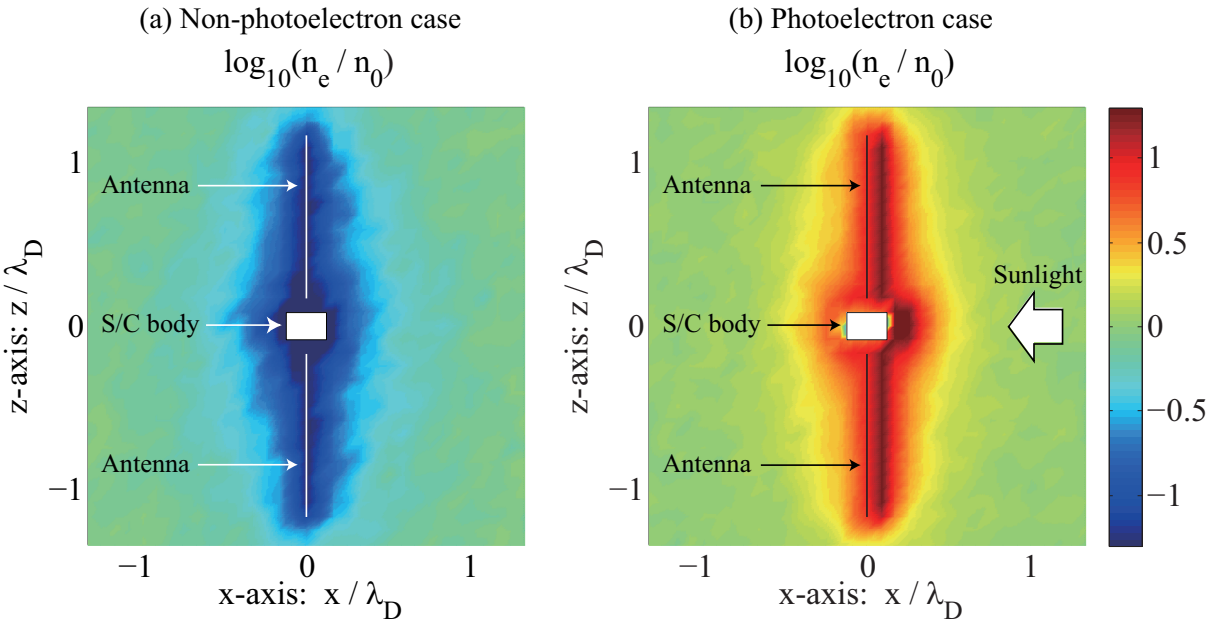

Figure 4.5: Contour map of the electron density around the spacecraft and the antenna. The left and right panels represent the cases without and with the photoelectron emission, respectively. In the right panel, we assumed the sunlight illuminates the antennas and the spacecraft from the right direction.

of the emitted photoelectrons move to the shadowed side and create an electron-dense region there.

In order to examine the plasma distribution at the conducting surfaces, we plot the electron density along the antenna direction in Figure 4.6. The density is measured along the z-axis, which lies on the antenna surfaces and penetrates the spacecraft body. We confirmed that the electron density is reduced to 0.03–0.1 times the background density n_0 at the antenna in the non-photoelectron case. On the other hand, in the photoelectron case, the photoelectron cloud is distributed uniformly on the antenna locations. Around the sunlit antennas, the electron density is $17n_0$. Although the photoelectron cloud on the spacecraft surfaces is not displayed in Figure 4.6, we confirmed the same order of the electron density as for the antenna surfaces.

4.3.2 Photoelectron Effects on the Antenna Impedance

After the steady-state of the inhomogeneous plasma environments was created, we computed the antenna impedance for each of the cases with and without the photoelectron emission.

Prior to analysis of the numerical simulation results, we briefly describe a basic characteristic of the antenna impedance in free space. As is widely known, the real part of the impedance R represents dissipation, which is typically caused by radiation because the

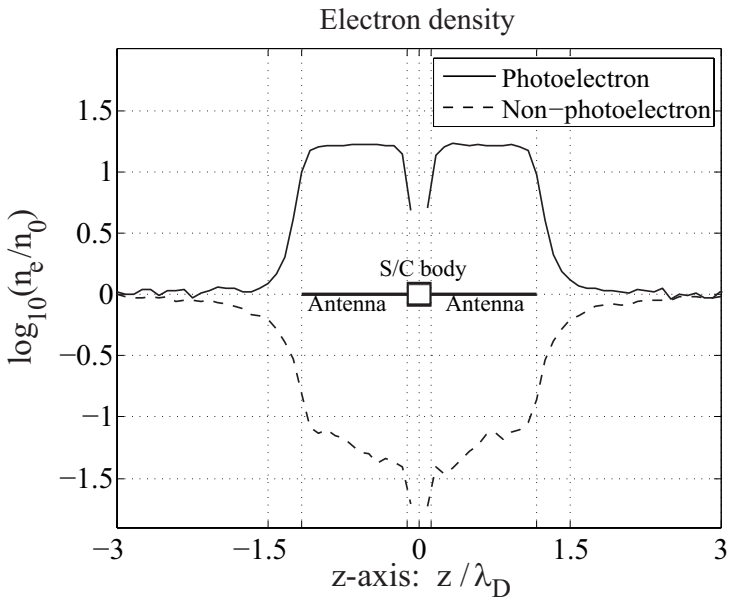

Figure 4.6: Electron density variation measured along the z-axis, which lies along the antenna surface and penetrates the center of the spacecraft body. The solid and dashed lines represent the photoelectron and non-photoelectron cases, respectively.

radiated power leaves the antenna and never returns. In the case of electrically short antenna, R is approximately zero because the EM-wave radiation is negligible. On the other hand, the imaginary part of the impedance X represents the reactive power stored in the vicinity of the antenna. For an electrically short dipole antenna, X is known to be purely capacitive, i.e., $X = -1/\omega C_0$, where C_0 represents the free-space antenna capacitance.

Figure 4.7 shows the real part (left panel) and the imaginary part (right panel) of antenna impedance obtained in the plasma environment with or without photoelectron emission. The horizontal axis is normalized to the electron plasma frequency $\omega_{\rm pe}$ for the background plasma. The local electron plasma frequency $\omega_{\rm sf} \sim 4.1\omega_{\rm pe}$ is also shown in the figure, which is calculated from the local electron density at the antenna surface for the case with photoelectrons. The solid and dashed lines in the figure represent the antenna impedance for the cases with and without photoelectron emission, respectively. We also plot the free-space reactance by a series of circles in the right panel of Figure 4.7, which was calculated by independently performing a FDTD simulation for a free-space case.

In the case of no photoelectrons (dashed lines), the antenna resistance R is almost null with a slight variation within the noise level caused by the limited number of particles used in the simulations. The reactive power X is always negative, which indicates that the antenna is capacitive. Furthermore, we confirmed that the observed curve of X is identical to the free-space reactance $X = -1/\omega C_0$. The above fact implies that the background plasma has little effect on the antenna impedance in the absence of the

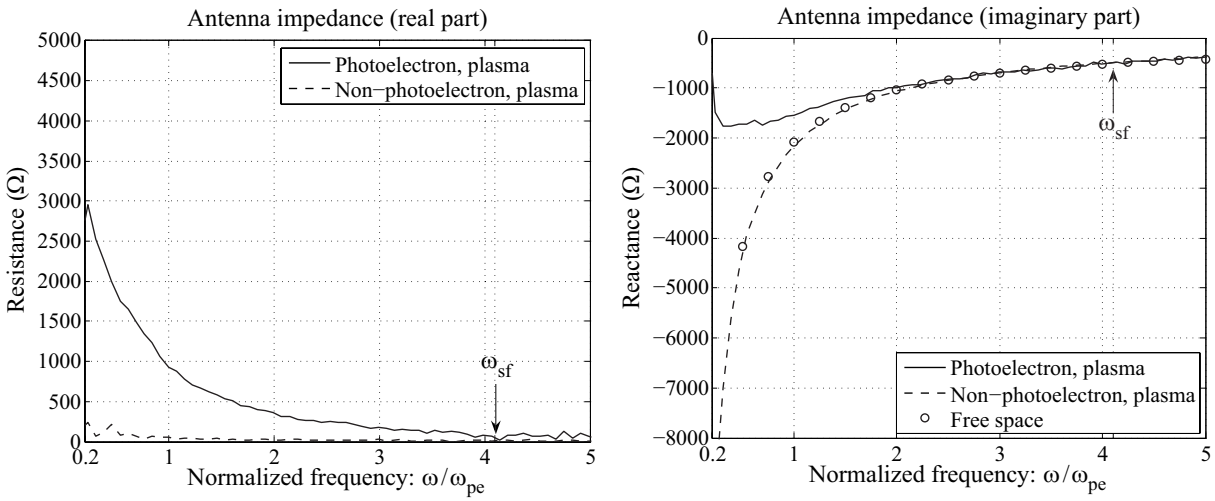

Figure 4.7: Antenna resistances $R(\omega)$ (left panel) and reactances $X(\omega)$ (right panel) as functions of the frequency obtained by the EM-PIC simulations. The solid and dashed lines represent the photoelectron and non-photoelectron cases, respectively. A series of circles in the right panel shows the free-space reactance values.

photoelectron emission. The impedance resonance, which usually occurs near the electron plasma frequency, is too weak to observe for small l_a/λ_D employed in the present analysis.

In the presence of photoelectrons, the impedance behavior is quite different from the case without photoelectrons. In the low-frequency range well below $\omega = \omega_{sf}$, R has a finite value and becomes greater as the frequency decreases. The absolute value of X becomes smaller in comparison with the non-photoelectron case at the low-frequency range. The notable feature is that the difference from the non-photoelectron case becomes greater as the frequency approaches zero. In contrast, the impedance shows little difference from the non-photoelectron case in the frequency range above $\omega = \omega_{sf}$. Note that the signature of the impedance resonance is not seen near $\omega = \omega_{pe}$ or $\omega = \omega_{sf} \sim 4.1\omega_{pe}$.

In order to examine the dependence of impedance on the amount of photoelectrons, we performed a simulation for the photoelectron flux $\Gamma_{ph} = 12.5\Gamma_e$ in addition to the case $\Gamma_{ph} = 50\Gamma_e$. In the case of $\Gamma_{ph} = 12.5\Gamma_e$, the electron density at the sunlit surfaces was confirmed to become 0.32 times the value in the previous case $\Gamma_{ph} = 50\Gamma_e$. Figure 4.8 shows the antenna impedance for the cases (a) $\Gamma_{ph} = 50\Gamma_e$ and (b) $\Gamma_{ph} = 12.5\Gamma_e$. The solid and dashed lines correspond to cases (a) and (b), respectively. The modification of the reactance X is moderated in case (b) in comparison with case (a). This moderation is easily expected from the smaller amount of photoelectrons in case (b), as compared to case (a). However, for the resistance R, more complex dependence on the photoelectron density is observed. The resistance for case (b) is smaller than the value for case (a) above $\omega \sim 0.4\omega_{pe}$. However, the resistance for case (b) exceeds that in case (a) below $\omega \sim 0.4\omega_{pe}$.

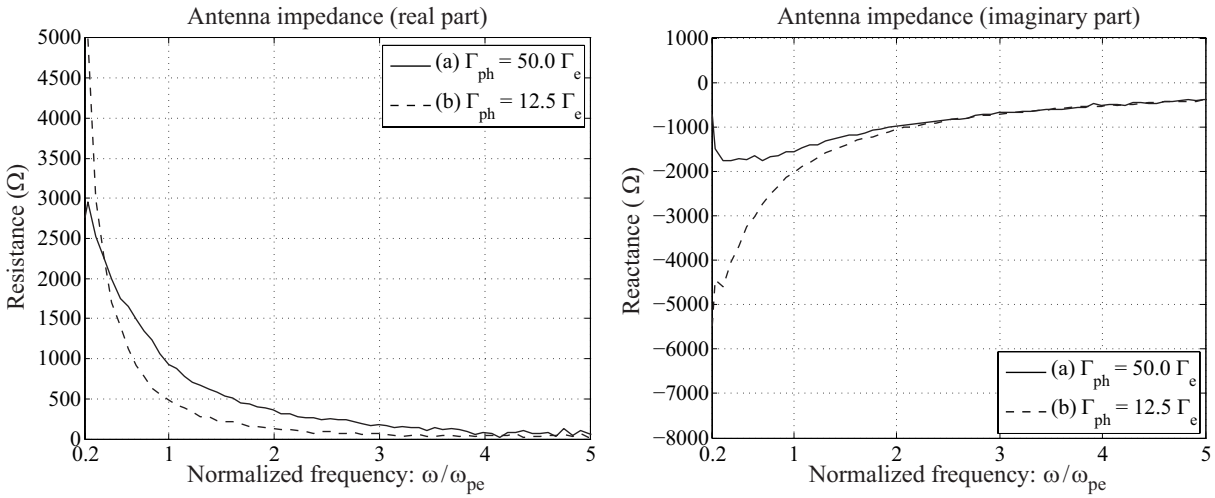

Figure 4.8: Antenna resistances $R(\omega)$ (left panel) and reactances $X(\omega)$ (right panel) obtained by the EM-PIC simulations for the cases of $\Gamma_{\rm ph} = 50\Gamma_{\rm e}$ and $\Gamma_{\rm ph} = 12.5\Gamma_{\rm e}$.

4.4 Equivalent Circuit Analysis of Antenna Impedance

4.4.1 $R_{\rm L}C_0$ Parallel Circuit Model

In order to interpret the dependence on the amount of photoelectrons, we observe the obtained numerical results in terms of the antenna admittance $Y = 1/Z$. Figure 4.9 shows the real part G and the imaginary part B of the admittance Y for cases (a) and (b). G has an almost constant value for both cases (a) and (b), and the value is larger for case (a) than for case (b). On the other hand, the value of B clearly increases linearly with the frequency. One can find little difference in the B values between cases (a) and (b). We confirmed that the gradient of the B curve is equal to C_0. The simple dependence of the antenna admittance on the frequency implies that the photoelectron effects on the antenna impedance can be better represented by the parallel equivalent circuit rather than the series equivalent circuit.

In order to construct the equivalent electric circuit, we defined $R_{\rm L} = 1/G$, where $R_{\rm L}$ has the dimension of a resistance. For the imaginary part B, we set $B = \omega C_0$ because B increases linearly with the frequency. In this way, it is possible to construct an equivalent circuit composed of $R_{\rm L}$ and C_0 connected in parallel for the antenna impedance in the presence of photoelectrons, of which the diagram is shown in Figure 4.10. In middle and right panels of Figure 4.10, we presented the function form of the equivalent circuit. Evidently, behavior of both real and imaginary parts of the impedance is consistent with the simulation results shown in Figure 4.8. On the other hand, in the absence of photoelectrons, the antenna impedance is almost the same as its free-space characteristics, which is represented by the pure capacitance C_0. This is obtained as the limit of $R_{\rm L} \to \infty$ in the

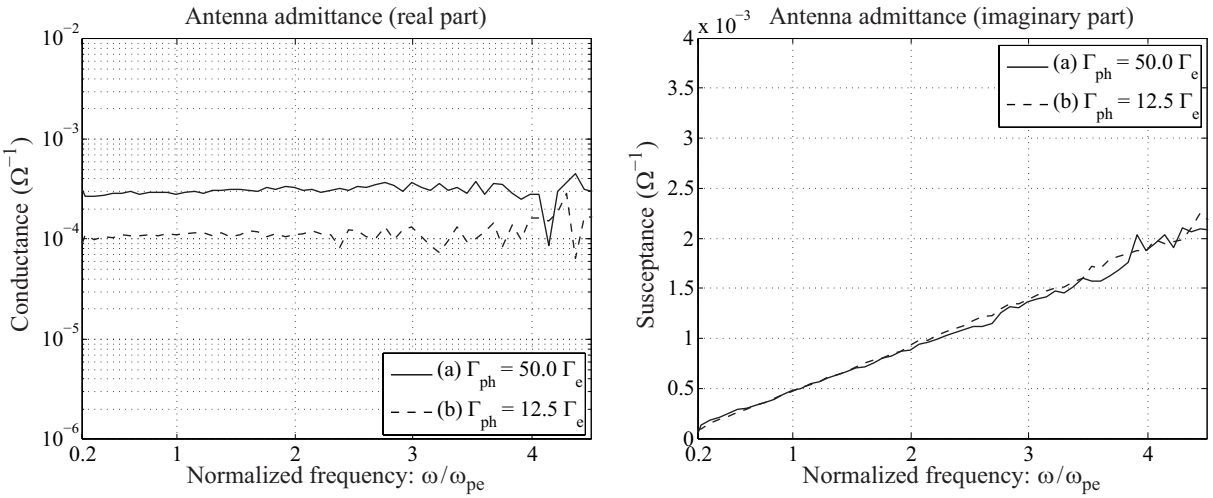

Figure 4.9: Antenna admittances for the cases of $\Gamma_{\rm ph} = 50\Gamma_{\rm e}$ and $\Gamma_{\rm ph} = 12.5\Gamma_{\rm e}$, the corresponding impedances of which are shown in Figure 4.8. The left and right panels show the antenna conductances and susceptances, respectively.

$R_{\rm L}C_0$ parallel circuit. The EM-PIC results also revealed that the dense photoelectrons lead to a smaller value of $R_{\rm L} = 1/G$ as shown in Figure 4.9. In summary of the present EM-PIC simulation results, the photoelectrons have the effect of reducing the value of $R_{\rm L}$, but have little effect on C_0.

The antenna surfaces contact with the highly conductive medium composed of the photoelectrons and the background plasma. In the aspect of electric circuit, this phenomenon can be modeled by adding a new path to the circuit, where the plasma conduction current flows, in parallel to C_0. The value of $R_{\rm L}$ controls the plasma conduction current flowing on the circuit path. $R_{\rm L}$ is occasionally referred to as "the Langmuir resistance", the effect of which is observed in the impedance profile in a low-frequency range [e.g., *Béghin* et al., 2005]. Note that the resistance $R_{\rm L}$ introduced here is not the conventional radiation resistance associated with the radiation of EM waves because EM waves are evanescent below the electron plasma frequency. Moreover, $R_{\rm L}$ must not be confused with the resistance caused by the dissipation of electrical energy due to the conversion of the field energy into the kinetic energy of plasma electrons. The latter resistance should be connected in series to C_0 and should have a peak at the local electron plasma frequency [*Kuehl*, 1967].

In the limit of high frequency, the $R_{\rm L}C_0$ parallel circuit becomes the pure capacitance C_0, and the presence of $R_{\rm L}$ has no effect on the total impedance of the circuit because C_0 behaves as a short circuit. As the frequency decreases, the influence of $R_{\rm L}$ becomes apparent. The real part $R_{\rm RC}$ and the imaginary part $X_{\rm RC}$ of the impedance of the $R_{\rm L}C_0$ parallel circuit are given as $R_{\rm RC} = R_{\rm L}/(1 + (\omega C_0 R_{\rm L})^2)$ and $X_{\rm RC} = -\omega C_0 R_{\rm L}^2/(1 + (\omega C_0 R_{\rm L})^2)$, respectively. Evidently, $R_{\rm RC}$ decreases with increasing frequency, and $|X_{\rm RC}|$ becomes smaller

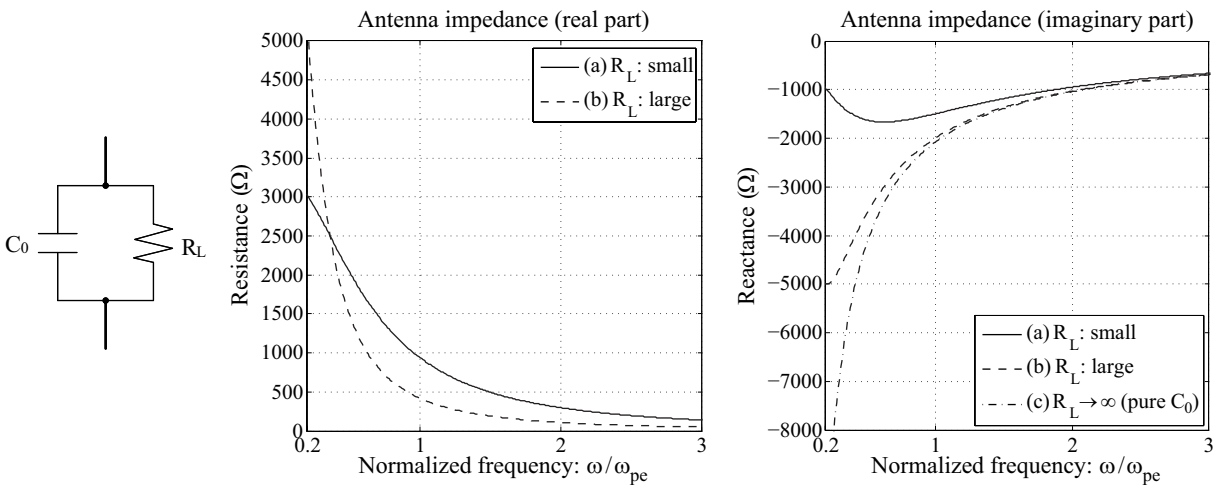

Figure 4.10: $R_{\rm L}C_0$ equivalent circuit diagram (left) and function forms of the real (middle) and imaginary (right) parts of the impedance of the circuit. In the middle and right panels, curves for (a) $R_{\rm L} = (3.1 \times 10^{-4})^{-1}$ Ω and (b) $R_{\rm L} = (1.0 \times 10^{-4})^{-1}$ Ω are plotted by solid and dashed lines, respectively. The dash-dotted line in the right panel shows the reactance curve corresponding to the pure capacitance C_0.

than the free-space reactance $|X_0| = 1/\omega C_0$ in a low-frequency range.

4.4.2 Analytical Calculation of Antenna Conductance

The antenna conductance can be estimated from $G = dI/dV$, where V and I are the antenna potential and the net current flowing into or out of the antenna surfaces, respectively. For simplicity in the analytical calculation, we assume that a small voltage signal excited at the antenna feeding point affects only the floating potential of the antenna, and not that of the spacecraft body. This assumption is valid when the capacitance of the spacecraft body is much larger than of the antenna.

In order to calculate G, we use the classical formulation for I shown in the studies, e.g., by *Mott-Smith and Langmuir* [1926]. After the derivation presented in the Appendix B, G can be given for the photoelectron and non-photoelectron cases as follows:

$$G = \frac{1}{2}\frac{e}{k_{\rm B}T_{\rm e} + eV_{\rm f}} I_{\rm e}(V_{\rm f}) + \frac{e}{k_{\rm B}T_{\rm ph}} I_{\rm ph}(V_{\rm f}) \qquad \text{(photoelectron case)}, \tag{4.1}$$

$$G = \frac{e}{k_{\rm B}T_{\rm e}} I_{\rm e}(V_{\rm f}) + \frac{1}{2}\frac{e}{k_{\rm B}T_{\rm i} - eV_{\rm f}} I_{\rm i}(V_{\rm f}) \qquad \text{(non-photoelectron case)}, \tag{4.2}$$

where $I_{\rm ph}(V_{\rm f})$, $I_{\rm e}(V_{\rm f})$, and $I_{\rm i}(V_{\rm f})$ are the currents of photoelectrons, background electrons, and ions, respectively, when the antenna has a floating potential $V_{\rm f}$. Note that, in the photoelectron case, we neglected an ion current because photoelectrons and background electrons form the dominant current.

In order to calculate Eqs. (4.1) and (4.2), we use the values of $I_{\rm ph}(V_{\rm f})$, $I_{\rm e}(V_{\rm f})$, and

$I_{\rm i}(V_{\rm f})$ which were numerically obtained from the EM-PIC simulation results for the case (a) $\Gamma_{\rm ph} = 50\Gamma_{\rm e}$. As described in Section 4.3.1, $I_{\rm ph}(V_{\rm f})$ and $I_{\rm e}(V_{\rm f})$ were equal to $1.7\,I_{\rm e0}$ for the photoelectron case. In the photoelectron case, the photoelectron and background electron currents are balanced with larger magnitude than $I_{\rm e0}$. This is a result of the positive floating potential $V_{\rm f} = 1.6\,k_{\rm B}T_{\rm e}/e$ for the photoelectron case. By substituting $I_{\rm ph}(V_{\rm f})$, $I_{\rm e}(V_{\rm f})$, $V_{\rm f}$, and other simulation parameters into Eq. (4.1) and transforming the value into the physical unit of Ω^{-1}, we obtain $G = 3.1 \times 10^{-4}\,\Omega^{-1}$, which agrees well with the EM-PIC simulation results for the case (a) $\Gamma_{\rm ph} = 50\Gamma_{\rm e}$ shown in Figure 4.9.

In the non-photoelectron case, $I_{\rm e}(V_{\rm f}) = I_{\rm i}(V_{\rm f}) \sim 7.0 \times 10^{-2}\,I_{\rm e0}$ was obtained as the EM-PIC simulation result. The background electron and ion currents are balanced at a much smaller magnitude than in the photoelectron case because the floating potential obtained for the non-photoelectron case had a negative value, i.e., $V_{\rm f} = -3.5\,k_{\rm B}T_{\rm e}/e$. As in the photoelectron case, G is calculated as $G = 3.4 \times 10^{-6}\,\Omega^{-1}$ and is much smaller than the photoelectron case. Using the obtained G (or $R_{\rm L}$) value, we can calculate the real and imaginary parts of the impedance at $\omega = \omega_{\rm pe}$ as $R_{\rm RC} = 15\,\Omega$ and $X_{\rm RC} = -2.1 \times 10^{3}\,\Omega$, respectively. We confirmed that $X_{\rm RC}$ is almost the same as the free-space reactance. Therefore, for such a small G value, the effect of $R_{\rm L}$ is not observed in the impedance profile near the electron plasma frequency.

4.5 Discussion

4.5.1 Equivalent Circuit for Non-photoelectron Case

In Section 4.4, we showed that the antenna impedance in photoelectron environment is well modeled by the parallel $R_{\rm L}C_0$ circuit, which was derived from the result showing the antenna conductance is almost constant with frequency. In this section, we discuss an equivalent circuit for the non-photoelectron case. Figure 4.11 shows the numerical result of the antenna admittance obtained for non-photoelectron case. In the panel (a), we also indicate the conductance value $G = 3.4 \times 10^{-6}\,\Omega^{-1}$ with the arrow, which was estimated in the previous section. Unlike the photoelectron cases, the conductance observed in non-photoelectron case clearly shows an increased trend with frequency, although the plot is rather scattered. The scattering might be simply due to the small magnitude of the conductance in comparison with the photoelectron case, which makes noise contribution stand out in the plot. However, the increased tread in the conductance plot suggests that the impedance characteristics in the non-photoelectron case cannot be well represented by the simple $R_{\rm L}C_0$ circuit.

In order to find out a suitable equivalent circuit for the non-photoelectron case, we tried to fit several types of circuits to the resultant conductance curve. As a result, we found that an additional small resistance $\sim 10^{1}\,\Omega$ connected to the conventional $R_{\rm L}C_0$ circuit can

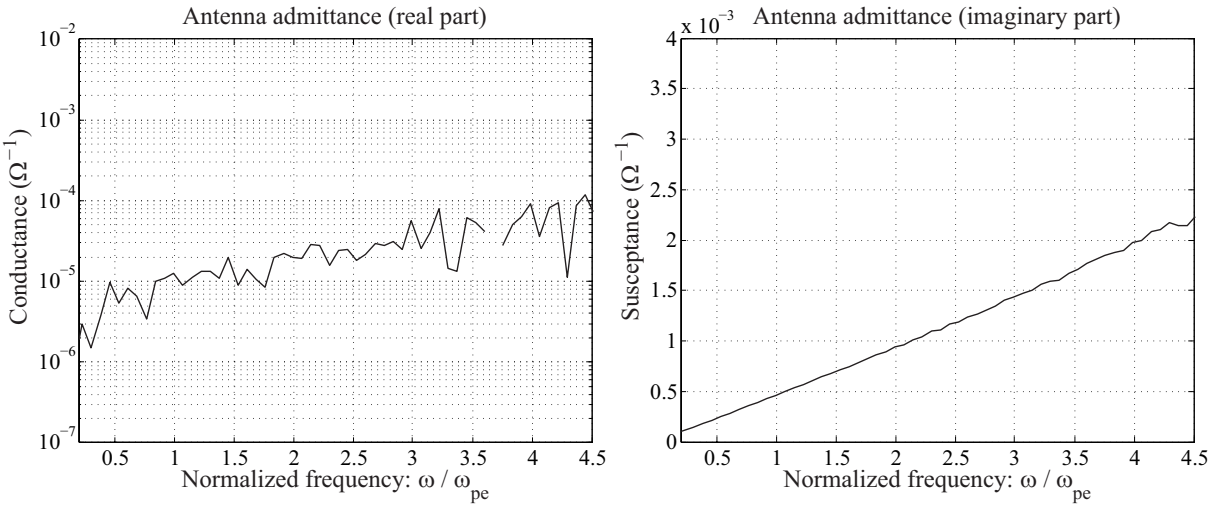

Figure 4.11: Antenna admittance for the non-photoelectron case. The left and right panels show the antenna conductance and susceptance, respectively. The arrow shown in the left panel indicates the conductance value of $G = 3.4 \times 10^{-6}\,\Omega^{-1}$, which is estimated for the non-photoelectron case in Section 4.4.2.

well model the increased trend observed in the non-photoelectron case. Figure 4.12 shows the diagram of the two types of newly proposed circuits and its frequency characteristics for the real part. In the figure, the solid and dashed curves are calculated from the circuits by using $G = 3.4 \times 10^{-6}\,\Omega^{-1}$ and $3.1 \times 10^{-4}\,\Omega^{-1}$ respectively and common $r = 15\,\Omega$, where the former and the latter correspond to non-photoelectron and photoelectron cases, respectively. We confirmed that both types of circuits yield almost the same characteristics of conductance for the above parameters. We also superimpose the simulation results for both cases. The increased trend observed for the non-photoelectron case is well reproduced by using the newly proposed circuits. On the other hand, when G is rather large as in the photoelectron case, the resultant conductance is almost flat even for the proposed circuits.

Some plausible factors can be considered responsible for the additional small resistance r. One is the radiation resistance resulting from radiation of EM waves. However, since the present antenna is electrically short, the radiation resistance is very small, and in the order of $10^{-1}\,\Omega$ for a frequency range of our interest even if the antenna is located in free space. In the present unmagnetized plasma, the radiation resistance is at least smaller than the free-space case, and should be zero for $\omega < \omega_{\rm pe}$ because EM waves are evanescent in the frequency range. Recalling that r was estimated at $15\,\Omega$ earlier, we must consider contribution of other factors to r. Another possibility is resistance caused by field energy conversion into the kinetic energy of plasma particles, which has been introduced in Chapter 3. By applying the EMF method, which has been used in Section 3.3.1, to

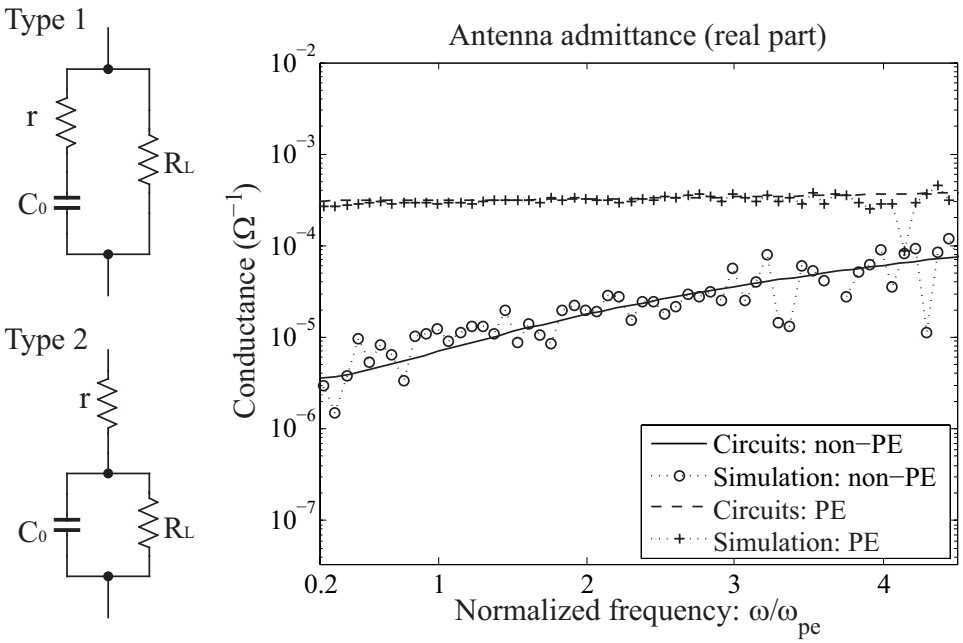

Figure 4.12: Diagrams of two types of equivalent circuits proposed for the antenna impedance in the non-photoelectron case and the plot of frequency characteristics of their conductance. We also superimpose the simulation results obtained for non-photoelectron and photoelectron cases.

the present situation, we can evaluate the order of the resistance as $\sim 10^1\,\Omega$ within the frequency range of the current interest, which is roughly consistent with the estimated value of r. From the discussion, the resistance due to field energy dissipation as a result of conversion into the kinetic energy of plasma particles can cause the increased trend of the conductance observed in the non-photoelectron. In the current status, however, we cannot conclude which type of the two circuit forms shown in Figure 4.12 is more appropriate representation for the antenna impedance in the non-photoelectron case, because both types of the circuit yield almost the same frequency characteristics of conductance for the present r value. The specification of the equivalent circuit should be carried out based on further numerical analyses adopting broad parameter ranges for photoelectrons and background plasmas, which is left as a future work.

From Figure 4.12, we can see that the proposed circuits provide good representation for conductance also in the photoelectron case. Because the contribution of the additional resistance r is not prominent in the case, the simpler $R_{\rm L}C_0$ circuit can become a satisfactory model as shown in the previous section. However, in a condition that the antenna is separated by an electron sparse region as in the non-photoelectron case, the impedance characteristics cannot be sufficiently represented by the simple $R_{\rm L}C_0$ circuit.

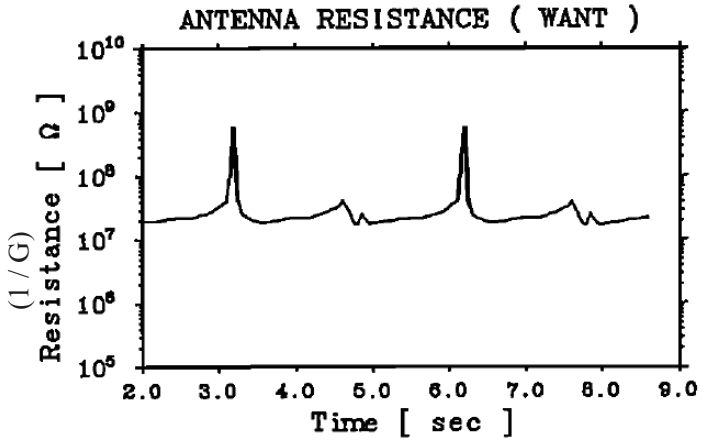

Figure 4.13: Time variations of $1/G$ observed for the WANT antenna aboard the GEOTAIL spacecraft [after *Tsutsui et al.*, 1997, Figure 13].

4.5.2 Comparison with In-flight Impedance Measurements

The present EM-PIC simulation revealed that a photoelectron cloud surrounding antennas behaves like a resistance R_{L} (or a conductance G) connected in parallel with a capacitance C_0. The result is basically consistent with empirical knowledge about the low-frequency impedance behavior in the presence of photoelectrons [e.g., *Okada et al.*, 2000]. We also note that the behavior is consistent with results of in-flight impedance measurements of electric field antennas aboard the GEOTAIL spacecraft [*Tsutsui et al.*, 1997]. In the measurements, the analogy with the equivalent circuit was observed at low frequencies of up to $\sim$100 Hz performed in the various regions of the Earth's magnetosphere.

As briefly introduced in Section 4.1, the spin-synchronized impedance change was observed in the GEOTAIL measurements. Figure 4.13 shows the time variations of $1/G$ of the WANT antenna during the period of about 6 s, which corresponds to two spin rotations of the GEOTAIL spacecraft [after *Tsutsui et al.*, 1997, Figure 13]. The figure clearly shows that the conductance G decreased ($1/G$ increased) at the same time of every half-spin period, which corresponds to the time when the antenna was directed toward the Sun. Since photoelectron flux is decreased for the antenna directed sunward, this phenomenon is explained by the spin modulation of photoelectron density around the antenna. It is basically consistent with the dependence of G on the photoelectron density revealed by the present simulations. Meanwhile, the large difference of appearance between the first/third peaks and the second/forth peaks has not been sufficiently resolved yet. We believe that further numerical analysis can contribute to more detailed interpretation of the in-flight antenna impedance measurements by the GEOTAIL spacecraft.

In the GEOTAIL measurements, the analogy with the parallel equivalent circuit

was observed at a sufficiently lower frequency range than the local electron plasma frequency. In the present analysis, however, the modification is found even near the electron plasma frequency, which is a much higher frequency range than the measurement results. Moreover, the EM-PIC results of $G \sim 10^{-4}\,\Omega^{-1}$ are large compared with the order of $G \sim 10^{-7}$–$10^{-9}\,\Omega^{-1}$ observed in the GEOTAIL measurements. This discrepancy may be due to the antenna modeling used in the present simulations. As described in Section 4.4.2, G is given as a function of the currents due to photoelectrons and background plasmas, which are emitted and collected by the antenna body, respectively. Evidently, the current values are significantly affected by the total area and the photoelectron-emitting area of the antenna surfaces. In the present simulation model, due to the limitation of the spatial resolution of the simulation, the diameter of the antenna was set to $\sim$0.08 times l_a. This radius and the resulting antenna surface area are unrealistically large considering actual wire antennas aboard scientific spacecraft, e.g., in the case of GEOTAIL the antenna diameter is $\sim 4.5 \times 10^{-6}$ times l_a. Therefore, in the present simulation, the large area of the antenna surface may amplify the effect on G.

4.6 Conclusion

This chapter describes the EM-PIC analysis on antenna impedance including plasma inhomogeneity caused by the photoelectron emission from conducting surfaces of an antenna and a spacecraft. In order to simulate the photoelectron emission, we performed electron injection from inner boundaries corresponding to sunlit antenna and spacecraft surfaces. We employed given photoelectron flux and energy as parameters and assume the Maxwellian for its energy distribution function.

The antenna impedance was analyzed in the EM-PIC simulation run for inhomogeneous plasma environment with and without photoelectrons. In the absence of photoelectrons, the background plasma has considerably small effect on the antenna impedance part, which has been predicted by conventional kinetic theories for a situation of comparable antenna length to the Debye length. In the presence of photoelectrons, however, large modification of the antenna impedance was observed in a low-frequency range. The real part increases with decreasing frequency, and the absolute value of the imaginary part becomes smaller than the free-space antenna reactance, which is not explained by the conventional theories.

Analysis using an equivalent electric circuit revealed that the impedance modification can be explained by introducing a finite resistance connected in parallel with the antenna capacitance. Theoretically, we formulated the resistance value by considering the contribution of the electron conduction current flowing into or out of the conductive antenna bodies when a small perturbation of the body potential is applied at an antenna

gap. The order of the estimated resistance value shows good agreement with that of EM-PIC simulation results, and we can confirm that the characteristic modification of the antenna impedance is caused by the large conducting current carried by the emitted photoelectrons.

In the present model, due to the unrealistically large antenna surface area, the simulation results of the conductance associated with the plasma conduction current is much larger than the value observed by the GEOTAIL spacecraft. In the future, in order to improve the proposed numerical tool, the antenna geometry must be modeled realistically and with better spatial resolution. Although a number of issues are left for future consideration, we showed the effectiveness of EMSES in its application to antenna analysis in complex situations that will be encountered when operating electric field antennas in space plasma environment.

Chapter 5

Analysis on the Receiving Characteristics of Electric Antennas for Future Satellite Missions

5.1 Introduction

In Chapters 3 and 4, we have investigated the characteristics of a space-based antenna for plasma wave measurements by simulating transmitting mode of the antenna. In the presence of the reciprocity relation between transmitting and receiving antennas, the delta-gap feeding method used in the previous chapters can be directly applied also to the analysis of receiving antennas. However, in plasma environment, the reciprocity has been strictly proved only in limited simple situations in past theories, e.g., for an isotropic plasma environment with a highly simplified ion-sheath structure [*Ishizone et al.*, 1976]. In order to extend the analysis of receiving antennas to environment of unknown reciprocity, we should develop a technique other than the delta-gap feeding method. As one of possible solutions, we can set up wave fields propagating in the simulation region and directly simulate the wave reception process by the antenna. For the application of EMSES to the receiving antennas in general plasma environments, we have developed a plug-in routine with this technique [*Miyake et al.*, 2008c].

Another important issue we should consider is the adaptation of EMSES to the analysis of modern electric field instruments, which are developed for future satellite missions and based on rather complex mechanics and electronics in comparison with a classical dipole-type antenna. Because it is too difficult to develop a theoretical model for such modern instruments, the application of the present numerical approach to the instruments is of primary importance.

In the present study, we focus on an electric field instrument designed based on a "hockey puck" principle [*Pedersen et al.*, 1998]. The notable feature of the instrument is the equipment of a guard electrode that can minimize photoelectron effects which are

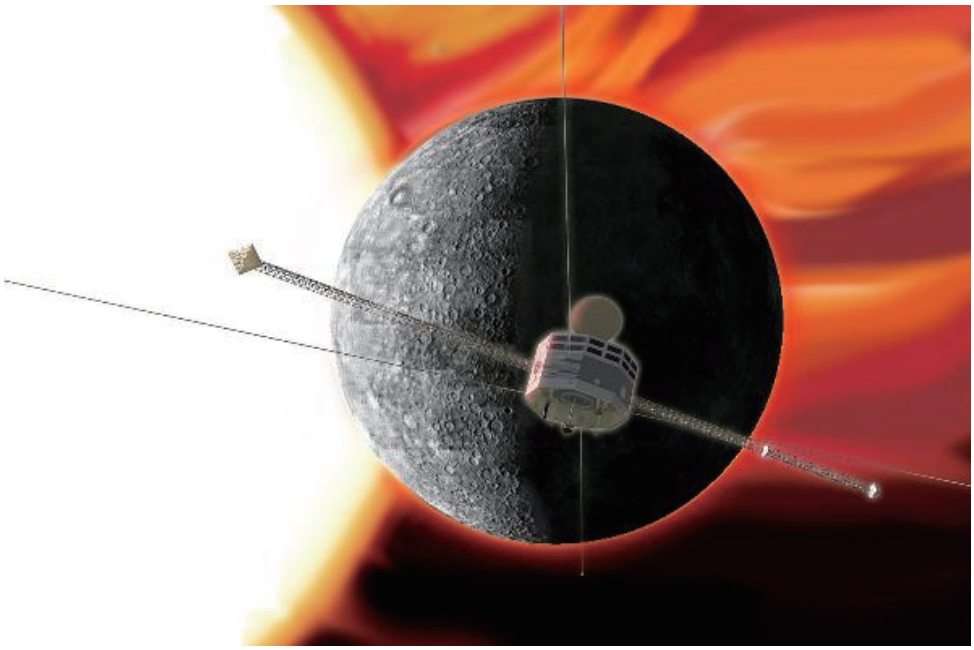

Figure 5.1: Image of Mercury Magnetospheric Orbiter (MMO). The image is the courtesy of RISH, Kyoto University.

formidable in electric field measurements particularly in DC and VLF ranges. Also, the geometry of the instrument is optimized for the DC electric field measurements, the details of which are presented in Section 5.3.1. As a result, it has been reported in the CLUSTER satellite mission that this type of the instrument has good performance in DC and VLF ranges [*Gustafsson et al.*, 2001]. However, there is a remaining problem for the instrument. The problem comes from the fact that electric field antennas must share plasma wave measurements as well as the DC electric field measurements. Basic properties as the effective length and the impedance in plasmas, which are important particularly for plasma wave observations at high frequencies, are insufficiently known due to its complex configuration. A strong demand for the better understanding of the characteristics of the instrument arises because a hockey-puck antenna called Mercury Electric Field In Situ TOol (MEFISTO) is planned to be onboard a future mission to Mercury: BepiColombo/MMO [*Blomberg*, 2006], the image of which is shown in Figure 5.1.

In order to understand the characteristics of an instrument designed based on the hockey puck principle, we performed the EM-PIC analysis on its characteristics in receiving external plasma waves. In Section 5.2, we present a newly introduced technique for computer experiments of the plasma wave reception and demonstrate the analysis by examining the effective length of relatively simple wire antennas. Section 5.3 is devoted to the detailed description of numerical models which are specially introduced for close analysis of MEFISTO. We particularly focus on the models for the puck-surface potential

control and the current biasing, the former of which particularly functions as the guard electrode. After that, we describe results of the computer experiments in Section 5.4. First, we describe the plasma environment in the vicinity of MEFISTO as a steady-state and the effects of the guard electrode and the current biasing on the environment. Finally, Section 5.4.3 presents results for the effective length and the impedance of MEFISTO in receiving external plasma waves.

5.2 Computer Experiments of Plasma Wave Reception with Wire Antennas

5.2.1 Numerical Technique and Model

In this section, we present a numerical technique introduced in EMSES for computer experiments of plasma wave reception. The analysis using the technique is demonstrated by examining the effective length of wire antennas which have relatively simple geometries. The application of the technique to the analysis of MEFISTO will be presented in Section 5.4.

Figure 5.2 shows the model of the current computer experiments. As shown in Figure 5.2(a), we make plasma waves propagate in the three-dimensional computational space and receive them by a numerical model of an electric field antenna placed in the center of the space. The numerical modeling of the antenna conducting bodies used in the present experiments is basically the same as that described in previous chapters. Presently, a gap point between the antenna conducting elements becomes an input point of the wave energy received by the antenna, which is an only different treatment from the previous chapters.

Setup of plasma waves

To examine the receiving antenna characteristics for both electrostatic and electromagnetic wave modes, we focus on the Langmuir and whistler modes as high-frequency electron waves in the present analysis. For simplicity, we assume and setup monochromatic, spatially uniform, plane waves for both modes at the initial states of the experiments.

For the setup of the Langmuir wave propagating along z-axis, we consider the wave electric field E_z which is a function of the position z and the time t and has the following form:

$$E_z = E_0 \cos(kz - \omega t) = \mathrm{Re}[E_0 \exp j(kz - \omega t)], \tag{5.1}$$

where E_0, k, and ω represent the wave amplitude, the wavenumber, and the wave frequency, respectively. By using Gauss's law $jkE_z = \rho/\epsilon_0$ and the continuity equation for charge $jkJ_z - j\omega\rho = 0$, the charge density ρ and the current density J_z can be obtained

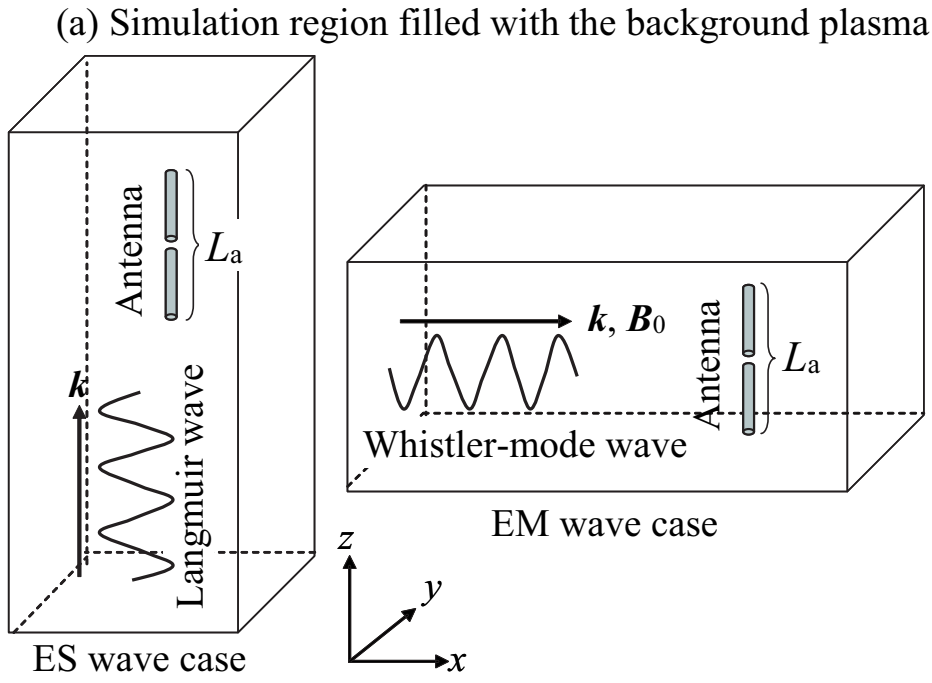

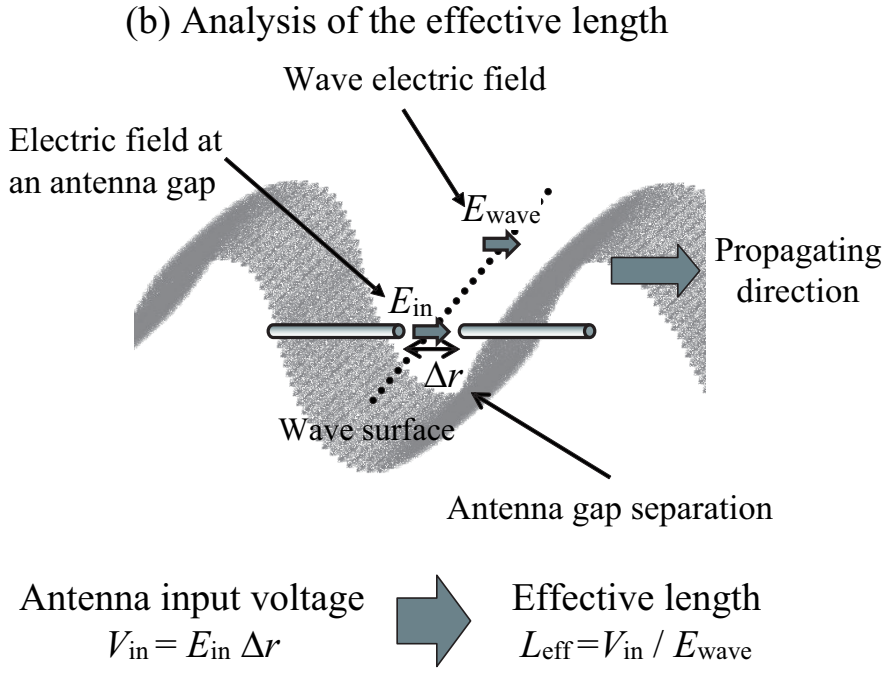

Figure 5.2: Model of computer experiments of the receiving antenna analysis. (a) Orientation of the antenna and the wavenumber vector. (b) Schematic illustration showing a calculation method of the effective length.

as follows:

$$\rho = -\epsilon_0 k E_0 \sin(kz - \omega t) = \mathrm{Re}[j\epsilon_0 k E_0 \exp j(kz - \omega t)] \tag{5.2}$$

$$J_z = -\epsilon_0 \omega E_0 \sin(kz - \omega t) = \mathrm{Re}[j\epsilon_0 \omega E_0 \exp j(kz - \omega t)]. \tag{5.3}$$

Here, k and ω satisfy the dispersion relation of the Langmuir wave, which is written as $\omega^2 = \omega_{\mathrm{pe}}^2(1 + 3k^2\lambda_{\mathrm{D}}^2)$, using the electron plasma frequency ω_{pe} and the Debye length λ_{D}.

For the setup of an initial wave field in computer experiments, we spatially modulate the density n_{e} and the first-order (oscillating) velocity $v_{\mathrm{e}1,x}$ for background electrons such that n_{e} and $v_{\mathrm{e}1,x}$ yield the above ρ and J_z at $t = 0$. We assume that the ion density and first-order velocity are hardly perturbed by the high-frequency wave of the current interest, i.e., $n_{\mathrm{i}} = n_0$ and $v_{\mathrm{i}1,\,x} = 0$. Then, n_{e} is given as

$$n_{\mathrm{e}}|_{t=0} = n_0 - \frac{1}{e}\rho = n_0 + \frac{\epsilon_0 k E_0}{e} \sin kz. \tag{5.4}$$

In the present experiments, we treat waves with amplitude enough small to be in the linear regime, i.e., the perturbation of the electron density is small as $|n_{\mathrm{e}} - n_0| \ll n_0$. Thus, $v_{\mathrm{e}1,x}$ should be modulated as

$$v_{\mathrm{e}1,x}|_{t=0} = -\frac{1}{n_0 e} J_z = \frac{\epsilon_0 \omega E_0}{n_0 e} \sin kz. \tag{5.5}$$

In summary, we setup the Langmuir wave field according to the following procedures.

1. Choose the wavelength λ (or the wavenumber k) which we want to examine.

2. Compute the wave frequency ω by performing the linear dispersion analysis.

3. Distribute electrons so that the electron density and the bulk velocity are modulated as given by Eqs. (5.4) and (5.5).

4. Solve Poisson's equation to obtain an initial profile of the wave electrostatic field.

Thanks to the procedure 4, we have no need to give wave electric field values explicitly at the initialization.

For the setting of the whistler-mode wave propagating along x-axis, we introduce the static magnetic field B_0 along x-axis and explicitly set wave electromagnetic fields and electron velocities which are modulated sinusoidally at the initialization of the computer experiments. Since some helpful literature is present for the field setting for whistler-mode waves [e.g., *Omura*, 1985], we don't describe the details here.

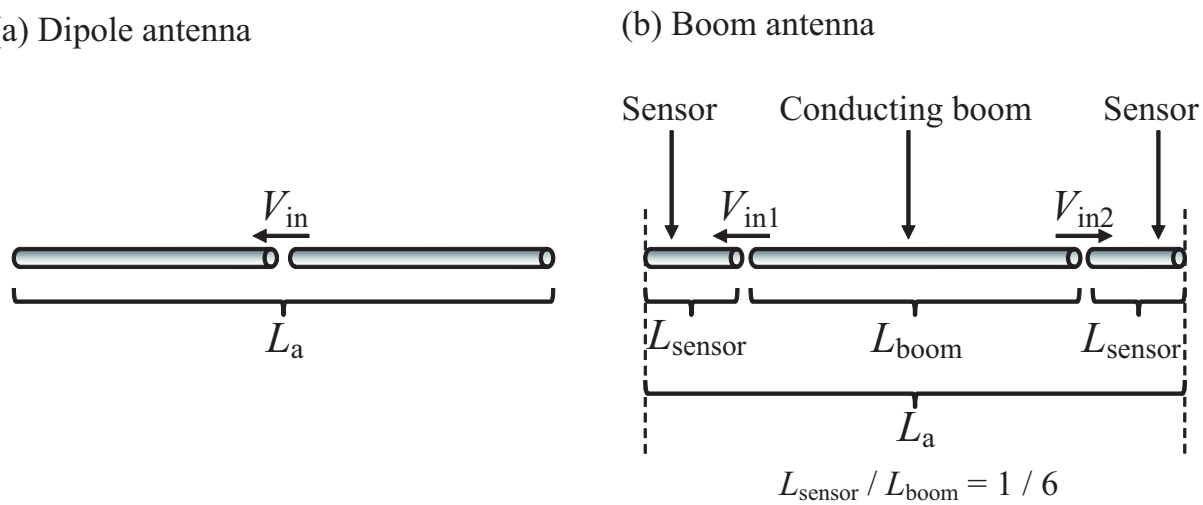

Figure 5.3: Wire antenna models examined in the computer experiments of the plasma wave reception. (a) Simple dipole antenna. (b) Linear-probe antenna.

Model of receiving antennas

Unlike the delta-gap feeding technique used in the analysis of a transmitting antenna, we do not give any electric field at a gap point pinched by antenna conducting elements in the current analysis. By simply placing the antenna conducting bodies in the propagating plasma waves, the antenna automatically starts to receive the waves, and received field energy is observed as a voltage signal at the gap. This situation corresponds to an open-circuit condition, i.e., an infinite load impedance is connected between the antenna sensing elements.

For the calculation of the effective length, we observed the wave electric field E_{wave} and the electric field E_{in} induced at the gap as shown in Figure 5.2(b). The input voltage V_{in} is then calculated by $E_{\mathrm{in}}\Delta r$. Finally, the effective length L_{eff} is obtained as $V_{\mathrm{in}}/E_{\mathrm{wave}}$ by its definition.

In this section, we examine two antenna models shown in Figure 5.3. Figure 5.3(a) is a simple dipole antenna that has a single antenna input. Meanwhile, the antenna model shown in Figure 5.3(b) has an intermediate structure between a wire antenna and a double probe. In principle, only conducting bodies placed at both ends compose sensing elements and the center conductor corresponds merely to a supporting boom. In this thesis, we call this antenna model a "linear-probe antenna" for convenience. For the linear-probe antenna, we observed induced voltages at two antenna gaps V_{in1} and V_{in2} shown in Figure 5.3(b) and calculate the total antenna input voltage by $V_{\mathrm{in}} = V_{\mathrm{in1}} - V_{\mathrm{in2}}$.

5.2.2 Analysis of Effective Length

For the validation of the introduced analysis technique, we examine the effective length by using the antenna models introduced in Section 5.2.1, excluding any sheath and photoelectron effects. For this aim, we utilize the "transparent" antenna treatment once used in Section 3.3, in which plasma particles can pass through the antenna location. In the current analysis, both antenna models are assumed to have the tip-to-tip length of $L_{\rm a} = 24$ measured in the simulation unit system. Meanwhile the wavelength of all plasma waves used in the current analysis is set to $\lambda \sim 21.3L_{\rm a}$ and is sufficiently larger than $L_{\rm a}$. The background plasma is composed of electrons and protons, and $\lambda_{\rm D}$ is set to $0.25L_{\rm a}$. By employing the above settings, we perform computer experiments for the Langmuir and whistler-mode waves. Figures 5.4 and 5.5 show simulation results for the Langmuir-wave reception for dipole and linear-probe antennas, respectively. The left and right panels show waveforms of $E_{\rm wave}$ and $V_{\rm in}$, respectively.

As shown in the figures, sinusoidal waveforms are observed as the antenna input voltage, which confirms the successful wave reception using the present analysis technique. As the ratio between amplitudes of $E_{\rm wave}$ and $V_{\rm in}$, the effective lengths are obtained as $L_{\rm eff} = 0.495L_{\rm a}$ and $0.780L_{\rm a}$ for the dipole and linear-probe antennas, respectively. The result for the dipole antenna, which approximately coincides with the half of the physical tip-to-tip length, is consistent with conventional knowledge for an electrically short antenna [*Gurnett*, 1998]. For the linear-probe antenna, though the sensing elements are only fractional parts at both ends, the resultant $L_{\rm eff}$ is larger than that of the dipole antenna.

Because an ES wave such as the Langmuir wave is well represented by the scalar potential, we interpret the results of $L_{\rm eff}$ based on a voltmeter principle, which is shown schematically in Figure 5.6. In the absence of DC charging of the antenna as the present analysis, the potentials $\phi_{\rm t1}$ and $\phi_{\rm t2}$ of two antenna terminals represent plasma potentials at certain positions. Then, the potential difference $\phi_{\rm t1} - \phi_{\rm t2}$ is obtained as $V_{\rm in}$. If we know the separation L between the positions that have unperturbed plasma potentials $\phi_{\rm t1}$ and $\phi_{\rm t2}$, we can obtain electric field intensity as $E = V_{\rm in}/L$. By definition described in the section of the simulation model, this distance L is evidently equivalent to the effective length $L_{\rm eff}$. Therefore, the potential distribution in the vicinity of the antenna has much information about the resultant value of $L_{\rm eff}$.

For a dipole antenna, it is well known that each antenna terminal has the plasma potential at its own midpoint. Therefore, the effective length coincides with the separation between the midpoints of two antenna terminals, i.e., the half of the tip-to-tip length. If we apply the idea to the linear-probe antenna, the effective length should become the separation between two midpoints of two sensing elements at both ends. For the present model shown in Figure 5.3(b), the effective length is then predicted as $0.875L_{\rm a}$ from the

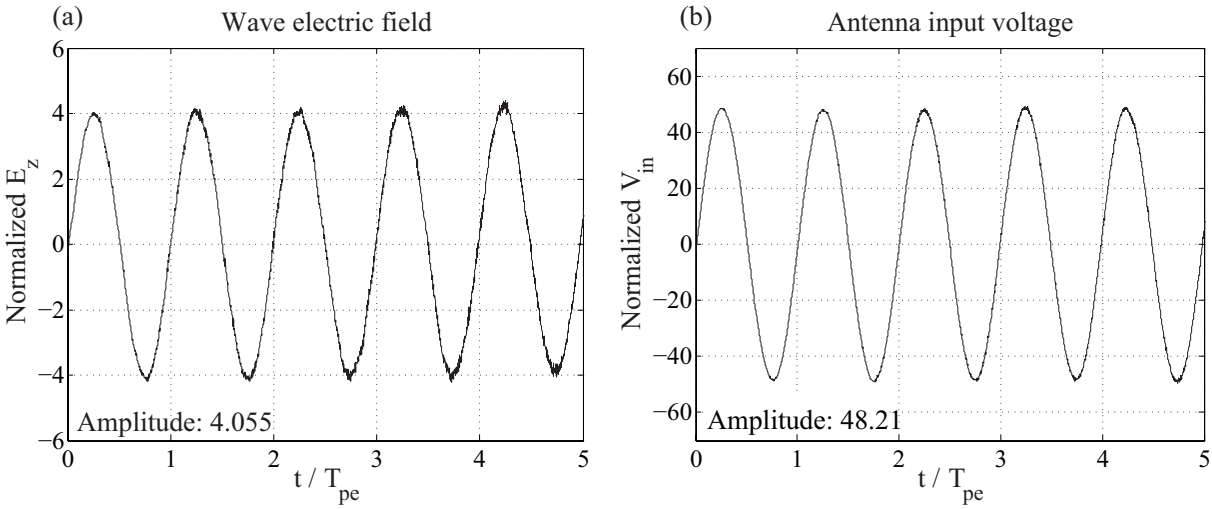

Figure 5.4: Result of the computer experiment of the wave reception by a simple dipole antenna. (a) Wave electric field measured at a certain locus in background plasma and on the same wavefront as the antenna center. (b) Waveform observed by the antenna as an input voltage.

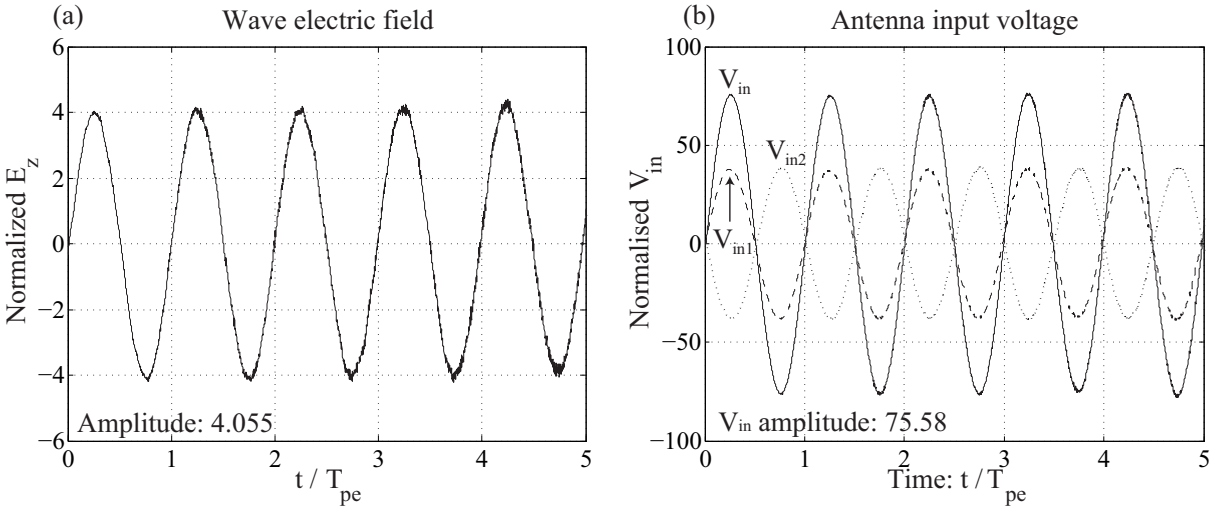

Figure 5.5: Result of the computer experiment of the wave reception by a linear-probe antenna. (a) Wave electric field measured at a certain locus in background plasma and on the same wavefront as the antenna center. (b) Waveforms observed by the antenna as input voltages. $V_{\mathrm{i}1}$ and $V_{\mathrm{i}2}$ represent the voltages independently observed at the two antenna input points. The total input voltage V_{in} is $V_{\mathrm{in}1} - V_{\mathrm{in}2}$.

idea. However, the actual numerical result $L_{\mathrm{eff}} = 0.780 L_{\mathrm{a}}$ is clearly shorter than the prediction.

To interpret the difference in detail, we plot a snap shot of the electric potential in the vicinity of the linear-probe antenna in Figure 5.7. The left and right panels show the one- and two-dimensional potential profiles. In the one-dimensional profile, the solid and dashed lines represent the potential along the antenna axis and the background plasma potential, respectively, the latter of which is unperturbed by the antenna. The dashed

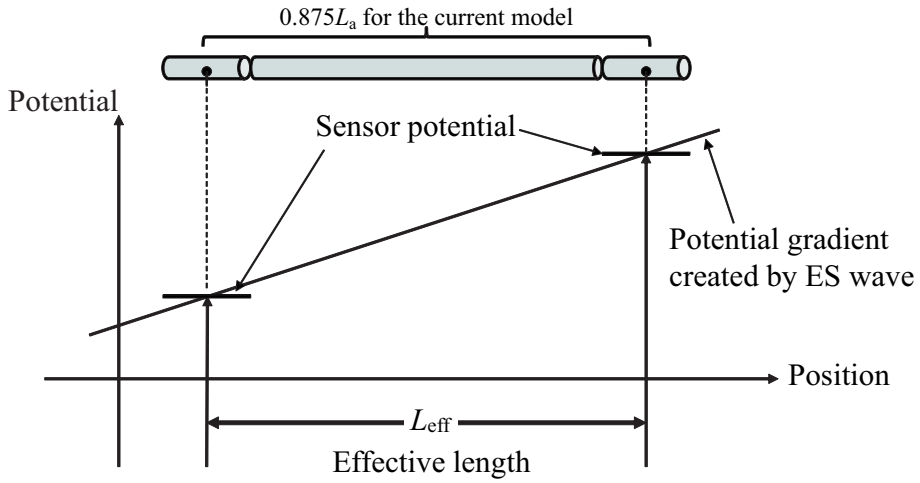

Figure 5.6: Schematic illustration showing a concept of the voltmeter principle. In the principle, sensing elements measure the background plasma potential at their midpoints. The resulting effective length is the separation between the two midpoints, which is, for instance, $0.875L_a$ for the current antenna model shown in Figure 5.3(b).

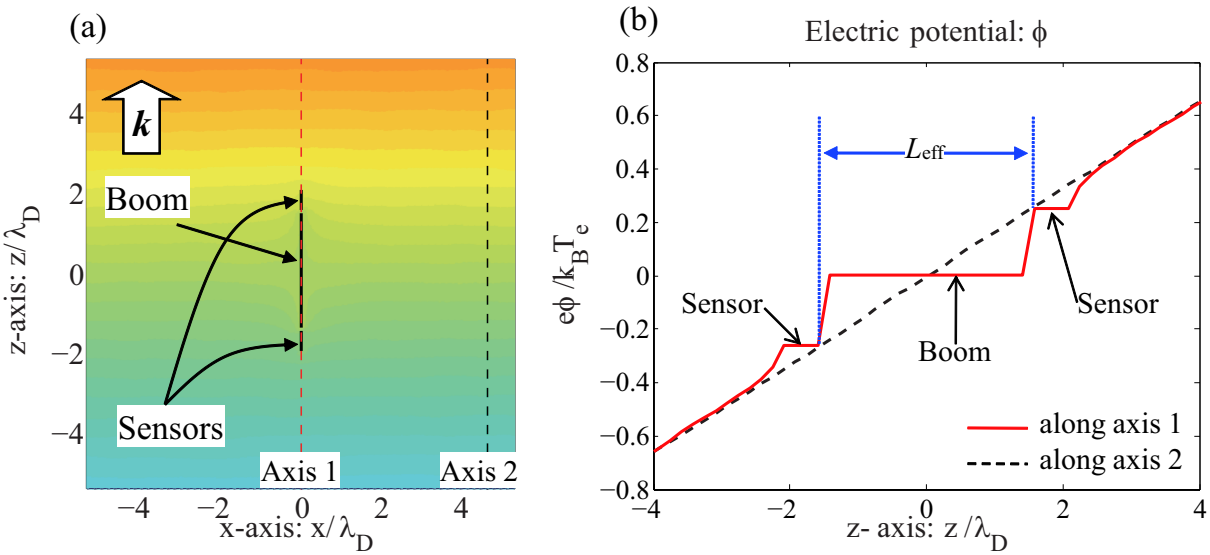

Figure 5.7: Snap shots of the electric potential in the vicinity of the linear-probe antenna. (a) Two-dimensional profile in x-z plane that includes the antenna. (b) One-dimensional profile along the axes 1 and 2 shown in the left panel.

line has a gradient that is created by the Langmuir wave electric field. By comparison between the solid and dashed lines, we find that two sensing elements represent the background plasma potentials at positions nearer boom than their own midpoints. This profile immediately follows the shorter effective length than the physical separation between the midpoints of the two sensing elements. The effect is caused by the center boom conductor, which tends to draw the sensor potentials close to its own potential. Although the effect has been known empirically by the name of a short-circuit effect in previous literature [*Pedersen et al.*, 1998], the quantitative evaluation of the effect requires numerical

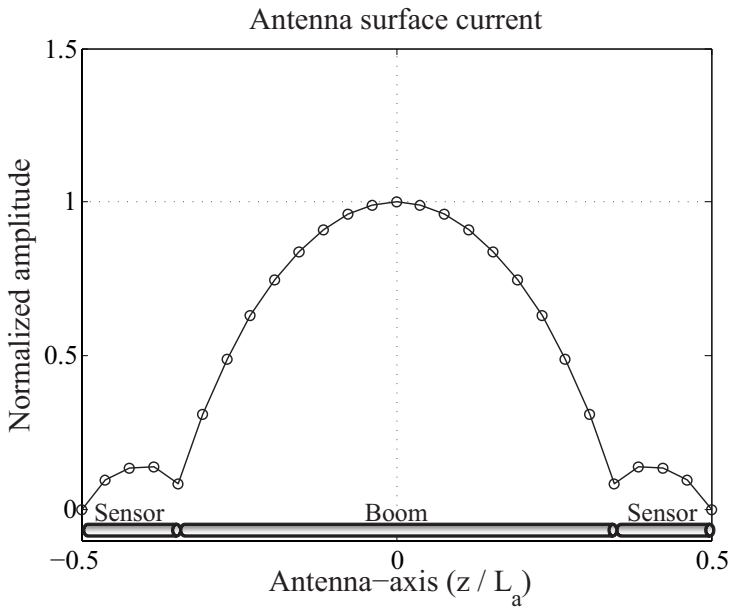

Figure 5.8: The normalized amplitude of the antenna surface current observed in the reception of the whistler-mode wave.

approaches as the present computer experiments.

We also examined the effective length for the whistler-mode wave. Although resultant waveforms are not displayed here, almost the same values for L_{eff} as the Langmuir-wave case are obtained for both dipole and linear-probe antennas. Figure 5.8 shows the normalized current magnitude distributed along the linear-probe antenna. It is clearly shown that the current is distributed not only on the sensing elements but also on the boom conductor. According to classical antenna theories [e.g., *Stutzman and Thiele*, 1997], the effective length for EM waves is formulated in terms of the antenna surface current when the antenna transmits waves. Because the current distribution does not satisfy the reciprocity generally, it is difficult to formulate the effective length by means of the current distribution when receiving plasma waves. However, the current distributed on the boom conductor suggests that the boom conductor also senses the wave electric field, which leads to the effective length much longer than only the length the sensing elements.

In summary, we successfully introduced an analysis technique which reproduces the plasma wave reception by an electric antenna. The technique is useful and effective for the quantitative analysis of the receiving antenna characteristics in more complex plasma environment. In the following sections, we applied the technique to the studies of the receiving characteristics of MEFISTO, which has complex functions such as the guard electrode and the current biasing as well as complex geometries.

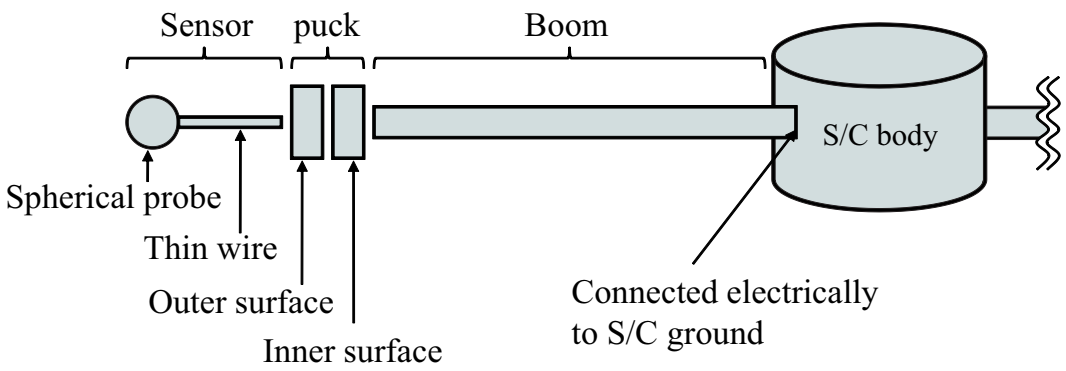

Figure 5.9: Schematic illustration of the MEFISTO sensor [*Blomberg et al.*, 2006].

5.3 Numerical Modeling of MEFISTO

5.3.1 MEFISTO Overview

In Sections 5.3 and 5.4, we investigate the receiving characteristics of MEFISTO in space plasma environment. MEFISTO is a double-probe electric field instrument designed based on the "hockey puck" principle as briefly introduced in Section 5.1. The double probe technique is optimal particularly for electric field measurements in DC and VLF ranges, in which pre-amplifiers should be as close as possible to the probe (ideally should be mounted inside the probe). For MEFISTO, in order to support reliable measurements also for a high-frequency (HF) range while satisfying the above requirement, a sensing element consists of not only a spherical probe but also a thin conducting wire. The pre-amplifier is mounted in a "puck" extended by a long boom from a spacecraft body, and a sensing element is attached outside the puck with the thin wire, which is much shorter than the boom. The separation of the sensor element from the pre-amplifier housing has another merit: we can choose a probe surface material optimizing the electrical contact with the surrounding environment at the same time as choosing a "puck" surface material providing an acceptable thermal environment for the pre-amplifier electronics. Although MEFISTO is made suitable particularly for flight in Mercury orbit, the "hockey puck" antenna itself can be a promising instrument also for other future missions. Therefore, precise and quantitative knowledge about its receiving characteristics is essential.

Figure 5.9 illustrates the MEFISTO sensor configuration for one side [*Blomberg et al.*, 2006]. In the figure, a spherical probe and a thin sensor wire have the same potential and form one sensing element. The external surface of a puck consists of two parts insulated electrically with each other. The potential values of the two surfaces can be set individually, and a policy about operational determination of the potential values will be described later. Finally, the conducting surface of the boom functions as a shield of signal

lines between electronics inside the puck and the spacecraft. The boom surface is then connected to the spacecraft ground. Since the same system as the figure is extended also to an opposite side, the entire system has seven independent potentials: ϕ_{s1} and ϕ_{s2} for two sets of the sensing elements, ϕ_{o1}, ϕ_{o2}, ϕ_{i1}, and ϕ_{i2} for two sets of the outer and inner puck surfaces, and ϕ_b for the bodies of the spacecraft (and the boom). The potential difference $\phi_{s1} - \phi_{s2}$ is measured as a final output voltage.

Although MEFISTO is reported to give optimal measurements at low frequencies [*Blomberg et al.*, 2006], the following problems about the receiving characteristics remain unresolved for more reliable measurements over a wide-frequency range.

- Basic characteristics such as the impedance and the effective length have not been sufficiently understood for MEFISTO. This is because MEFISTO has very different and complex structure from classical electric field instruments such as WANT and PANT onboard the GEOTAIL spacecraft.

- The quantitative evaluation of the MEFISTO performance in a HF range is insufficient, because MEFISTO is designed so that the optimal operation is primarily achieved in low-frequency ranges.

- The behavior and distribution of photoelectrons in the vicinity of the sensor are rather complex. The independent potential values on the surfaces of the sensor, puck, and boom can much influence the orbits of the photoelectrons. For MEFISTO, it is planned to minimize undesirable photoelectron effects by taking advantage of the operational control of the puck-surface potential. To do this, however, we need to investigate photoelectron behavior around the sensor in advance.

In order to work on the above issues, we newly introduced numerical models of MEFISTO in the EMSES code. We particularly focus on the operational control of the puck-surface potential and the bias current provided to the sensing elements. We also introduced a numerical model of a finite load impedance, which is necessary for the evaluation of antenna impedance during the computer experiments of plasma wave reception.

5.3.2 Operational Control of Puck Surface Potential

The puck surface functions as a guard or an attractor for photoelectrons, the potential of which should be determined such that undesirable photoelectron effects are minimized. The inner (boom-side) surface of the puck is called a guard electrode, which is planned to be kept $\sim$10 V negative with respect to the spacecraft body in the baseline specification of MEFISTO. The objective of the guard electrode is to repel photoelectrons emitted from the spacecraft body (and the boom). On the other hand, the outer (sensor-side) surface

is called a stub and kept $\sim 5\,\mathrm{V}$ positive with respect to the sensing elements. The stub will attract photoelectrons emitted from the probe and prevent them from escaping from the sensor elements. Roughly, the magnitude of the above potentials is enough to change the photoelectron orbits, the typical energy of which is a few eV. However, the optimal values have not been known sufficiently yet and may change depending on a surrounding plasma environment. Hence, the above values will be used only as a rough guide.

In EMSES, we simulate the above potential control by forcibly moving charge at every time step between the puck surfaces and the spacecraft body. Practically, this can be performed by the extension of the Capacity Matrix method. In the formulation described hereinafter, all equations are simplified assuming that only one set of a sensor and a puck exists in the simulation system. Though two sets are actually extended oppositely, the extension of the following formulation for the actual situation is straightforward. The first step we should do is to obtain the representations for the modification of the total charge ΔQ_e possessed by a conducting element $\mathrm{e} \in \{\mathrm{s}, \mathrm{o}, \mathrm{i}, \mathrm{b}\}$ in terms of all conducting body potentials: ϕ_s, ϕ_o, ϕ_i, and ϕ_b, where "s", "o", "i", and "b" denote the sensor, the outer and inner surfaces of the puck, and the spacecraft body, respectively. Here, ΔQ_e is given by $\sum_{i\in E} \delta\rho_i \times \Delta r^3$ using the charge density modification $\delta\rho_i$ on the grid i, where the set E consists of all grid points composing the conducting element "e". Because the relation between the charge density and the potential on each grid is defined in the Capacity Matrix method, we can derive ΔQ_e ($\mathrm{e} \in \{\mathrm{s}, \mathrm{o}, \mathrm{i}, \mathrm{b}\}$) by extending Eq. (2.10) described in Section 2.3.4 as follows:

$$\frac{1}{\Delta r^3}\begin{pmatrix} \Delta Q_\mathrm{s} \\ \Delta Q_\mathrm{o} \\ \Delta Q_\mathrm{i} \\ \Delta Q_\mathrm{b} \end{pmatrix} = \begin{pmatrix} C_\mathrm{ss} & C_\mathrm{so} & C_\mathrm{si} & C_\mathrm{sb} \\ C_\mathrm{os} & C_\mathrm{oo} & C_\mathrm{oi} & C_\mathrm{ob} \\ C_\mathrm{is} & C_\mathrm{io} & C_\mathrm{ii} & C_\mathrm{ib} \\ C_\mathrm{bs} & C_\mathrm{bo} & C_\mathrm{bi} & C_\mathrm{bb} \end{pmatrix} \begin{pmatrix} \phi_\mathrm{s} \\ \phi_\mathrm{o} \\ \phi_\mathrm{i} \\ \phi_\mathrm{b} \end{pmatrix} - \begin{pmatrix} \sum_{i\in S}\sum_j C_{ij}\phi_{0j} \\ \sum_{i\in O}\sum_j C_{ij}\phi_{0j} \\ \sum_{i\in I}\sum_j C_{ij}\phi_{0j} \\ \sum_{i\in B}\sum_j C_{ij}\phi_{0j} \end{pmatrix}, \tag{5.6}$$

where the sets S, O, I, and B for the sensor, the outer and inner surfaces of the puck, and the spacecraft body, respectively are defined in the same manner as the set E described above. The summation for the index j appeared in the last term should be performed for all grid points defined on all conducting bodies. Then, ϕ_{0j} represents a potential value on the grid j before performing the surface charge redistribution. We can compute the elements of the matrix appeared in the first term of the right-hand side of Eq. (5.6) from the elements C_{ij} of the capacity matrix described in Appendix A. For example, C_so is given by

$$C_\mathrm{so} = \sum_{i\in S}\sum_{j\in O} C_{ij}. \tag{5.7}$$

Our goal is to obtain ϕ_s, ϕ_o, ϕ_i, and ϕ_b from Eq. (5.6). Because the potential differences $\Delta\phi_\mathrm{os} = \phi_\mathrm{o} - \phi_\mathrm{s}$ and $\Delta\phi_\mathrm{ib} = \phi_\mathrm{i} - \phi_\mathrm{b}$ are given as input parameters of the guard electrode, the number of unknown potential values reduce to only two. We therefore need two restraint

conditions in order to solve the simultaneous equations. In the present situation, we use the charge conservation condition given by

$$\Delta Q_{\rm s} = 0, \tag{5.8}$$

$$\Delta Q_{\rm o} + \Delta Q_{\rm i} + \Delta Q_{\rm b} = 0. \tag{5.9}$$

Here, the second condition is derived by considering that the charge should be moved between the spacecraft and the puck (including both inner and outer surfaces). Then, the final form of the simultaneous equations to be solved are given as follows:

$$\begin{pmatrix} D_{11} & D_{12} \\ D_{21} & D_{22} \end{pmatrix} \begin{pmatrix} \phi_{\rm s} \\ \phi_{\rm b} \end{pmatrix} = - \begin{pmatrix} E_{11} & E_{12} \\ E_{21} & E_{22} \end{pmatrix} \begin{pmatrix} \Delta\phi_{\rm os} \\ \Delta\phi_{\rm ib} \end{pmatrix} + \begin{pmatrix} \sum_{i\in S} \sum_j C_{ij}\phi_{0j} \\ \sum_{i\in O\cup I\cup B} \sum_j C_{ij}\phi_{0j} \end{pmatrix}, \tag{5.10}$$

where

$$\begin{aligned} D_{11} &= C_{\rm ss} + C_{\rm so}, \\ D_{12} &= C_{\rm sb} + C_{\rm si}, \\ D_{21} &= C_{\rm os} + C_{\rm oo} + C_{\rm is} + C_{\rm io} + C_{\rm bs} + C_{\rm bo}, \\ D_{22} &= C_{\rm ob} + C_{\rm oi} + C_{\rm ib} + C_{\rm ii} + C_{\rm bb} + C_{\rm bi}, \\ E_{11} &= C_{\rm so}, \\ E_{12} &= C_{\rm si}, \\ E_{21} &= C_{\rm oo} + C_{\rm io} + C_{\rm bo}, \\ E_{22} &= C_{\rm oi} + C_{\rm ii} + C_{\rm bi}. \end{aligned} \tag{5.11}$$

By solving Eq. (5.10) for $\phi_{\rm s}$ and $\phi_{\rm b}$, we can obtain potential values for all conducting elements, which satisfy the intended puck-surface potentials with regard to the probe and the spacecraft body. Once we obtain the potential values, we can immediately modify the associated electrostatic field component by the method described in Section 2.3.4.

5.3.3 Modeling of Sensor Current Biasing

A bias current generator of MEFISTO provides the sensing elements with a constant current to keep the sensor potential close to a local plasma potential. An original purpose of keeping the sensor potential at the plasma potential is that the spacecraft potential can be monitored as the difference between an averaged potential of the two sensors and that of the spacecraft body [*Ishisaka*, 2000], which is basically different operation from the electric field measurement. Because the current biasing clearly affects the photoelectron distribution around the sensor, we need to investigate its effects on antenna receiving characteristics.

Generally, the necessary magnitude of the bias current in order to keep the sensor potential at the plasma potential is difficult to know precisely in space, because it depends on conditions of the photoelectron emission and the surrounding plasma. In actual

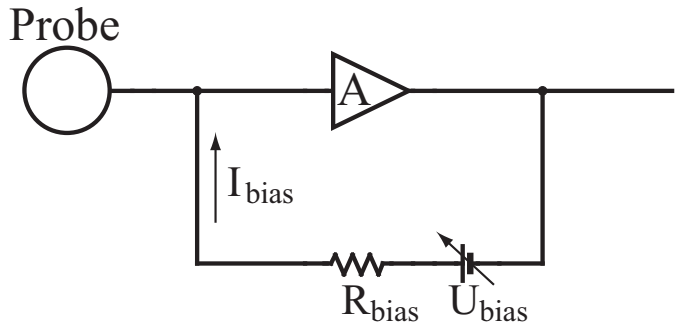

Figure 5.10: Schematic diagram of the bias current generator [*Åhlén and Ishisaka*, private communication].

missions, a comfortable value of the bias current is determined by once sweeping the current magnitude monitoring the sensor–spacecraft voltage. From a principle of an emissive probe which is a kind of the Langmuir probe, the slope of the voltage–current characteristic curve would have a sharp change at the sensor potential close to the local plasma potential [*Hershkowitz*, 1989]. By this trial, one can estimate the optimal magnitude for the bias current.

For MEFISTO, the bias current is produced actually by a positive feedback circuit, a simplified diagram of which is shown in Figure 5.10. In the circuit, the gain A is adjust as close to 1 as possible, while assuring that A never exceeds 1 in order to avoid instabilities. As a result, the current generator outputs the constant bias current $I_{\rm bias} = U_{\rm bias}/R_{\rm bias}$, where $U_{\rm bias}$ and $R_{\rm bias}$ are the voltage source and the resistance, respectively, used in the bias current circuit. Another purpose of using the feedback circuit is to make the sensor input impedance as large as possible, which will be mentioned later.

In order to model the bias current in EMSES, we constantly move the charge $I_{\rm bias}\Delta t$ at every time step between the sensor and the spacecraft body, where $I_{\rm bias}$ is the intended bias current value given as an input parameter. We can realize this treatment by slightly modifying Eqs. (5.8) and (5.9) as follows:

$$\Delta Q_{\rm s} + I_{\rm bias}\Delta t = 0 \tag{5.12}$$

$$\Delta Q_{\rm o} + \Delta Q_{\rm i} + \Delta Q_{\rm b} - I_{\rm bias}\Delta t = 0. \tag{5.13}$$

The adjustment of the bias current value to keep the sensor at the background plasma potential in computational experiments is much easier than in actual missions in space, because the complete potential profile in the vicinity of the spacecraft is always available in the computer experiments. However, in order to reproduce actual operations in space, we also conducted computer experiments for various magnitude of the bias current. The experiments will be described in Section 5.4.2.

5.3.4 Modeling of Finite Load Impedance

The finite load impedance $Z_{\rm L}$ is responsible for the attenuation and the phase shift of the input voltage $V_{\rm in}$ in combination with the impedance of the sensor itself. For MEFISTO, $Z_{\rm L}$ can be effectively regarded as a resistance $R_{\rm L}$ and a capacitance $C_{\rm L}$ connected in parallel. In the present baseline assumption, $C_{\rm L}$ is about 4 pF, which is in the same order as the free-space capacitance of the sensor itself [*Åhlén*, private communication; *Olson*, 2006]. The value of $R_{\rm L}$ depends on a frequency range of interest. At low-frequencies, a major factor determining $R_{\rm L}$ is the feedback circuit shown in Figure 5.10. The feedback circuit has an input impedance $R_{\rm bias}/(1-A)$. Because of the feedback circuit with $A \sim 1$, $R_{\rm L}$ at low-frequencies becomes so large ($\sim$100 GΩ [*Åhlén*, private communication]), which assures almost an ideal, open-circuit measurement. For higher-frequencies, however, $R_{\rm L}$ decreases gradually with the increasing frequency and finally reduced to the order of MΩ at $\sim$100 MHz.

In the present analysis, assuming that $Z_{\rm L}$ is composed of $R_{\rm L}$ and $C_{\rm L}$ connected in parallel, we introduced a numerical model which enables us to set arbitrary values for $R_{\rm L}$ and $C_{\rm L}$. Actually, the model is coded in the update of the electric field in EMSES. When the input voltage $V_{\rm in}$ is applied to $Z_{\rm L}$, the following current $I_{\rm L}$ should flow to the load.

$$I_{\rm L} = \frac{V_{\rm in}}{Z_{\rm L}} = \frac{V_{\rm in}}{R_{\rm L}} + C_{\rm L}\frac{dV_{\rm in}}{dt} = \frac{E_{\rm in}\Delta r}{R_{\rm L}} + C_{\rm L}\Delta r\frac{dE_{\rm in}}{dt}, \tag{5.14}$$

where we used $V_{\rm in} = E_{\rm in}\Delta r$. Considering that the current (density) should be defined at the half-integer time step while the electric field at the integer time step, the above is rewritten as

$$I_{\rm L}^{n+1/2} = \frac{\Delta r}{R_{\rm L}}\frac{E_{\rm in}^{n+1}+E_{\rm in}^{n}}{2} + \frac{C_{\rm L}\Delta r}{\Delta t}(E_{\rm in}^{n+1}-E_{\rm in}^{n}), \tag{5.15}$$

where we took the average of $E_{\rm in}^{n+1}$ and $E_{\rm in}^{n}$ to obtain $E_{\rm in}$ at the half-integer time step. The above current is added as the current density $J_{\rm L} = I_{\rm L}/\Delta r^2$ to the equation for the update of the electric field at the grid point between the sensor wire and the boom. After some arrangement, we finally obtain a following form for the update equation of the electric field:

$$\begin{aligned}\boldsymbol{E}^{n+1} = \frac{1-\frac{\Delta t}{2\epsilon_0 R_{\rm L}\Delta r}+\frac{C_{\rm L}}{\epsilon_0\Delta r}}{1+\frac{\Delta t}{2\epsilon_0 R_{\rm L}\Delta r}+\frac{C_{\rm L}}{\epsilon_0\Delta r}}\boldsymbol{E}^{n} &+ \frac{c^2\Delta t}{1+\frac{\Delta t}{2\epsilon_0 R_{\rm L}\Delta r}+\frac{C_{\rm L}}{\epsilon_0\Delta r}}\nabla\times\boldsymbol{B}^{n+\frac{1}{2}} \\ &- \frac{\Delta t}{\epsilon_0\left(1+\frac{\Delta t}{2\epsilon_0 R_{\rm L}\Delta r}+\frac{C_{\rm L}}{\epsilon_0\Delta r}\right)}\boldsymbol{J}^{n+\frac{1}{2}}.\end{aligned} \tag{5.16}$$

By using the above instead of the normal update equation only at antenna input points, we can include an effect of the finite load impedance in the computer experiments.

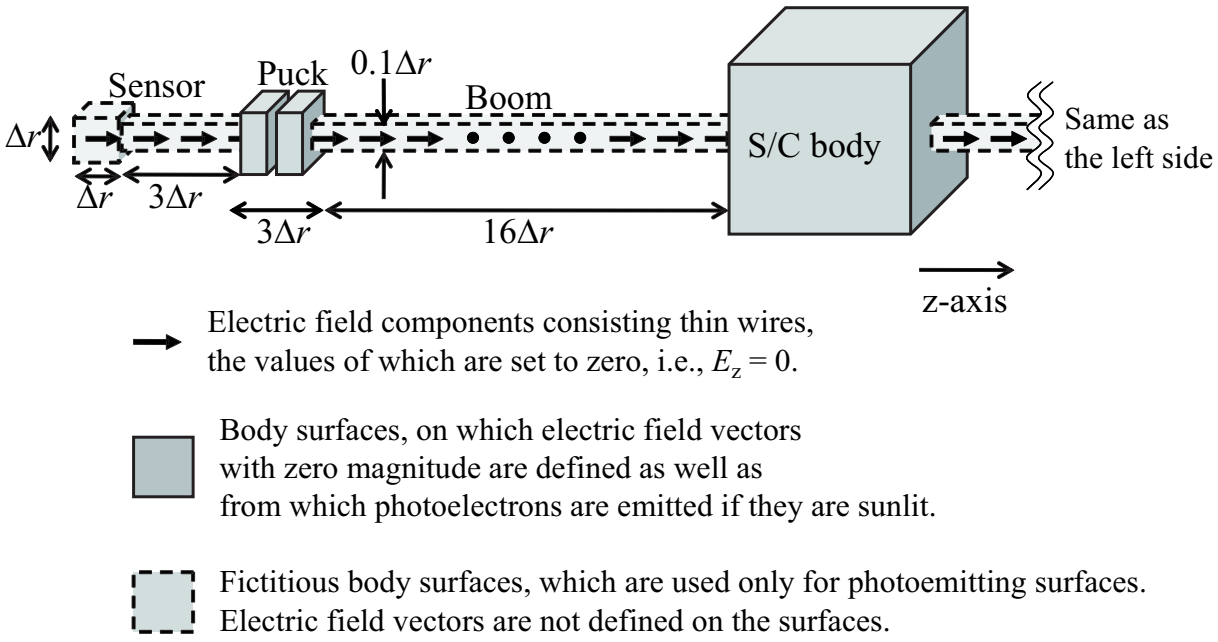

Figure 5.11: Configuration and dimensions of the numerical model of MEFISTO used in the present computer experiments. Note that the configuration and dimensions are modified from the original ones for tractability in the computer experiments. A tip-to-tip length L_a is set to $52\Delta r$.

5.4 Results of Computer Experiments

5.4.1 Experimental Setup and Parameters

The setup of the computer experiments for the receiving characteristics of MEFISTO is basically the same as that shown in Figure 5.2. As heretofore, we place the antenna in the center of the computational space, which is filled with background plasmas consisting of electrons and ions. The model of the antenna is replaced with the MEFISTO model that includes the treatments of the guard electrode (puck-surface potential control) and the current biasing newly introduced in the previous section. We also simulate the photoemission by the same method as presented in Section 4.2.

The detailed structure of the MEFISTO model is shown in Figure 5.11. The model includes spacecraft and two puck bodies. Since we have to describe the antenna geometry with a limited number of rectangular grid elements, some parts of the actual fine structure are difficult to model. Our baseline assumption is that the spacecraft body and the pucks have a rectangular shape, which is not realistic particularly for the spacecraft. The sensor wires and the boom cylinders are represented electrically by a single column of the computational grid points. We set the electric field values defined between the grid points to zero in order to simulate the perfect conducting behavior. A problem for this fashion of the conducting wire modeling is ambiguity of the thickness of the wire.

In previous studies, a wire modeled by the method is reported to have an equivalent radius of $\exp(-2)\Delta r \sim 0.14\Delta r$ [e.g., *Uno*, 1998]. In order to model the real radius 0.144 mm of the sensor wire according to the rule, we must set $\Delta r = 1$ mm, which is too small to realize within a presently available computational resource. We therefore set Δr comparable to the shielding length for photoelectrons, i.e., typically $\sim 10^2$ mm, which is the smallest scale of the dynamics of charged particles around the antenna. As a trade-off, the effective thickness of the wire parts becomes unrealistically large in the present experiments. Moreover, the real radius of a spherical probe, i.e., 40 mm is also smaller than Δr, and thus we cannot model the spherical structure of the probe in the present model. We, therefore, will mainly discuss the effects of surrounding plasma environments on the resultant sensor characteristics rather than their absolute values.

For the simulation of the photoelectron emission and particle absorption by conducting bodies, we also need to define solid surfaces that are sensed by superparticles. For the spacecraft and puck bodies, the solid surfaces accord with mesh surfaces on which perfect conducting conditions for the field components are employed. For the sensor and boom wires, however, we cannot setup solid surfaces in accordance with mesh surfaces, because the wire is defined electrically by only a single column of the computational grid points. Thus, we must determine fictitious solid surfaces independent of the conducting body assignment on grid points. In Figure 5.11, the setup of the fictitious solid surfaces is also illustrated. We presently used $0.1\Delta r$ for the thickness of the wire. At the end of the sensor wire we attach a cubic body with the length Δr on each side, which corresponds to the spherical probe.

There are two important parameters newly introduced in the current analysis, i.e., the puck-surface potential setting and the magnitude of the bias current. In the following analysis, we basically compare three cases with and without the puck-surface potential (PC) control and the bias current (BC): (a) PC: on, BC: on, (b) PC: off, BC: on, and (c) PC: on, BC: off. We set an inner-puck-surface potential to $-8k_{\rm B}T_{\rm ph}/e$ and outer-puck-surface potential to $+2k_{\rm B}T_{\rm ph}/e$ with respect to the boom (and spacecraft) potential and the sensor potential, respectively. For BC, we perform several computer experiments using different current magnitudes and finally choose a magnitude that gives an optimal sensor potential close to the background plasma potential. In the present analysis, we treat a symmetric photoelectron case to concentrate on the fundamental behavior of MEFISTO. In the symmetric case, the sun-satellite direction (set to x-axis) is perpendicular to the sensor direction. In the case, photoelectrons are expected to distribute in a symmetric manner, which is considered a well-behaved situation for the sensor.

Except for the puck-surface potentials and the magnitude of the bias current, most of parameters used in the present computer experiments are identical to those listed in Table 4.1. We set the energy and flux ratios between photoelectrons and plasma electrons

as $\phi_{\rm ph}/\phi_{\rm e} = 1/4$ and $\Gamma_{\rm ph}/\Gamma_{\rm e} = 50$, respectively. On the other hand, we extend the system length along the z-axis to $512\Delta r$ in order to treat long wavelength for external plasma waves.

5.4.2 Steady State of the Plasma Environment

We performed ES simulations by using the numerical models for MEFISTO introduced in the previous section. In the present section, we first present results on plasma environments obtained as a steady state in the presence of the photoelectron emission, and also focus on the contribution of the puck-surface potential control and the current biasing to the surrounding plasma distribution. In order to obtain the steady state for the environment, we include no external plasma waves in the current computer experiments.

Electric potential

Figure 5.12 plots electric potentials of respective conducting elements of MEFISTO at a steady state with the puck-surface potential control, which is measured as a one-dimensional profile along the sensor axis. The positions of the conducting elements of MEFISTO are indicated in the figure. We choose the background plasma potential as a reference value. Here, we show three experimental results with different bias current magnitudes. The solid line represents the profile for a case of $I_{\rm bias} = -0.83 I_{\rm ph0}$, where $I_{\rm ph0}$ represents the photoemission current from one sensor element with the background plasma potential. For the sensor and the outer puck surface, we also plot their potentials in cases of $I_{\rm bias} = -0.41 I_{\rm ph0}$ and 0 by the dash-dotted and dashed lines, respectively.

The profile shows that respective conducting elements have correctly different potentials, which is a particular feature of MEFISTO. The boom has positive potential of several $k_{\rm B}T_{\rm ph}/e$, which is also the potential of the spacecraft body although not displayed in the figure. Because the boom and the spacecraft body are almost in a floating condition, the potential is a result of the balance between the dominant photoemission current and the small incident plasma currents. The potential of the inner puck surface is exactly $8k_{\rm B}T_{\rm ph}/e$ lower than the boom potential, which is intended in the computer experiments. The potentials of the sensor and the outer puck surface are clearly much influenced by the current bias magnitude. In the zero bias current case and still in the $I_{\rm bias} = -0.41 I_{\rm ph0}$ case, the sensor potential is positive for the same reason as for the spacecraft body. On the other hand, for $I_{\rm bias} = -0.83 I_{\rm ph0}$, the sensor potential is $0.052 k_{\rm B}T_{\rm ph}/e$. In the case, the bias current successfully draws the sensor potential close to the background plasma potential. The potential of the outer puck surface is $2k_{\rm B}T_{\rm ph}/e$ higher than the sensor potential for all cases as is intended.

Next, in order to exhibit an effect of the bias current, we plot the voltage–current

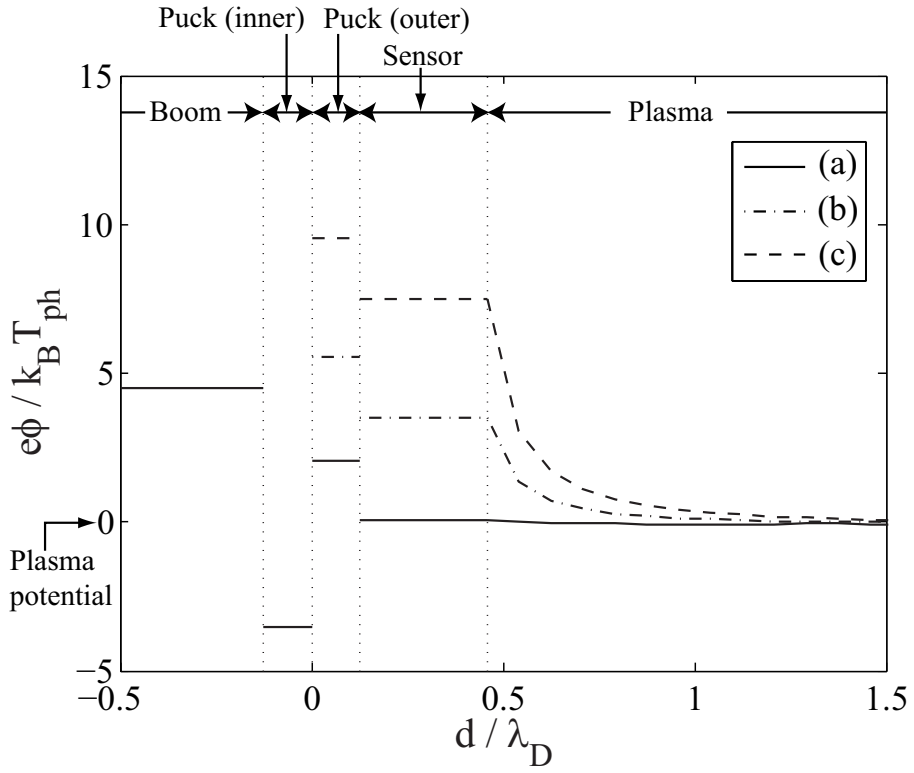

Figure 5.12: One-dimensional profile of the electric potential along the sensor axis. The horizontal axis represents the distance d from the interface between the inner and outer puck surfaces, which is normalized to the Debye length $\lambda_{\rm D}$ for the background plasma. The solid, dash-dotted, and dashed lines correspond to cases of (a) $I_{\rm bias} = -0.83 I_{\rm ph0}$, (b) $I_{\rm bias} = -0.41 I_{\rm ph0}$, and (c) $I_{\rm bias} = 0$, respectively.

characteristic curve in Figure 5.13, which is obtained in the computer experiment with the puck-surface potential control. From the figure, it is confirmed that the optimum magnitude for $I_{\rm bias}$ is $\sim -0.83 I_{\rm ph0}$ as is also shown in Figure 5.13. In order to form an equilibrium sensor potential at the background plasma potential, the sensor should satisfy a current balance condition given as

$$I_{\rm net} = I_{\rm ph0} + I_{\rm bias} - I_{\rm e0} + I_{\rm i0} = 0, \tag{5.17}$$

where $I_{\rm e0}$ and $I_{\rm i0}$ represent the currents of background plasma electrons and ions, respectively, when the sensor has the plasma potential. From Eq. (5.17), we calculated the optimum bias current analytically as

$$\begin{aligned} I_{\rm bias} &= -I_{\rm ph0} + I_{\rm e0} - I_{\rm i0} \\ &= I_{\rm ph0}\left[-1 + \frac{S\Gamma_{\rm e}}{S_{\rm ph}\Gamma_{\rm ph}}\left(1 - \sqrt{\frac{m_{\rm e}T_{\rm i}}{m_{\rm i}T_{\rm e}}}\right)\right] \\ &\sim -0.81 I_{\rm ph0}. \end{aligned} \tag{5.18}$$

In calculating the last term, we used the present parameters $S\Gamma_{\rm e}/S_{\rm ph}\Gamma_{\rm ph} = 0.191$ and $\sqrt{(m_{\rm e}T_{\rm i}/m_{\rm i}T_{\rm e})} = 2.33 \times 10^{-2}$. In the present case, the order of the analytical value agrees

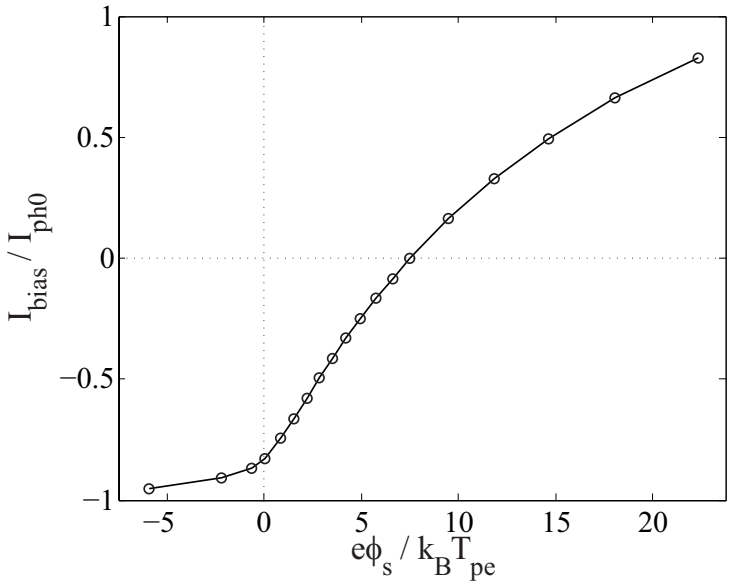

Figure 5.13: The voltage–current characteristic curve obtained in the computer simulations by changing the magnitude of the bias current. The zero potential corresponds to the background plasma potential.

with that of the numerical result. The small difference between the numerical and analytical results may be due to the presence of other conducting bodies near the sensor. Generally, in the presence of multiple conducting bodies emitting photoelectrons, the simple analytical expression arises some error because the body coupling through the emitted photoelectron currents is not taken into consideration in the theoretical estimation.

The voltage–current characteristic shown in Figure 5.13 can be understood in the analogy with an emissive (electron-emitting) probe, which is a sort of the Langmuir probes and used for a simple measurement of the plasma potential [*Hershkowitz*, 1989]. For a laboratory emissive probe, the probe body is heated to extract electrons from its surface, while the photoelectron emission plays an equivalent role in space. Another necessary condition for the emissive probe is that the temperature of emitted electrons should be much smaller than that of background electrons, which is also satisfied in the present photoemitting case. Thus, the present situation well reproduces a situation of the emissive probe. The emissive probe has advantage in precisely determining the plasma potential in comparison with a normal (non-electron-emitting) Langmuir probe.

Neglecting a space-charge effect, the photoelectron current $I_{\rm ph}$ can be written as

$$I_{\rm ph}(\phi_{\rm s}) = \begin{cases} I_{\rm ph0}\, g(\phi_{\rm s}) \exp\left(\dfrac{-e\phi_{\rm s}}{2k_{\rm B}T_{\rm ph}}\right) & \text{for } \phi_{\rm s} \geq 0, \\ I_{\rm ph0} & \text{for } \phi_{\rm s} \leq 0, \end{cases} \tag{5.19}$$

where the function $g(\phi_{\rm s})$ accounts for orbital momentum and depends on the dimensions of the photoelectron sheath [*Smith et al.*, 1979]. In the same manner, the collected

background electron current is given as

$$I_{\mathrm{e}}(\phi_{\mathrm{s}}) = \begin{cases} I_{\mathrm{e0}}\, g(\phi_{\mathrm{s}}) & \text{for } \phi_{\mathrm{s}} \geq 0, \\ I_{\mathrm{e0}} \exp\left(\dfrac{e\phi_{\mathrm{s}}}{k_{\mathrm{B}} T_{\mathrm{e}}}\right) & \text{for } \phi_{\mathrm{s}} \leq 0. \end{cases} \tag{5.20}$$

Since the collected ion saturation current is much smaller than the photoelectron current, the contribution of the ion current is usually neglected for the emissive probe unlike the normal Langmuir probe.

By taking the present parameter settings into consideration, the above emitted and collected currents form the total voltage–current relation shown in Figure 5.14(a), where we assume that $g(\phi_{\mathrm{s}}) \approx \sqrt{1 + e\phi_{\mathrm{s}}/k_{\mathrm{B}}T_{\mathrm{ph,e}}}$. The resultant I_{bias} curve indicates that the characteristic curve of the photoelectron current mostly determines the behavior of I_{bias} resulting from $I_{\mathrm{ph0}} \gg I_{\mathrm{e0}}$. Then, an inflection of the photoelectron current curve as ϕ_{s} passes through the plasma potential is effectively used for the determination of the plasma potential. It has been reported that the inflection in the total current is actually observed within a sensor potential range $0 - \phi_{\mathrm{ph}}$ [*Lieberman and Lichtenberg*, 1994], where ϕ_{ph} represents the kinetic energy of a photoelectron. This enables us to measure the plasma potential to an accuracy of the order of ϕ_{ph}.

Although the inflection of the curve is also seen in the numerical result shown in Figure 5.13, the present numerical result shows more moderate inflection than that shown in Figure 5.14(a). Furthermore, the numerical and theoretical curves show much different behavior in a range of the high sensor potential. This may be caused in part by the photoelectron current coupling among the sensor, the puck, and the boom. To see this effect, we consider the external current I_{ext}, which is generated by photoelectrons emitted from conducting bodies except the sensor and flowing into the sensor element. For simplicity, we use the same formulation as the background plasma electrons for I_{ext}, i.e., a formula obtained by replacing the subscript "e" in Eq. (5.20) by "ext". We here use $\phi_{\mathrm{ext}} = \phi_{\mathrm{ph}}$ for simplicity. On the other hand, I_{ext0} is practically difficult to estimate with an analytical approach, because the complex configuration of conducting elements directly influences it. As one example, we plot theoretical curves for $I_{\mathrm{ext0}} = (1/6)I_{\mathrm{ph0}}$ in Figure 5.14(b). It is seen that I_{ext} can moderate the inflection near $\phi_{\mathrm{s}} = 0$ and the gradient for $\phi_{\mathrm{s}} > 0$ of the curve, which is consistent with the tendency in the numerical result.

Even when we introduce the contribution of I_{ext}, the floating potential (i.e., the potential at which $I_{\mathrm{bias}} = 0$) read from the theoretical curve is smaller than that of the numerical result. This might be firstly caused by the erroneous assumption for the magnitude of I_{ext0}. Another plausible factor for the difference is the inappropriate formulation for I_{ph} given by Eq. (5.19). Eq. (5.19) indicates that I_{ph} decreases exponentially with an increasing sensor potential, which indicates most of emitted photoelectrons are trapped by and cannot escape from the positively charged sensor. However, some fraction of emit-

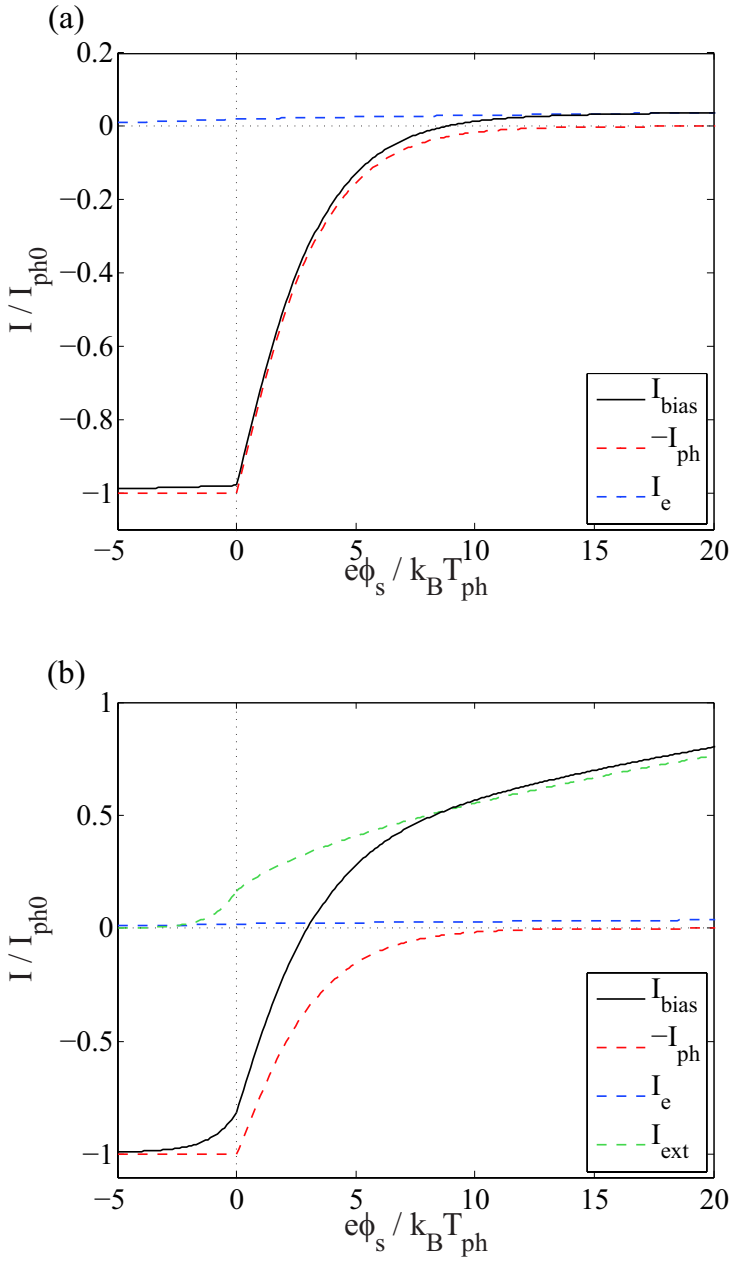

Figure 5.14: The voltage–current characteristic curves obtained theoretically. (a) We only consider the contribution of the photoelectron current $I_{\rm ph}$ and the background electron current $I_{\rm e}$. (b) We add the contribution of $I_{\rm ext}$, which is generated by photoelectrons emitted from conducting bodies except the sensor and flowing into the sensor element. We use $\phi_{\rm ext} = \phi_{\rm ph}$ and $I_{\rm ext0} = (1/6)I_{\rm ph0}$ for the plot.

ted photoelectrons should be constantly collected by the outer-puck surface, because the outer-puck surface always has a higher potential than the sensor potential. Since photoelectrons collected by the outer-puck surface are effectively counted as being emitted from the sensor, $I_{\rm ph}$ cannot become zero for a considerably high sensor potential. This effect is not considered in Eq. (5.19). Analytical evaluation of the above factors is often intractable for the situations of the complex sensor and spacecraft system. Therefore,

the quantitative investigation including the complicating factors should be conducted by using numerical methods as the present approach.

In this section, we focused on the steady state of the electric potential on the conducting elements of MEFISTO. Overall, it is confirmed through the analysis that the newly introduced numerical models can change the potential distribution on MEFISTO as we intended.

Photoelectron distribution

Our next interest is on the photoelectron distribution around the sensor and the spacecraft. Figure 5.15 shows contour maps of electron density (including photo- and background electrons) at the steady state in three cases (a) PC: on, BC: on, (b) PC: off, BC: on, and (c) PC: on, BC: off. The figures represent density profiles focused on the upper half of MEFISTO measured on the x–z plane that cuts the center of the spacecraft.

We confirmed that electron dense regions basically locate on the right side of each conducting body, which is obvious because photoelectrons are emitted rightward ($+x$ direction) from the sunlit surfaces. The distribution of the photoelectron clouds, however, is much different between the cases, particularly in the vicinity of the sensor and the puck surfaces. In comparison between cases (a) and (b), we can see effects of the puck-surface potential control on the electron densities around the outer and inner puck surfaces. In case (a) the photoelectron cloud is created mainly on the outer puck surface, while in case (b) the cloud shifts its position onto the inner puck surface. As a result, the cloud on the puck coalesces with that surrounding the boom in case (b). Next, in comparison between cases (a) and (c), an effect of the current biasing is also remarkable in the density profile in the vicinity of the outer puck surface and the sensor. The electron density is clearly reduced by the current biasing. The difference between the three cases is also seen in the electron density around the boom. For cases (a) and (c), the electron density evidently decreases being close to the puck. This is understood as an effect of the negatively biased potential of the inner puck with respect to the boom. On the other hand, in case (b), the electron density around the boom becomes higher as being close to the puck, which may be due to photoelectrons coming from the inner puck surface.

Figure 5.16 shows the flow of photoelectrons around the upper half of MEFISTO and the spacecraft body at the steady state of the environment. The vector plots show the local photoelectron flux, i.e., $J_{\mathrm{ph}}/(-e)$, where J_{ph} is the photoelectron current density, and the contour map shows the distribution of the electric potential. The profiles of the photoelectron flow show much different signatures around the sensor and the puck between the three cases, while no substantial difference near the spacecraft body.

Around the puck surface in case (a), the photoelectron flow clearly changes its direction from downward to upward at $z/\lambda_{\mathrm{D}} = 1.7$ which approximately corresponds to the

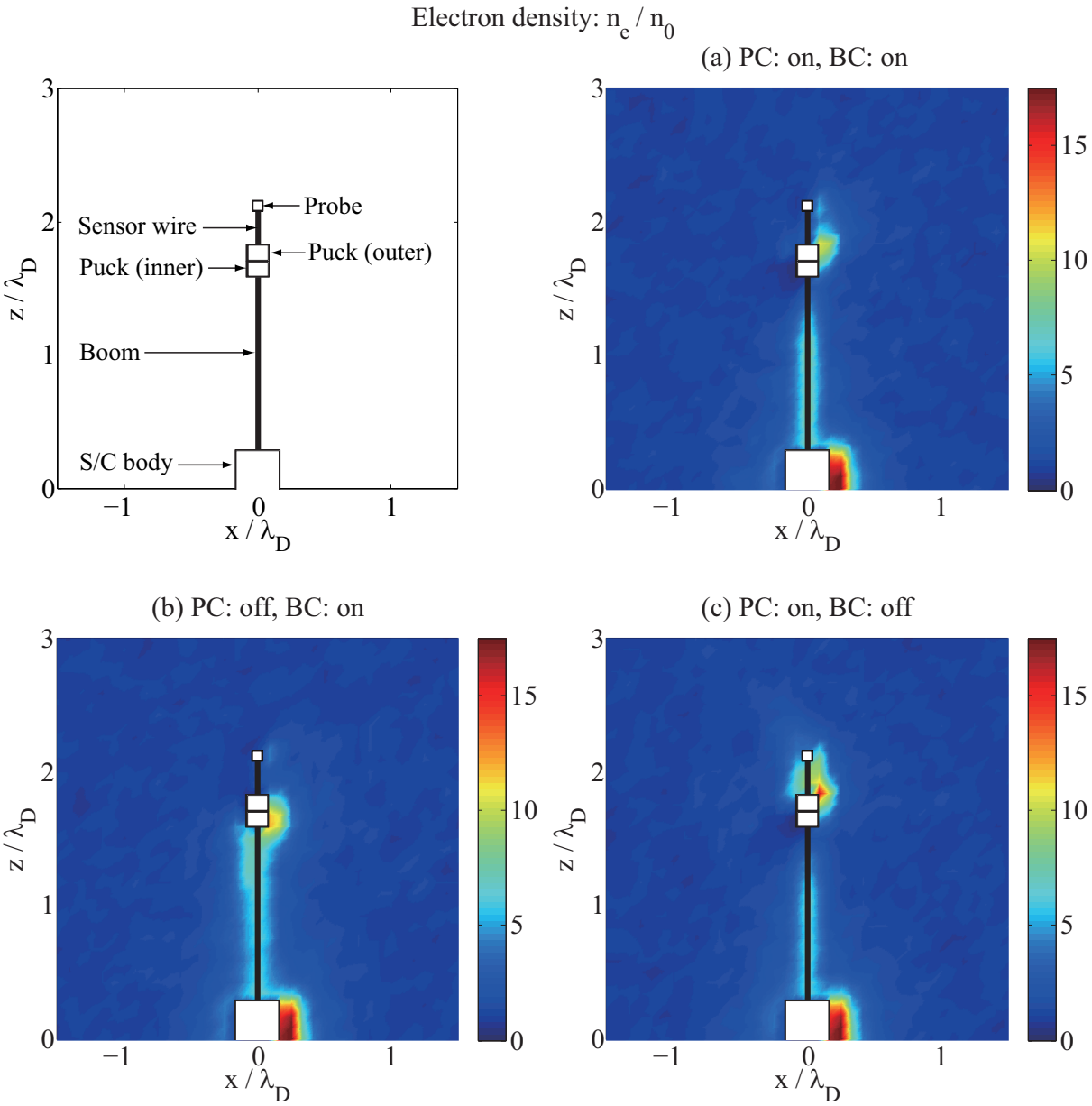

Figure 5.15: Two-dimensional profiles of the electron density on x–z plane that includes the MEFISTO antenna and cuts the center of the spacecraft. The upper-right, lower-left, and lower-right panels correspond to cases of (a) PC: on, BC: on, (b) PC: off, BC: on, and (c) PC: on, BC: off, respectively.

z-coordinate of the interface between the inner and outer puck surfaces. From the background potential profile, it is seen that photoelectrons accelerated by an intense electric field (potential difference) at the interface create the flow pointing upward even around the sensor. Meanwhile, some portion of photoelectrons emitted from the inner puck is attracted to the high potential region created by the boom conductor. As a result, the photoelectron flow is separated above and below the interface between the outer and inner puck surfaces. We can also see that photoelectron cloud observed in Figure 5.15

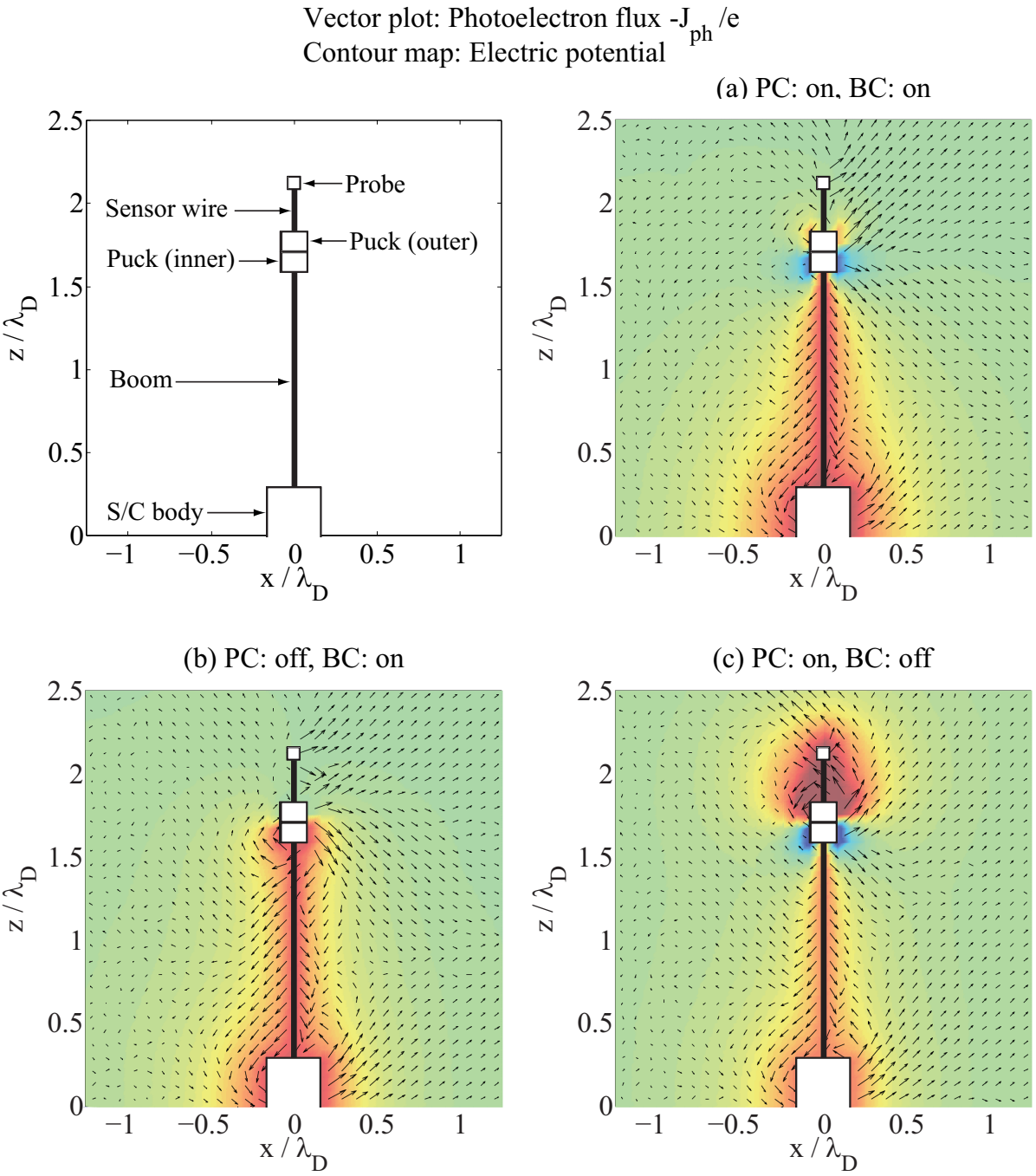

Figure 5.16: Vector plots of the photoelectron flux on x–z plane that cuts the center of the spacecraft. Background contour maps show the electric potential profiles. The upper-right, lower-left, and lower-right panels correspond to cases (a) PC: on, BC: on, (b) PC: off, BC: on, and (c) PC: on, BC: off, respectively.

corresponds to the positive potential region created around the surface of the outer puck.

For case (b), photoelectrons should be accelerated downward at the interface between the inner and outer puck surfaces. Further, a part of the accelerated photoelectrons appears to be attracted by the positively charged boom conductor. Thus, a substantial

amount of photoelectrons emitted from the puck surface flows onto the boom conductor, which leads to the coalesced photoelectron cloud observed in Figure 5.15.

Finally, the prominent feature seen in case (c) is a considerably high potential region around the outer puck surface and the sensor. This region attracts photoelectrons emitted from the inner puck surfaces as well as holding photoelectrons emitted from the sensor and the outer puck themselves. It follows that a large photoelectron cloud is created around the sensor in compared with cases (a) and (b), as seen in Figure 5.15.

In summary, the puck-surface potential control can inhibit the mixture of photoelectrons emitted from the sensor and the outer puck surface with photoelectrons emitted from the inner puck surface, boom, and spacecraft body, particularly in a case of combined use with the current biasing. Since the sensor and the outer puck can be thought as of one sensing element, the result suggests that the sensor–spacecraft (or sensor–boom) electric coupling through the photoelectron current can be reduced by the potential control. This function will be more important in a situation that the sensor is directed sunward, because it is believed that an erroneous electric field measurement in the situation is mainly caused by an asymmetric condition of the photoemission around the spacecraft surface and the sensor–spacecraft electric coupling through the photoelectrons [*Pedersen et al.*, 1998].

5.4.3 Wave Receiving Characteristics of MEFISTO

Electric properties of antennas based on the hockey puck principle have been numerically studied in a few previous works, e.g., *Béghin et al.* [2005] for CLUSTER's electric antennas and *Olson*, [2006] for MEFISTO. In the works, however, effects of photoelectrons and the distinctive functions as the puck-surface potential control and the current biasing have been completely neglected in the analyses. In the present section, we examine the effective length and the antenna impedance as receiving characteristics of MEFISTO fully including the above complicating factors.

Effective length

As was performed in Section 5.2, we setup the Langmuir waves propagating along z-axis in the computational space and receive them numerically by MEFISTO. In the current analysis, we set the wavelength $\lambda = 512\Delta r \sim 9.85 L_{\mathrm{a}}$. In the present section, we employ an open-circuit condition for the antenna input points in order to focus solely on the effective length. We performed three computer experiments for the cases (a) PC: on, BC: on, (b) PC: off, BC: on, and (c) PC: on, BC: off. For the current biasing, we use the current magnitude, which has been found in the preceding section to realize an optimal sensor potential close to the background plasma potential.

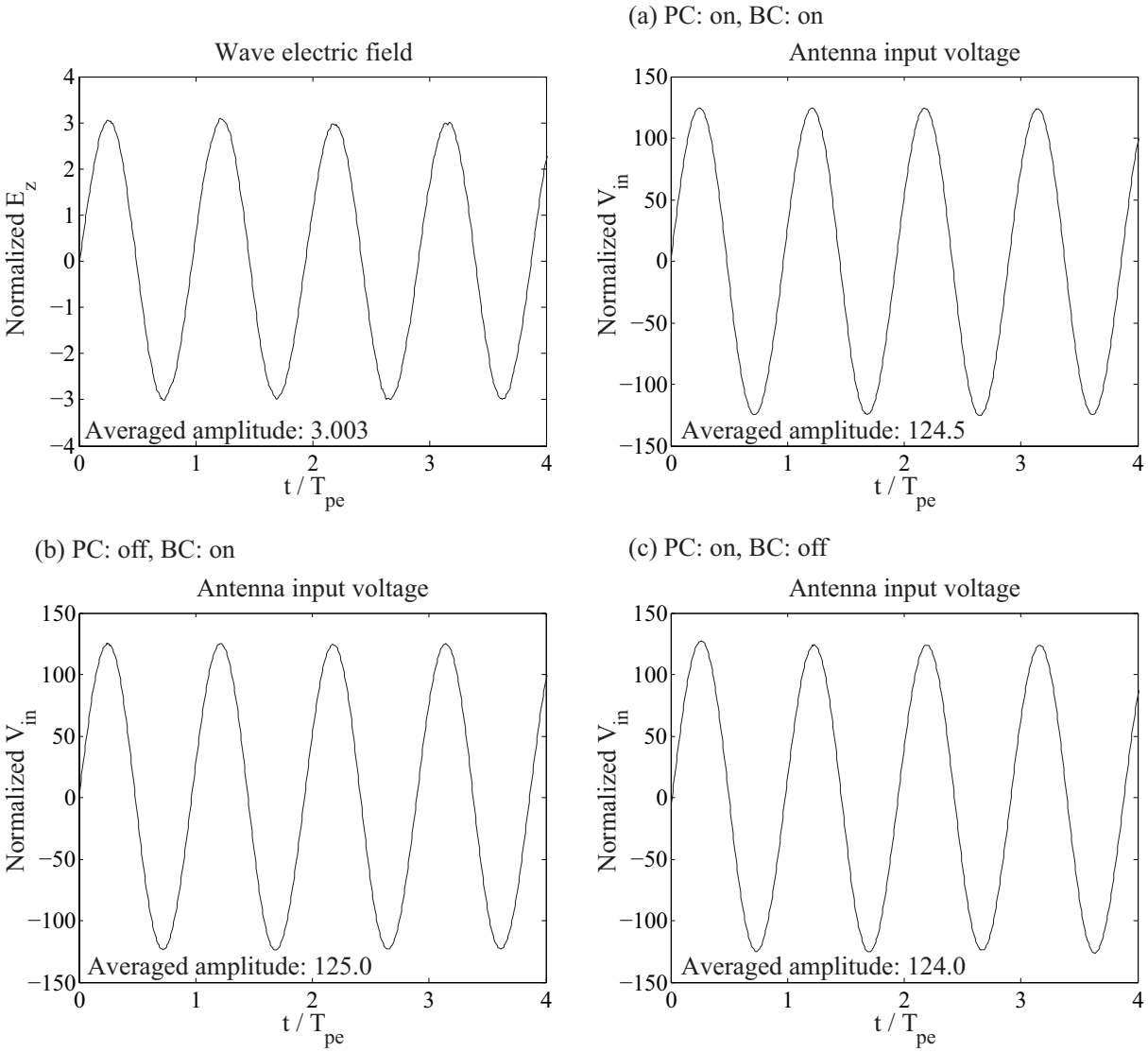

Figure 5.17: (Upper-left) Raw electric field of the Langmuir wave, which is measured at a certain locus in the background plasma and on the wavefront cutting the center of the spacecraft. (Upper-right, lower-left, and lower-right) Waveforms observed by MEFISTO as the input voltages in cases of (a) PC: on, BC: on, (b) PC: off, BC: on, and (c) PC: on, BC: off, respectively.

Figure 5.17 shows waveforms of the wave electric field and the antenna input voltage (the potential difference between the two sensor elements) observed in the Langmuir wave reception. It should be noted that since the input voltage should be zero if any external waves are not present, the plotted waveforms in the figure represent only oscillating components purely caused by the incident plasma waves. The results clearly show that the observed waveforms of the antenna input voltages are almost the same in all cases, which indicates the effective length is hardly influenced by the puck surface potential control and the current biasing. From the comparison of the amplitude of $V_{\rm in}$ with $E_{\rm wave}$, we obtain the effective length $L_{\rm eff} \sim 0.80 L_{\rm a}$ for all cases. The resultant value is smaller than

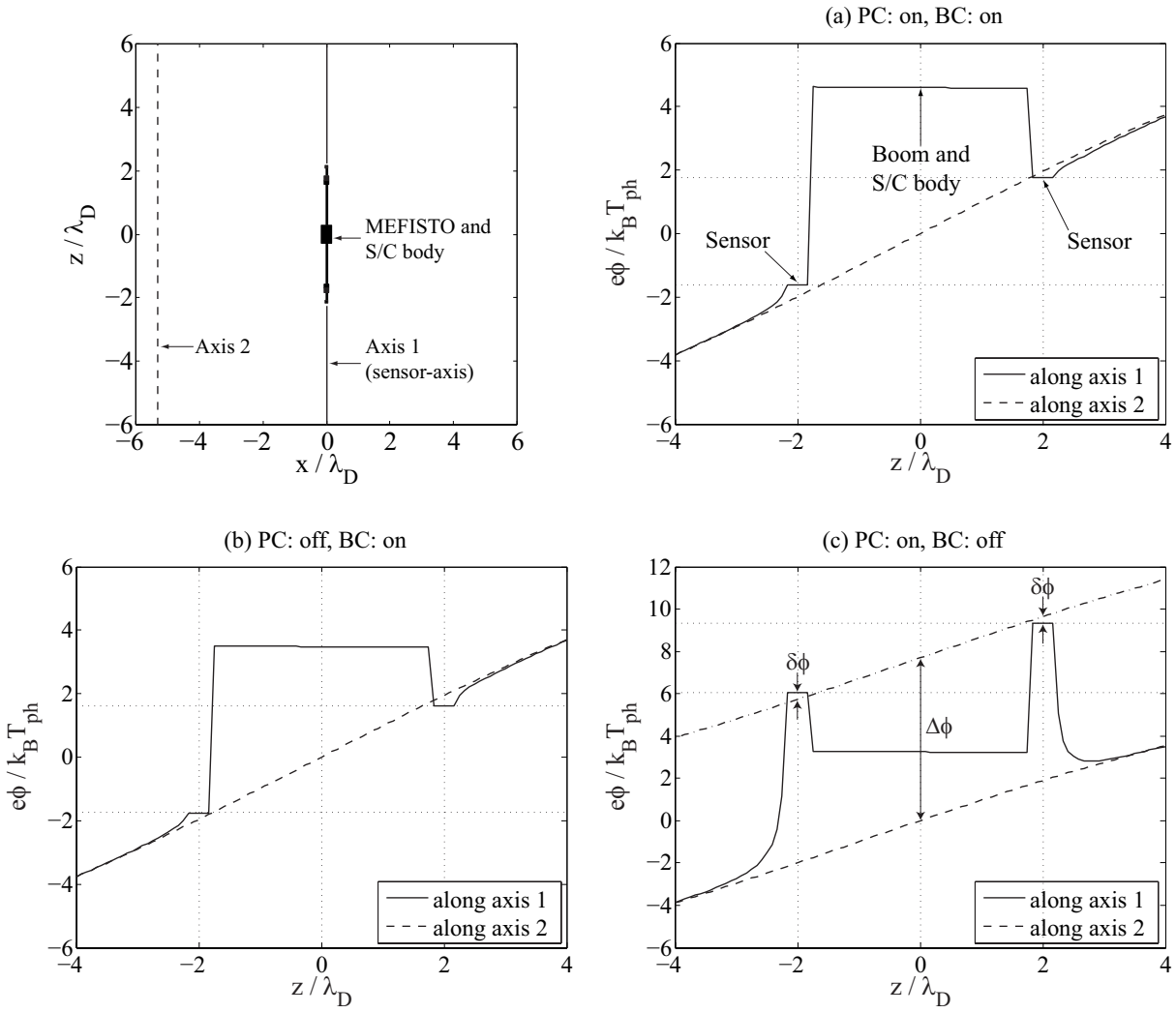

Figure 5.18: Snap shots of one-dimensional profiles of electric potential measured along the sensor axis (shown in the solid line), and in the background plasma (shown in the dashed line). Note that the profiles include only potentials of the sensors at both ends and the boom (and the spacecraft), and the puck surface potentials are not displayed.

the separation between two midpoints of the sensor elements, i.e., $0.92L_{\rm a}$ for the present numerical model. This decrement may be caused by the short-circuit effect discussed in Section 5.2.

Although the resulting effective lengths are almost the same in the three cases, the potential profiles around MEFISTO are expected to be different among these cases. In Figure 5.18, we show snap shots of one-dimensional potential profiles in the vicinity of MEFISTO plotted in the same way as Figure 5.7. Note that the profiles include only potentials of the sensors at both ends and the boom (and the spacecraft), and the puck surface potentials are not displayed. In the figure, the cases (a) and (b) show the similar signature. This immediately indicates that the puck surface potential control has small

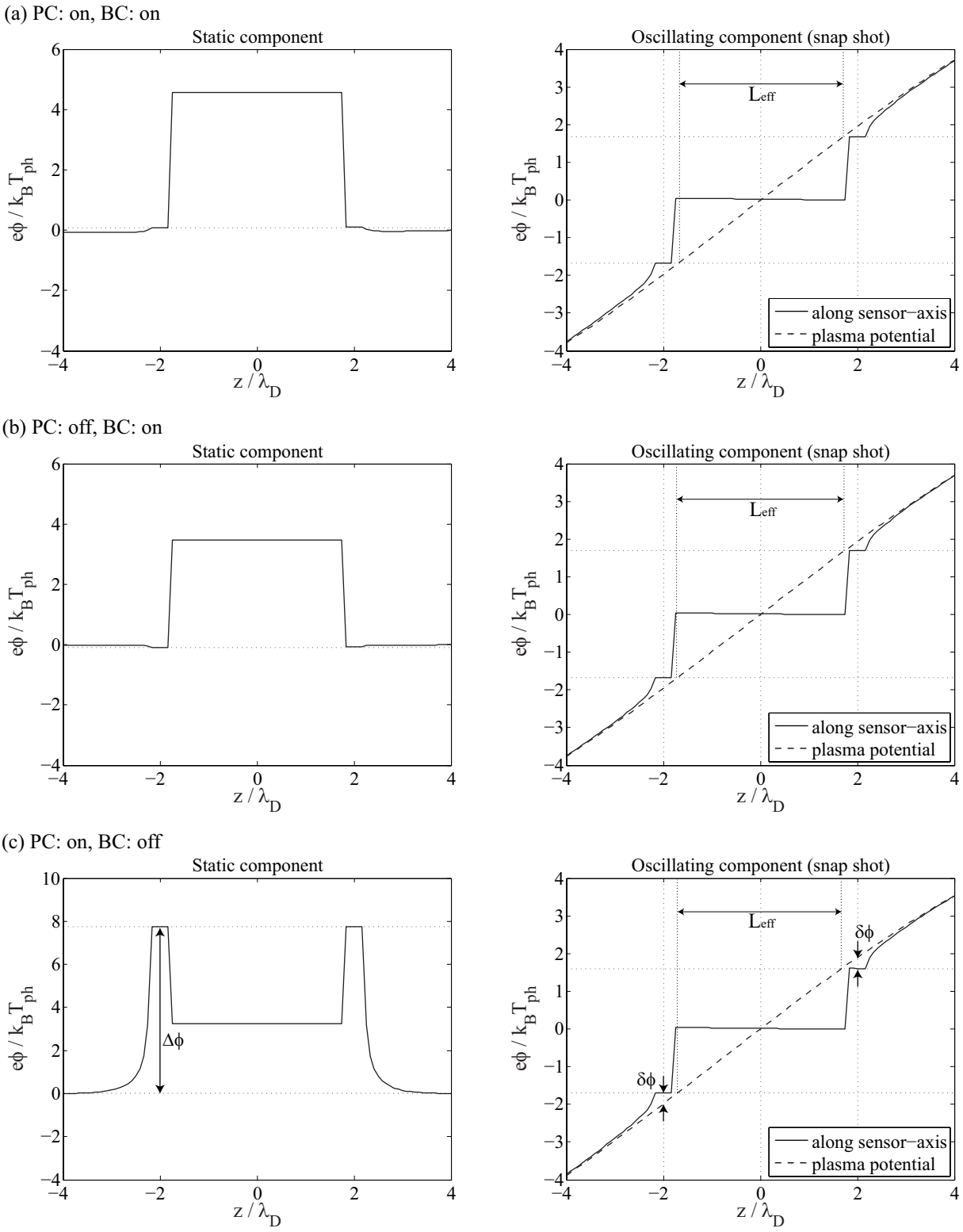

Figure 5.19: Static and oscillating components of electric potential structure measured along the sensor axis (shown in the solid line), and in the background plasma (shown in the dashed line).

influence on the potential values of the sensor elements. On the other hand, since the current biasing is disabled in the case (c), sensor potentials at both sides are positively biased from their local plasma potentials due to the photoemission. What is interesting in the profile is that the extent of the potential increments from their local plasma potentials is different between the two sensor elements. As shown in the profile, the potential increment is $2\delta\phi$ larger for the left sensor element than for the right. Here $\delta\phi$ is the potential difference between a local potential value for the dash-dotted line defined in the figure and each sensor potential.

The snap shots shown in Figure 5.18 include both static and oscillating components of the potential structure. Since the external electric field to be received by MEFISTO is a wave (oscillating) field in the present situation, the results of $L_{\rm eff}$ can be thought as being associated with only the oscillating component of the potential structure. In order to understand the potential profiles more clearly, we plot the static and oscillating components of the potential structure independently in Figure 5.19. To extract the static components from the total potential profile, we took temporal averages of the potential profiles over one period of the Langmuir wave. The snap shots of the oscillating components are then obtained by subtracting the static components from the total potential profiles. Figure 5.19 indicates that the difference of the total potential profiles observed in Figure 5.18 entirely comes from the static components, while the oscillating components exhibit little difference between the three cases. For the oscillating components in all cases, the sensor potentials represent the background plasma potential of positions nearer the spacecraft than their own midpoints. This tendency is basically the same as that seen for the linear-probe antenna described in Section 5.2. As a result, the resultant effective lengths are identical for all cases. We can also understand in Figure 5.19(c) that $\delta\phi$ observed in Figure 5.18(c) comes from the oscillating component, while $\Delta\phi$ from the static component. We finally note that the static potentials for the boom conductor are different between the three cases and the highest for the case (a). This is caused by the negative biasing of the inner puck surface potential and the sensor potential with respect to the boom potential, both of which lead to the accumulation of the positive charge at the boom. The different static potentials for the boom conductor, however, have little influence on the resultant effective length of the sensor.

Antenna impedance

Next, we focus on the MEFISTO antenna impedance. For this aim, we performed computer experiments including a finite load impedance, the modeling of which has been introduced in Section 5.3.4. When the load impedance $Z_{\rm L}$ is connected at the antenna input, the relation between the output voltage $V_{\rm out}$ and $E_{\rm wave}$ is given by Eq. (1.2). On the other hand, we have already obtained the open-circuit voltages in the preceding sec-

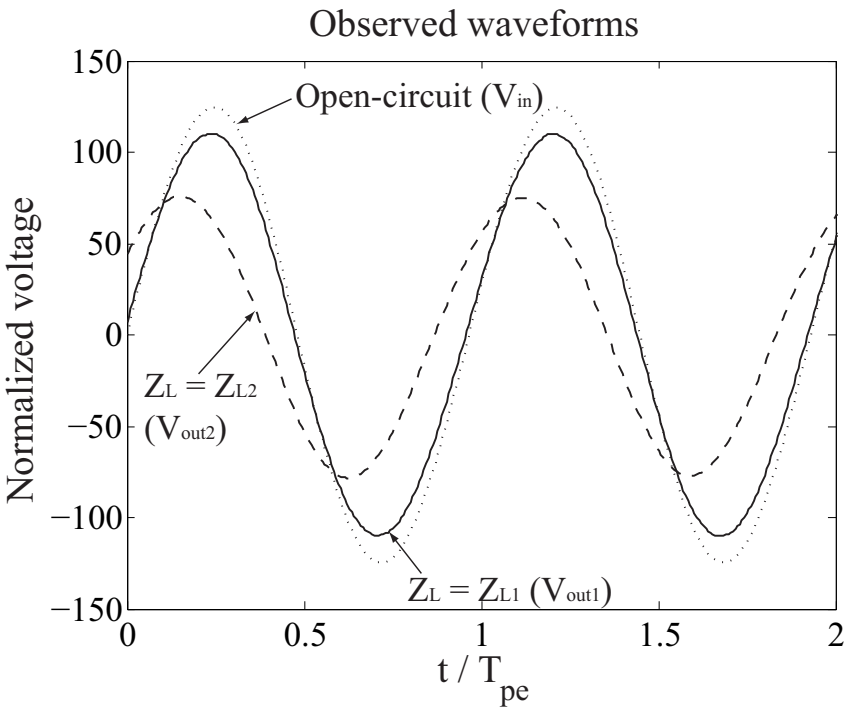

Figure 5.20: Waveforms of observed voltage signals by MEFISTO with finite and infinite load impedances in the case of (a) PC: on, BC: on. The solid, dashed, and dotted lines correspond to cases of $Z_{\rm L} = Z_{\rm L1}$, $Z_{\rm L2}$, and open-circuit conditions, respectively (also see text for the details of $Z_{\rm L1}$ and $Z_{\rm L2}$).

tion, which are given by $V_{\rm in} = L_{\rm eff} E_{\rm wave}$. By combining it with Eq. (1.2), the antenna impedance $Z_{\rm a}$ is given by

$$Z_{\rm a} = \left(\frac{\tilde{V}_{\rm in}}{\tilde{V}_{\rm out}} - 1 \right) Z_{\rm L} = \left(\frac{|V_{\rm in}|}{|V_{\rm out}|} e^{-j\theta_{\rm s}} - 1 \right) Z_{\rm L}, \tag{5.21}$$

where $\tilde{V}_{\rm in}$ and $\tilde{V}_{\rm out}$ give the phasor representations of the signals $V_{\rm in}$ and $V_{\rm out}$, and $\theta_{\rm s}$ represents the phase shift of $V_{\rm out}$ with respect to $V_{\rm in}$. Namely, we can obtain $Z_{\rm a}$ by comparing waveforms observed in cases of the open-circuit and finite load impedance conditions.

As briefly introduced in Section 5.3.4, in actual missions $Z_{\rm L}$ is effectively composed of the resistance $R_{\rm L} \sim 10^1\,{\rm M}\Omega$ and the capacitance $C_{\rm L} \sim 10^0\,{\rm pF}$ connected in parallel. In the frequency range of $\omega = 10^1$–$10^2\,{\rm kHz}$ in which electron plasma waves are frequently observed, the above setting gives $|1/\omega R_{\rm L} C_{\rm L}| \sim 10^{-1}$–$10^0$. In the computer experiments, on the other hand, the free-space capacitance $C_{\rm a}$ of the numerical antenna model is much larger than the actual MEFISTO antenna due to some unrealistic settings of its dimensions, and $|1/\omega_{\rm pe} C_{\rm a}|$ is about $10^4\,\Omega$, where $\omega_{\rm pe}$ is the electron plasma frequency. In the present analysis, as a first setting of parameters, we choose values of the load impedance $Z_{\rm L1}$ composed of $R_{\rm L} = 5 \times 10^4\,\Omega$ and $|1/\omega_{\rm pe} C_{\rm L}| = 5 \times 10^4\,\Omega$ connected in parallel. In addition to the above setting, in order to exhibit the attenuation due to

Table 5.1: Numerical results of the MEFISTO antenna impedance in cases of (a) PC: on, BC: on, (b) PC: off, BC: on, and (c) PC: on, BC: off. Based on the lessons obtained in Chapter 4, we assume a circuit form consisting of a resistance R and a capacitance C connected in parallel, i.e., $Z_{\rm a} = R\|(1/j\omega_{\rm L}C)$. We then listed the calculated values for R and $1/\omega_{\rm L}C$.

Case	R (Ω)	$1/\omega_{\rm L}C$ (Ω)
(a) PC: on, BC: on	1.66×10^4	5.40×10^3
(b) PC: off, BC: on	1.56×10^4	5.44×10^3
(c) PC: on, BC: off	1.62×10^4	5.38×10^3

the finite load impedance more clearly, we also perform computer experiments using $Z_{\rm L2} = R_{\rm L} = 5 \times 10^3\,\Omega$ (pure resistance).

By using the above two settings of $Z_{\rm L}$, we performed the computer experiments of the Langmuir wave reception for the cases (a), (b), and (c) which have been analyzed also in the previous sections. We plot an observed waveform of the antenna input voltage for the case (a) in Figure 5.20. The received waveforms with the finite load impedances (the solid and dashed lines) clearly show the attenuation of the signal amplitude compared with that in the open-circuit condition. Moreover, for the dashed line, we can also confirm the phase shift of the received waveform. The numerical results for the cases (b) and (c) are almost the same as the case (a), although their waveforms are not displayed. The result suggests that the puck surface potential control and the current biasing have a small effect also on the antenna impedance as well as the effective length.

From the resultant waveforms, we obtained the antenna impedance using Eq. (5.21) at the Langmuir wave frequency $\omega_{\rm L}$. In Table 5.1, we list the impedance results for the cases (a)–(c) calculated by comparing the waveforms in the $Z_{\rm L} = Z_{\rm L2}$ and open-circuit conditions.

The numerical results show only slight difference between the three cases, i.e., the maximum difference is $\sim 6\,\%$ for R and $\sim 1\,\%$ for $1/\omega_{\rm L}C$. It should be noted that we can calculate the impedance also using the waveforms in the $Z_{\rm L} = Z_{\rm L1}$ and open-circuit conditions, and the calculated impedance value should coincide with the values listed in Table 5.1. For example, in the case (a), the impedance value calculated using the waveform in $Z_{\rm L} = Z_{\rm L1}$ instead of that in $Z_{\rm L} = Z_{\rm L2}$ is $R\|(1/j\omega_{\rm L}C) = (1.9 \times 10^4\,\Omega)\|(-5.4 \times 10^3 j\,\Omega)$. From the fact that a certain level ($\sim 10\,\%$) of the difference is seen particularly in the R value compared with the value listed in Table 5.1, it is considered that the error level of $\sim 10\,\%$ might be included in the resultant values listed in Table 5.1. This indicates the difficulty to conclude that the slight difference observed between the cases (a)–(c) is surely caused by effects of the potential control for the puck surfaces or the current biasing. In fact, the results suggest that both puck surface potential control and current biasing do not have, at least, large influence on the antenna impedance.

Recalling the electron density profile around the sensor element shown in Figure 5.15, the puck surface potential control mainly influences the electron density in the vicinity of the puck surface and a region that is slightly apart from the sensor position. On the other hand, the antenna conductance (and the dynamic resistance R_{L} as its inverse) strongly depends on electrons directly contacting to the sensor surface as discussed in the preceding chapter. Therefore, an effect of the puck surface potential control may be too small to observe as the change of the antenna impedance for the present parameter setting of the puck surface potential.

Meanwhile, the result that the current biasing also has little effect on the impedance is more puzzling, which is inconsistent with a theoretical prediction as discussed below. By considering only contribution of the dominant photoelectron current, the analytical expression for the dynamic resistance R_{L} is given as

$$R_{\mathrm{L}} = \left[\frac{S_{\mathrm{ph}} e^2 \Gamma_{\mathrm{ph}}}{k_{\mathrm{B}} T_{\mathrm{ph}}} \exp\left(-\frac{\phi_{\mathrm{s}}}{\phi_{\mathrm{ph}}} \right) \right]^{-1}, \tag{5.22}$$

as discussed in Chapter 4. The expression indicates that the resistance has exponential dependence with respect to the sensor potential, which implies that the antenna impedance should be sensitive to the current biasing operation. A reason for the disagreement between the numerical result and the theoretical prediction can be explained by referring the voltage–current characteristic curves shown in Figures 5.13 and 5.14. In principle, the antenna conductance $1/R_{\mathrm{L}}$ corresponds to the local gradient of the voltage–current curve at a given DC sensor potential. For the theoretical curve shown in Figure 5.14(a), the curve evidently has higher gradient at $\phi_{\mathrm{s}} = 0$ than at the floating potential $\phi_{\mathrm{s}} \sim 9 k_{\mathrm{B}} T_{\mathrm{ph}}/e$ corresponding to $I_{\mathrm{bias}} = 0$. This trend of the dynamic resistance with respect to ϕ_{s} is consistent with a result led by Eq. (5.22). However, in the actual voltage–current curve shown in Figure 5.13, its inflection at $\phi_{\mathrm{s}} = 0$ is moderated in comparison with that shown in Figure 5.14(a), which reduces the local gradient at $\phi_{\mathrm{s}} = 0$ to a value similar to the gradient at the floating potential. It follows that the resultant resistance values are almost the same for both cases of the sensor with the background plasma potential (BC: on) and the floating potential (BC: off).

5.5 Summary

This chapter presents a new technique for the direct analysis of the plasma-wave reception by the electric antenna and numerical modeling of a modern electric field instrument designed based on the hockey puck principle. The simulation technique of the plasma-wave reception enables us to reproduce more realistic situations of the plasma-wave observation with scientific spacecraft. Once the method is developed, the analysis on various types of

antennas becomes possible only by replacing the numerical model of the antenna placed in the center of the computational space.

As one of the antenna models for specific satellite missions, we have focused on MEFISTO, which is planned to be onboard BepiColombo/MMO to Mercury. Special attention has been paid for the modeling of the operational control of the puck surface as the photoelectron guard and the current biasing. Although these mechanisms are originally for optimal measurements of a DC electric field component, the close modeling of them is essential also for the analysis of the wave receiving characteristics of MEFISTO. The mechanisms are introduced as new treatments of the accumulated charge on the MEFISTO surfaces and the electrostatic component associated with the surface charge. We have derived necessary conditions for the surface charge by expanding the Capacity Matrix method. We have also presented the treatment of the finite load impedance on the assumption that the impedance is composed of a resistance and a capacitance connected in parallel, which is a typical composition used for plasma wave instruments.

The introduced models are validated by examining the steady state of the potential profile and the plasma environment. We confirm the achievement of the intended behavior of the puck surface potential control and the current biasing. It is also revealed that these mechanisms have a significant impact on the distribution of photoelectron clouds. The negatively charged guard electrode tends to reduce the electric coupling between the sensor and the boom through the photoelectron current. It is also found that the current biasing reduces the amount of photoelectrons surrounding the sensor parts.

Next, we have analyzed the wave receiving characteristics of MEFISTO. The result shows that the effective length of MEFISTO is hardly affected by the puck surface potential control and the current biasing. The analysis of the antenna impedance also shows a considerably small effect of the puck surface potential control and the current biasing. Particularly, almost the same antenna impedance obtained in the two cases of the sensor with the background plasma potential (BC: on) and the floating potential (BC: off) is not consistent with a theoretical prediction. For the inconsistency, a numerical result of a voltage–current characteristic curve suggests that the moderated inflection of the curve may reduce the gradient of the curve at the plasma potential, which also reduces the antenna conductance to the same level as that observed at the floating potential.

The similar impedance values for the cases with and without the current biasing are explained by the deformation of the voltage–current curve due to the photoelectron current coupling. This implies the possibility that the coupling can influence the antenna impedance, even though its effect is decreased by the function of the guard electrode. To mitigate the influence of the photoelectron coupling more effectively, we should evaluate more optimal puck surface potentials by further computer experiments in the future.

In actual operations in magnetospheric missions, the sensor is expected to operate at a

slightly higher potential than the background plasma potential. Further, the moderation of inflection of the voltage–current curve should be smaller than the present numerical analysis, because the energy ratio of the photoelectrons to the background plasma electrons is small in the present numerical analysis compared with realistic parameters. In such a situation, the antenna impedance can have some dependence on the bias current magnitude. For more detailed understanding of the effect, further numerical analyses are necessary employing more realistic photoelectron parameters and various magnitude of the bias current, which is left as a future work.

Chapter 6

Concluding Remarks

6.1 Summary and Conclusions

In this thesis, we have made numerical investigations on the electric antenna characteristics in space plasma environment that is disturbed by interactions with the conducting bodies of an antenna and a spacecraft. For the numerical investigations, we have constructed a simulation code based on an electromagnetic Particle-In-Cell (EM-PIC) description as well as numerical models of the antenna and the spacecraft. After a confirmatory impedance analysis in a homogeneous plasma environment, we have introduced plasma-inhomogeneity effects such as the sheath formation and the photoelectron emission, which are inevitable factors when considering practical spacecraft environments. Particularly, in the last half of the thesis, we have concentrated our analysis on the effects of photoelectrons, the distribution of which is strongly influenced by the charging of the antenna and spacecraft bodies. Below, we give summaries of the present thesis.

In Chapter 1, we have introduced basic principles of plasma wave measurements, especially an electric field measurement using space-based electric antennas onboard scientific satellites. From the principles, we have clarified important antenna characteristics for plasma wave measurements: the impedance and the effective length. From the aspects of some limitations and difficulties inherent in theoretical and space-experimental approaches, we have discussed the significance of computer experiments for the antenna analysis in space plasmas.

In Chapter 2, we have described numerical techniques for the study of antenna–plasma interactions on a full EM basis. Previously, numerical treatments of perfect conducting bodies were mostly studied only for electrostatic PIC simulations, and the methodologies for including the conducting bodies in EM-PIC simulations were rarely discussed. For the adaptation of the conducting body treatments also to the present EM model, we have shown the importance of introducing inner-boundary treatments for the current density in addition to those for the charge density. Then, the charge density is computed by integrating the charge continuity equation using the above-obtained current density. These

treatments are necessary for accurate descriptions of the charge accumulation exactly on conducing surfaces. By combining the above treatments with other necessary treatments such as body-surface charge redistribution and modifications of longitudinal and transverse electric field components, we have successfully constructed a simulation code for the self-consistent analysis of antenna–plasma (and spacecraft–plasma) interactions including EM phenomena.

Chapter 3 is devoted partly to the demonstration of the antenna analysis by applying the constructed code to relatively simple plasma environments. As a basic impedance-analysis technique, we have introduced a delta-gap feeding technique assuming a transmitting antenna, which is used also in Chapter 4. We have firstly examined the dipole antenna impedance in an unmagnetized plasma completely excluding effects of the sheath formation and the photoelectron emission. The impedance resonance is correctly reproduced at the electron plasma frequency, which is a result of a strong antenna–plasma interaction through emanated antenna-field energy. As a next step, we have included contribution of an ion sheath created around the antenna in the impedance analysis. An electron density profile in the ion sheath, which is created associated with the antenna charging, has gradual variation in a spatial scale of a few Debye lengths. Although the sheath edge is not well defined because of the gradual density change, the sheath mainly contributes to the antenna reactance below the electron plasma frequency, the behavior of which can be modeled as a capacitance as was done in previous studies. Also, several differences from previous knowledge are found in the present numerical results. One is a non-triangular current distribution along the antenna observed at the impedance resonance frequency, which is one of plausible reasons for a disagreement of the resonance intensities observed between the numerical and theoretical results. The other is the capacitance of a thick sheath which is forcibly expanded by the DC potential biasing of the antenna. It is revealed that the capacitance cannot have a lower value than the free-space capacitance of the antenna itself.

In Chapter 4, we have investigated photoelectron effects on the antenna impedance. Assuming that the sun illuminates an antenna and a spacecraft body from the direction perpendicular to the antenna, we have injected electrons from the sunlit surfaces into a computational space, which simulated the photoelectron emission. As a result of the photoemission, a positive floating potential with the magnitude corresponding to a few times the photoelectron energy is obtained for the antenna, which is due to a sufficiently larger photoelectron flux than that of plasma electrons. As for the plasma environment, the formation of an electron-dense region is confirmed around the sunlit surfaces of the antenna and the spacecraft. Under the photoelectron environment, the antenna admittance (i.e., the inverse of antenna impedance) has an almost constant real part and a linearly increased imaginary part with the frequency, which suggests that the impedance

under the photoelectron environment is well modeled by an equivalent electric circuit consisting of a resistance and a capacitance connected in parallel. Further, it is found that the above resistance highly depends on the photoelectron flux, while the capacitance is almost independent of the flux. Analytical derivation of the dynamic resistance based on the Orbital-Motion-Limited theory shows a good agreement with the present numerical result for the antenna resistance. From this attempt, it is revealed that the impedance change under the photoelectron environment is caused by the conduction current induced by the actual motion of photoelectrons contacting with the antenna surfaces. On the other hand, the impedance resonance, which was observed in the analysis described in the previous chapter, is not observed for the present situation and plasma parameters. This is because the antenna dimensions are sufficiently smaller than the Debye length for the background plasma.

In Chapter 5, the receiving characteristics of an electric antenna are studied more directly using a newly introduced analysis technique. In the technique, we have set up wave fields propagating in a computational space and simulated a process of the wave reception by the antenna. By using the technique, we have examined the effective lengths of a dipole antenna and a probe-like antenna. For the probe-like antenna sensing wire elements are attached at both ends of a center boom conductor. The analysis correctly reproduces the reception of the Langmuir wave with much larger wavelength than the tip-to-tip antenna length, which is confirmed by the result that the obtained effective length coincides with the half of the physical antenna length for the dipole antenna. Meanwhile, for the probe-like antenna, the effective length becomes shorter than the physical separation between the centers of the two sensing elements. This effect comes from the distortion of equi-potential surfaces caused by the presence of the center boom conductor and the attraction of the sensor potential to the boom conductor potential.

Next, we have introduced numerical models of guard electrode and current biasing, which are planned to be installed in modern electric field instruments for future missions. By examining a static plasma environment using the introduced models, we have found that the guard electrode decreases the coupling of the sensor conductor with the boom or spacecraft bodies through the photoelectron conduction current. We have also confirmed that the bias current draws the sensor potential close to the background plasma potential. In comparison with their significant impacts on the static plasma environment, we have observed a relatively small effect of the guard electrode and the current biasing on sensor behavior for oscillating fields created by external plasma waves. This result is understood from the voltage–current characteristic curve of the sensor, the gradient of which indicates the inverse of the dynamic resistance of the sensor for the oscillating fields. Meanwhile, the observed voltage–current curve is considerably deformed by the effect of the photoelectron current coupling even though it is decreased by the operation of the guard electrode.

The result suggests the possibility that more optimal electrode potentials can minimize the photoelectron effect and modify the sensor characteristics even for the wave fields. This emphasizes the significance of further investigations of sensor characteristics when operating the guard electrode and the current biasing more optimally.

In conclusion, we have observed two classes of impedance change in plasma environment through the present computer experiments. The first class of the impedance change comes from an antenna–plasma interaction through field energy in the form of plasma waves (or oscillations). Then the impedance change is strongly associated with the properties of plasma waves and oscillations. The most noticeable example is the impedance resonance observed exactly at the frequency, at which the electron plasma (Langmuir) wave is allowed to propagate. The important feature of the impedance change is that it can be observed only when the antenna length is sufficiently longer than plasma characteristic lengths such as the Debye length as examined in the computer experiments in Chapter 3.

The second class of the impedance change is a result of the antenna near field acting more directly on plasma particles in the vicinity of the antenna. The motion of affected plasma particles forms the conduction current flowing into or out of the antenna conducting surface. In the aspect of an equivalent circuit for the antenna impedance, the effect of the conduction current can be modeled as a circuit path with a finite resistance connected in parallel to the antenna capacitance. This class of the impedance change is particularly prominent in the presence of photoelectrons contacting with the antenna surface as examined in Chapters 4 and 5, because the current created by the photoelectron motion can directly flow into and out of the surface. Meanwhile, the impedance change is not observed in an ion-sheathed situation as analyzed in Chapter 3. This is because the electron sparse region separates the antenna surface from the conducting background plasma.

As described above, we can evaluate the contribution of multiple mechanisms for impedance change simultaneously by performing the computer experiments. The present numerical approach also has feasibility of including complex antenna and spacecraft geometries. The advantage has been actually shown in the analysis of the effective length, in which it is revealed that the effective length is influenced by the presence of a supporting boom conductor. Thanks to these advantages, we believe that the present numerical method will become a standard approach for the quantitative evaluation of practical electric antenna characteristics in future satellite missions.

6.2 Suggestions for Future Works

For the further development of the present numerical tool, some issues should be considered in future works. One is the precise inclusion of the fine structures of an antenna and a spacecraft in the computer experiments. Since the spatial scale of the fine structure is too small to treat simultaneously with surrounding plasma environments in the present uniform grid system, the introduction of a locally refined mesh will be required for more quantitative evaluation of the antenna characteristics. The other is the introduction of non-conducting bodies such as dielectric materials. For an electric antenna, the dielectric material is used as an insulator of the antenna conductor from surrounding plasmas, which particularly influences DC and low-frequency behavior of the antenna.

Also for antenna characteristics in space plasma environment, there are some problems which should be considered in the future. In the present work, we have examined the receiving antenna characteristics only for plasma waves with sufficiently larger wavelength than the antenna length. However, electrostatic waves sometimes have considerably short wavelength, and it is reported that the antenna behavior for such waves deviates from that in the long-wavelength case. We should perform computer experiments for more reliable plasma wave measurements also in such short-wavelength situations. It is also necessary to study interactions between a high-voltage antenna and surrounding plasmas, because it is planned that such an antenna is applied to a whistler wave transmitter to control the precipitation of radiation belt electrons [*Inan et al.*, 2003]. When the high voltage is applied to the antenna, the antenna behavior may deviate strongly from previous knowledge that is mostly based on a linear theory for the plasma response to the antenna near field. The present EM-PIC approach can become a powerful tool for the analysis of the non-linear plasma response to the high-voltage antenna. We hope that the further investigations using the present numerical method will contribute to a better understanding of the complex antenna–plasma interactions.

Appendix A

Capacity Matrix Method for Conducting Body Surface

In order to obtain an equipotential solution on a conducting body, we use the Capacity Matrix method [*Hockney and Eastwood*, 1981]. The electrical potential ϕ and the charge density ρ on grid points within the computational space can be related by a matrix A as follows:

$$\rho_i = \sum_{j=1}^{N_\mathrm{G}} A_{ij}\phi_j, \quad (i = 1, \ldots, N_\mathrm{G}), \tag{A.1}$$

where i and j are the indices of the grid points, and N_G represents the total number of grid points. A is generally called a capacity matrix. Inversely, ϕ is calculated as

$$\phi_i = \sum_{j=1}^{N_\mathrm{G}} B_{ij}\rho_j, \quad (i = 1, \ldots, N_\mathrm{G}), \tag{A.2}$$

where $B = A^{-1}$.

When the surface charge on a conducting body is redistributed, only ρ_s, which is assigned on the body surface, is altered. The charge outside and inside the body is not changed. Therefore, the correction of the electrical potential $\delta\phi_\mathrm{s}$ is related to that of the charge density $\delta\rho_\mathrm{s}$ by

$$\delta\phi_{\mathrm{s},i} = \sum_{j=1}^{N_\mathrm{B}} B_{ij}\delta\rho_{\mathrm{s},j}, \quad (i = 1, \ldots, N_\mathrm{B}), \tag{A.3}$$

where N_B represents the total number of grid points on the conducting surface and $N_\mathrm{B} < N_\mathrm{G}$. Note that, although ϕ generally changes not only on the conducting surface but also outside the body, we focus on potential values only on the conducting surface in Eq. (A.3), because our goal is to control ϕ_s only on the surface for an equipotential solution. We here redefine a partial upper-left block of B with N_B rows and columns as a new matrix B'.

As a matrix inversion of B', we obtain a specialized capacity matrix C for the grids on the conducting surface. By using C, the relation between $\delta\phi_{\rm s}$ and $\delta\rho_{\rm s}$ is given by

$$\delta\rho_{{\rm s},i} = \sum_{j=1}^{N_{\rm B}} C_{ij}\delta\phi_{{\rm s},j}, \quad (i = 1, \ldots, N_{\rm B}). \tag{A.4}$$

In a simulation run, Eq. (A.4) is used to obtain the equipotential solution as described in Section 2.3.4. We should note that C_{ij} is generally not identical to the original matrix A_{ij}.

A straightforward way to obtain C is to place a unit charge on each grid on the conducting surface in turn with zero charge on the other grid points and solve for the potential. The obtained potential values form the elements of one column of B'. We repeat this process until all the elements of B' are obtained. Finally, C is computed by $C = B'^{-1}$. These processes are performed only once at the initialization of the simulation run.

Appendix B

Formulation of Antenna Conductance

In order to calculate the antenna conductance, we first formulate the currents carried by charged particles that impinge on or escape from the antenna surfaces as functions of the antenna potential V. In the presence of photoelectrons, we consider the currents of only background electrons and photoelectrons, and neglect the background ion current contribution. The magnitude of the currents is given as follows:

$$I_{\mathrm{ph}} = S_{\mathrm{ph}} e \Gamma_{\mathrm{ph}} \exp\left(-\frac{eV}{k_{\mathrm{B}} T_{\mathrm{ph}}}\right) \quad \text{(photoelectron)}, \tag{B.1}$$

$$I_{\mathrm{e}} = S n_0 e \sqrt{\frac{k_{\mathrm{B}} T_{\mathrm{e}}}{2\pi m_{\mathrm{e}}}} \frac{2}{\sqrt{\pi}} \sqrt{1 + \frac{eV}{k_{\mathrm{B}} T_{\mathrm{e}}}} \quad \text{(background electron)}, \tag{B.2}$$

where S_{ph} represents the area of antenna surface that emits photoelectrons. In the absence of photoelectrons, we consider the current balance between background electrons and ions. The current magnitude is given as

$$I_{\mathrm{e}} = S n_0 e \sqrt{\frac{k_{\mathrm{B}} T_{\mathrm{e}}}{2\pi m_{\mathrm{e}}}} \exp\left(\frac{eV}{k_{\mathrm{B}} T_{\mathrm{e}}}\right) \quad \text{(background electron)}, \tag{B.3}$$

$$I_{\mathrm{i}} = S n_0 e \sqrt{\frac{k_{\mathrm{B}} T_{\mathrm{i}}}{2\pi m_{\mathrm{i}}}} \frac{2}{\sqrt{\pi}} \sqrt{1 - \frac{eV}{k_{\mathrm{B}} T_{\mathrm{i}}}} \quad \text{(background ion)}, \tag{B.4}$$

where T_{i} represents the ion temperature. Here, we used the Orbital-Limited-Motion (OML) theory proposed by *Mott-Smith and Langmuir* [1926] and assumed that the antenna radius is smaller than the sheath thickness. In the above formulation, the expression (B.3) of the background electron current for the non-photoelectron case is different from equation (B.2) for the photoelectron case. This difference results from the fact that the antenna is negatively charged in the non-photoelectron case, whereas it is positively charged in the photoelectron case.

In the steady state of the plasma environment with an equilibrium floating antenna potential V_{f}, the above currents are balanced, i.e., the net current flow I into the antenna

is 0. The antenna conductance G represents how easily the current I is changed by a small applied variation of an antenna potential from V_f, and is given as $G = dI/dV|_{V=V_\mathrm{f}}$. By substituting equations (B.1)–(B.4) into $I = I_\mathrm{e} - I_\mathrm{ph}$ for the photoelectron case and $I = I_\mathrm{e} - I_\mathrm{i}$ for the non-photoelectron case, G is calculated as

$$\begin{aligned} G = \left.\frac{dI}{dV}\right|_{V=V_\mathrm{f}} &= \frac{Sn_0e^2}{k_\mathrm{B}T_\mathrm{e}}\sqrt{\frac{k_\mathrm{B}T_\mathrm{e}}{2\pi m_\mathrm{e}}}\frac{1}{\sqrt{\pi}}\left(1+\frac{eV_\mathrm{f}}{k_\mathrm{B}T_\mathrm{e}}\right)^{-\frac{1}{2}} + \frac{S_\mathrm{ph}e^2\Gamma_\mathrm{ph}}{k_\mathrm{B}T_\mathrm{ph}}\exp\left(-\frac{eV_\mathrm{f}}{k_\mathrm{B}T_\mathrm{ph}}\right) \\ &= \frac{1}{2}\frac{e}{k_\mathrm{B}T_\mathrm{e}+eV_\mathrm{f}}I_\mathrm{e}(V_\mathrm{f}) + \frac{e}{k_\mathrm{B}T_\mathrm{ph}}I_\mathrm{ph}(V_\mathrm{f}) \quad \text{(photoelectron case)}, \end{aligned} \tag{B.5}$$

$$\begin{aligned} G = \left.\frac{dI}{dV}\right|_{V=V_\mathrm{f}} &= \frac{Sn_0e^2}{k_\mathrm{B}T_\mathrm{e}}\sqrt{\frac{k_\mathrm{B}T_\mathrm{e}}{2\pi m_\mathrm{e}}}\exp\left(\frac{eV_\mathrm{f}}{k_\mathrm{B}T_\mathrm{e}}\right) + \frac{Sn_0e^2}{k_\mathrm{B}T_\mathrm{i}}\sqrt{\frac{k_\mathrm{B}T_\mathrm{i}}{2\pi m_\mathrm{i}}}\frac{1}{\sqrt{\pi}}\left(1-\frac{eV_\mathrm{f}}{k_\mathrm{B}T_\mathrm{i}}\right)^{-\frac{1}{2}} \\ &= \frac{e}{k_\mathrm{B}T_\mathrm{e}}I_\mathrm{e}(V_\mathrm{f}) + \frac{1}{2}\frac{e}{k_\mathrm{B}T_\mathrm{i}-eV_\mathrm{f}}I_\mathrm{i}(V_\mathrm{f}) \quad \text{(non-photoelectron case)}. \end{aligned} \tag{B.6}$$

These are analytical expressions of G for cases with and without photoelectron emission.

References

[1] Adachi, S., T. Ishizone, and Y. Mushiake (1977), Transmission line theory of antenna impedance in a magnetoplasma, *Radio Sci.*, *12*, 23–31, doi:10.1029/RS012i001p00023.

[2] Allcock, G. McK. (1957), A study of the audio-frequency radio phenomenon known as "dawn chorus", *Australian J. Phys.*, *10*, 286–298.

[3] Aso, T. (1973), A sheath resonance observed by a high frequency impedance probe, *J. Geomag. Geoelect.*, *25*, 325–330.

[4] Balmain, K. G. (1964), The impedance of a short dipole antenna in a magnetoplasma, *IEEE Trans. Antenna Propag.*, *AP-21*, 605–617, doi:10.1109/TAP.1964.1138278.

[5] Balmain, K. G. (1965), Impedance of a short dipole in a compressible plasma, *Radio Sci.*, *69D*, 559–566.

[6] Balmain, K. G., and G. A. Oksiutik (1969), RF probe admittance in the ionosphere: theory and experiment, in *Plasma Waves in Space and in the Laboratory*, vol. 1, edited by J. O. Thomas and B. J. Landmark, pp. 247–261, Edinburgh University Press, Edinburgh.

[7] Barrington, R. E., and J. S. Belrose (1963), Preliminary results from the very-low-frequency receiver aboard Canada's Alouette satellite, *Nature*, *198*, 651–656, doi:10.1038/198651a0.

[8] Béghin, C., and E. Kolesnikova (1998), Surface-charge distribution for modeling of quasi-static electric antennas in isotropic thermal plasma, *Radio Sci.*, *33*, 503–516, doi:10.1029/97RS03588.

[9] Béghin, C., P. M. E. Décréau, J. Pickett, D. Sundkvist, and B. Lefebvre (2005), Modeling of Cluster's electric antennas in space: Application to plasma diagnostics, *Radio Sci.*, *40*, RS6008, doi:10.1029/2005RS003264.

[10] Bell, T. F., U. S. Inan, and T. Chevalier (2006), Current distribution of a VLF electric dipole antenna in the plasmasphere, *Radio Sci.*, *41*, RS2009, doi:10.1029/2005RS003260.

[11] Birdsall, C. K., and A. B. Langdon (1985), *Plasma Physics via Computer Simulation*, McGraw-Hill, New York.

[12] Blomberg, L. G., H. Matsumoto, J.-L. Bougeret, H. Kojima, S. Yagitani, J. A. Cumnock, A. I. Eriksson, G. T. Marklund, J.-E. Wahlund, L. Bylander, L. Ahlen, J. A. Holtet, K. Ishisaka, E. Kallio, Y. Kasaba, A. Matsuoka, M. Moncuquet, K. Mursula, Y. Omura, and J. G. Trotignon (2006), MEFISTO - an electric field instrument for BepiColombo/MMO, *Adv. Space Res.*, *38*, 672–679, doi:10.1016/j.asr.2005.05.032.

[13] Boonzaaier, J. J., and C. W. I. Pistorius (1990), Thin wire dipoles - A finite-difference time-domain approach, *Electron. Lett.*, *26*, 1891-1892.

[14] Burton, E. T., and E. M. Boardman (1933), Audio-frequency atmospherics, *Proc. Institute of Radio Engineers*, *21*, 1476–1494.

[15] Calder, A. C., G. W. Hulbert, and J. G. Laframboise (1993), Sheath dynamics of electrodes stepped to large negative potentials, *Phys. Fluids B*, *5*(3), 674–690, doi:10.1063/1.860513.

[16] Cartwright, K. L., J. P. Verboncoeur, and C. K. Birdsall (2000), Loading and injection of Maxwellian distributions in particle simulations, *J. Comput. Phys.*, *162*, 483–613, doi:10.1006/jcph.2000.6549.

[17] Chugunov, Y. V., and V. Fiala (2006), Effective length of a receiving antenna in a streaming plasma, *IEEE Trans. Antennas Propag.*, *54*, 2750–2756, doi:10.1109/TAP.2006.882162.

[18] Cummer, S. A. (1997), An analysis of new and existing FDTD methods for isotropic cold plasma and a method for improving their accuracy, *IEEE Trans. Antennas Propag.*, *45*, 392–400, doi:10.1109/8.558654.

[19] Dawson, J. M. (1983), Particle simulation of plasmas, *Rev. Modern Phys.*, *55*, 403–447.

[20] Fahleson, U. (1967), Theory of electric field measurements conducted in the magnetosphere with electric probes, *Space Sci. Rev.*, *7*, 238–262, doi:10.1007/BF00215600.

[21] Forest, J., A. Hilgers, B. Thiebault, L. Eliasson, J.-J. Berthelier, and H. de Feraudy (2006), An open-source spacecraft plasma interaction simulation code PicUp3D: tests and validations, *IEEE Trans. Plasma Sci.*, *34*, 2103–2113, doi:10.1109/TPS.2006.883402.

[22] Fried, B. D., and S. D. Conte (1961), *The Plasma Dispersion Function: The Hilbert Transform of the Gaussian*, Academic Press, New York and London.

[23] Fujimoto, K., and S. Machida (2006), Electromagnetic full particle code with adaptive mesh refinement technique: Application to the current sheet evolution, *J. Comput. Phys.*, *214*, 550–566, doi:10.1016/j.jcp.2005.10.003.

[24] Fuselier, S. A., and D. A. Gurnett (1984), Short wavelength ion waves upstream of the Earth's bow shock, *J. Geophys. Res.*, *89*, 91–103, doi:10.1029/JA089iA01p00091.

[25] Garrett, H. B. (1981), The charging of spacecraft surfaces, *Rev. Geophys. Space. Phys.*, *19*, 577–616, doi:10.1029/RG019i004p00577.

[26] Garrett, H. B., and A. C. Whittlesey (2000), Spacecraft charging, an update, *IEEE Trans. Plasma Sci.*, *28*, 2017–2028, doi:10.1109/27.902229.

[27] Grard, R. J. L. (1973), Properties of the satellite photoelectron sheath derived from photoemission laboratory measurements, *J. Geophys. Res.*, *78*, 2885–2906, doi:10.1029/JA078i016p02885.

[28] Gurnett, D. A., and R. R. Shaw (1973), Electromagnetic radiation trapped in the magnetosphere above plasma frequency, *J. Geophys. Res.*, *78*, 8236–8249.

[29] Gurnett, D. A. (1974), The Earth as a radio source: Terrestrial kilometric radiation, *J. Geophys. Res.*, *79*, 4227–4238, doi:10.1029/JA079i028p04227.

[30] Gurnett, D. A. (1998), Principles of space plasma wave instrument design, in *Measurement Techniques in Space Plasmas – Fields*, edited by R. F. Pfaff et al., pp. 121–136, AGU, Washington, D. C.

[31] Gustafsson, G., M. André, T. Carozzi, A. I. Eriksson, C.-G. Fälthammar, R. Grard, G. Holmgren, J. A. Holtet, N. Ivchenko, T. Karlsson, Y. Khotyaintsev, S. Klimov, H. Laakso, P.-A. Lindqvist, B. Lybekk, G. Marklund, F. Mozer, K. Mursula, A. Pedersen, B. Popielawska, S. Savin, K. Stasiewicz, P. Tanskanen, A. Vaivads and J.-E. Wahlund (2001), First results of electric field and density observations by Cluster EFW based on initial months of operation, *Ann. Geophys.*, *19*, 1219–1241.

[32] Harrington, R. F. (1968), *Field Computation by Moment Methods*, Wiley–IEEE Press, New York.

[33] Hashimoto, K., I. Nagano, T. Okada, M. Yamamoto, and I. Kimura (1991), Antenna vector impedance measurement by the EXOS-D (Akebono) Very Low Frequency Plasma Wave Instrument (VLF), *Geophys. Res. Lett.*, *18*, 313–316, doi:10.1029/91GL00035.

[34] Hastings, D., and H. Garrett (1996), *Spacecraft–Environment Interactions*, Cambridge Univ. Press, Cambridge, U. K.

[35] Hershkowitz, N. (1989), How Langmuir probes work, in *Plasma Diafnostics*, vol. 1, edited by O. Auciello and D. L. Flamm, pp. 113–184, Academic, San Diego.

[36] Hockney, R. W., and J. W. Eastwood (1981), *Computer Simulation Using Particles*, McGraw-Hill, New York.

[37] Hunsberger, F., R. Luebbers, and K. Kunz (1992), Finite-difference time-domain analysis of gyrotropic media. I - Magnetized plasma, *IEEE Trans. Antennas Propag.*, *40*, 1489–1495, doi:10.1109/8.204739.

[38] Imachi, T., S. Yagitani, I. Nagano, M. Tsutsui, and H. Matsumoto (2002), Effective Lengths of the Electric Antennas Aboard GEOTAIL Spacecraft, *IEICE Trans. B (in Japanese)*, *J85-B*, 97–104.

[39] Imachi, T., S. Yagitani, R. Higashi, and I. Nagano (2007), Rheometry experiment for a wire antenna aboard spacecraft at low frequencies, *Elect. Commun. Jpn. (Part I: Communications)*, *90*, 45–53, doi:10.1002/ecja.20353.

[40] Inan, U. S., T. F. Bell, J. Bortnik, and J. M. Albert (2003), Controlled precipitation of radiation belt electrons, *J. Geophys. Res.*, *108*(A5), 1186, doi:10.1029/2002JA009580.

[41] Ishisaka, K. (2000), Analysis of GEOTAIL spacecraft potentials and its applications to the magnetospheric plasma diagnostic, Ph.D. thesis (in Japanese), Toyama Pref. Univ., Toyama, Japan.

[42] Ishizone, T., S. Adachi, and Y. Mushiake (1976), Reciprocity relations in an isotropic compressible multifluid plasma, *J. Appl. Phys.*, *47*, 2918–2922, doi:10.1063/1.323073.

[43] James, H. G. (2000), Electrostatic resonance-cone waves emitted by a dipole in the Ionosphere, *IEEE Trans. Antennas Propag.*, *48*, 1340–1348, doi:10.1109/8.898766.

[44] Jordan, E. C. (1950), *Electromagnetic Waves and Radiating Systems*, Prentice-Hall, Englewood Cliffs, N. J.

[45] Kafafy, R., and J. Wang (2006), A hybrid grid immersed finite element particle-in-cell algorithm for modeling spacecraft plasma interactions, *IEEE Trans. Plasma Sci.*, *34*, 2114–2124, doi:10.1109/TPS.2006.883404.

[46] Kojima, H. (1998), Study on the plasma waves in the geomagnetic tail region, Ph.D. thesis, Kyoto Univ., Kyoto, Japan.

[47] Kuehl, H. H. (1966), Resistance of a short antenna in a warm plasma, *Radio Sci.*, *1*, 971–976.

[48] Kuehl, H. H. (1967), Computations of the resistance of a short antenna in a warm plasma, *Radio Sci.*, *2*, 73–76.

[49] Laframboise, L. G. (1966), Theory of spherical and cylindrical Langmuir probes in a collisionless, Maxwellian plasma at rest, Ph.D. thesis, Univ. of Toronto, Toronto, Canada.

[50] Laurin, J.-J., G. A. Morin, and K. G. Balmain (1989), Sheath wave propagation in a magnetoplasma, *Radio Sci.*, *24*, 289–300, doi:10.1029/RS024i003p00289.

[51] Lieberman, M. A., and A. J. Lichtenberg (1994), *Principles of Plasma Dischages and Materials Processing*, Wiley-Interscience, New York.

[52] Luebbers, R., F. Hunsberger, and K. S. Kunz (1991), A frequency-dependent finite-difference time-domain formulation for transient propagation in plasma, *IEEE Trans. Antennas Propag.*, *39*, 29-34, doi:10.1109/8.64431.

[53] Luebbers, R., L. Chen, T. Uno, and S. Adachi (1992), FDTD calculation of radiation patterns, impedance and gain for a monopole antenna on a conducting box, *IEEE Trans. Antennas Propag.*, *40*, 1577–1583, doi:10.1109/8.204752.

[54] Lui, A. T. Y. (1987), *Magnetotail Physics*, *The Johns Hopkins University Press*, Baltimore and London.

[55] Lüttgen, A. A. E., and K. G. Balmain (1996), Nonreciprocal magnetoplasma sheath waves, *Radio Sci.*, *31*, 1599–1614, doi:10.1029/96RS02193.

[56] Mandell, M. J., V. A. Davis, D. L. Cooke, A. T. Wheelock, and C. J. Roth (2006), Nascap-2k spacecraft charging code overview, *IEEE Trans. Plasma Sci.*, *34*, 2084–2093, doi:10.1109/TPS.2006.881934.

[57] Martin, A. R. (1994), A review of spacecraft/plasma interactions and effects on space systems, *J. Br. Interplanet. Soc.*, *47*, 134–142.

[58] Matsumoto, H., and Y. Omura (1993), *Computer Space Plasma Physics*, Terra Scientific, Tokyo.

[59] Matsumoto, H., H. Kojima, T. Miyatake, Y. Omura, M. Okada, I. Nagano, and M. Tsutsui (1994a), Plasma wave observations with Geotail spacecraft, *J. Geomag. Geoelectr.*, *46*, 59–95.

[60] Matsumoto, H., H. Kojima, T. Miyatake, Y. Omura, M. Okada, I. Nagano, and M. Tsutsui (1994b), Electrostatic solitary waves (ESW) in the magnetotail: BEN wave forms observed by GEOTAIL, *Geophys. Res. Lett.*, *21*(25), 2915–2918.

[61] Meyer, P., and N. Vernet (1974), Impedance of a short antenna in a warm magnetoplasma, *Radio Sci.*, *9*, 409–416, doi:10.1029/RS009i003p00409.

[62] Meyer, P., N. Vernet, and P. Lassudrie-Duchesne (1974), Theoretical and experimental study of the effect of the sheath on an antenna immersed in a warm isotropic plasma, *J. Appl. Phys.*, *45*, 700-706.

[63] Meyer-Vernet, N., and C. Perche (1989), Tool kit for antennae and thermal noise near the plasma frequency, *J. Geophys. Res.*, *94*, 2405–2415, doi:10.1029/JA094iA03p02405.

[64] Meyer-Vernet, N., S. Hoang, K. Issautier, M. Maksimovic, R. Manning, M. Moncuquet, and R. G. Stone (1998), Measuring plasma parameters with thermal noise spectroscopy, in *Measurement Techniques in Space Plasmas – Fields*, edited by R. F. Pfaff et al., pp. 205–210, AGU, Washington, D. C.

[65] Miyake, Y., H. Usui, H. Kojima, Y. Omura, and H. Matsumoto (2008a), Electromagnetic Particle-In-Cell simulation on the impedance of a dipole antenna surrounded by an ion sheath, *Radio Sci.*, *43*, RS3004, doi:10.1029/2007RS003707.

[66] Miyake, Y., and H. Usui (2008b), Analysis of photoelectron effect on the antenna impedance via Particle-In-Cell simulation, *Radio Sci.*, *43*, RS4006, doi:10.1029/2007RS003776.

[67] Miyake, Y., H. Usui, H. Kojima, and Y. Omura (2008c), Particle-In-Cell simulation on the characteristics of a receiving antenna in space plasma environment, *Proc. 26th Int. Sympo. on RGD*, *1084*, 895–900.

[68] Miyake, Y., and H. Usui (2008d), New electromagnetic particle simulation code for the analysis of spacecraft-plasma interactions, submitted to *Phys. Plasmas*.

[69] Morin, G. A., and K. G. Balmain (1991), Hydrodynamic radio-frequency model of an ion sheath near a conductor in a plasma, *Radio Sci.*, *26*, 459–467, doi:10.1029/90RS02757.

[70] Mott-Smith, H. M., and I. Langmuir (1926), The theory of collectors in gaseous discharges, *Phys. Rev.*, *28*, 727–763.

[71] Muranaka, T., S. Hosoda, J. Kim, S. Hatta, K. Ikeda, T. Hasegawa, M. Cho, H. Usui, H. O. Ueda, K. Koga, and T. Goka (2008), Development of Multi-Utility Spacecraft Charging Analysis Tool (MUSCAT), *IEEE Trans. Plasma Sci.*, *36*, 2336–2349, doi:10.1109/TPS.2008.2003974.

[72] Nakagawa, T., T. Ishii, K. Tsuruda, H. Hayakawa, and T. Mukai (2000), Net current density of photoelectrons emitted from the surface of the GEOTAIL spacecraft, *Earth Planets Space*, *52*, 283–292,.

[73] Nakatani, D. T., and H. H. Kuehl (1976), Input impedance of a short dipole antenna in a warm anisotropic plasma. I - Kinetic theory, *Radio Sci.*, *11*, 433–444, doi:10.1029/RS011i005p00433.

[74] Okada, T., K. Ishisaka, T. Mukai, K. Tsuruda, and H. Matsumoto (2000), Study of magnetospheric structure of electron density using correlation between spacecraft potential and electron density, *IEICE Trans. B* (in Japanese), *J83-B*, 885–893.

[75] Olson, J. (2006), Modeling of the MEFISTO antenna on BepiColombo, Master thesis, Royal Inst. Tech., Stockholm, Sweden.

[76] Omura, Y. (1985), Study on nonlinear wave–particle interactions in space plasmas via computer simulations, Ph.D. thesis, Kyoto Univ., Kyoto, Japan.

[77] Oya, H. (1965), Effect of resonances on the admittance of an RF plasma probe surrounded by an ion sheath, *Rep. Ionos. Space Res. Jpn.*, *19*, 243–271.

[78] Oya, H. (1966), Study on boundary value problems of magneto-active plasma and their applications to space observation, Ph.D. thesis, Kyoto Univ., Kyoto, Japan.

[79] Oya, H., and T. Obayashi (1966), Measurement of ionospheric electron density by a Gyro-Plasma Probe: A rocket experiment by a new impedance probe, *Rep. Ionos. Space Res. Jpn.*, *20*, 199–213.

[80] Oya, H., and T. Aso (1969), Ionospheric electron temperature measured by a gyro-plasma probe, in *Space Res. IX*, pp. 287–296, North-Holland Publishing Company, Amsterdam.

[81] Pedersen, A. and C. A. Cattell, C.-G. Fälthammar, V. Formisano, P.-A. Lindqvist, F. Mozer, and R. Torbert (1984), Quasistatic electric field measurements with spherical double probes on the GEOS and ISEE satellites, *Space Sci. Rev.*, *37*, 269–312, doi:10.1007/BF00226365.

[82] Pedersen, A., F. Mozer, and G. Gustafsson (1998), Electric field measurements in a tenuous plasma with spherical double probes, in *Measurement Techniques in Space Plasmas – Fields*, edited by R. F. Pfaff et al., pp. 1–12, AGU, Washington, D. C.

[83] Preece, W. H. (1894), Earth currents, *Nature*, *49*(1276), 554, doi:10.1038/049554b0.

[84] Roussel, J.-F., F. Rogier, G. Dufour, J.-C. Matéo-Vélez, J. Forest, A. Hilgers, D. Rodgers, L. Girard, and D. Payan (2008), SPIS open-source code: Methods, capabilities, achievements, and prospects, *IEEE Trans. Plasma Sci.*, *36*, 2360–2368, doi:10.1109/TPS.2008.2002327.

[85] Schelkunoff, S. A., and H. T. Friis (1952), *Antennas; Theory and Practice*, John Wiley and Sons, New York.

[86] Schiff, M. L. (1970), Impedance of a short dipole antenna in a warm isotropic plasma, *Radio Sci.*, *5*, 1489–1496.

[87] Schiff, M. L., and J. A. Fejer (1970), Impedance of antennas in a warm isotropic plasma: A comparison of different models, *Radio Sci.*, *5*, 811–819, doi:10.1029/RS005i005p00811.

[88] Schmidt, R., and A. Pedersen (1987), Long-term behaviour of photo-electron emission from the electric field double probe sensors on GEOS-2, *Planet. Space Sci.*, *35*, 61–70, doi:10.1016/0032-0633(87)90145-0.

[89] Schwartz, S. J., T. Horbury, C. Owen, W. Baumjohann, R. Nakamura P. Canu, A. Roux, F. Sahraoui, P. Louarn, J.-A. Sauvaud, J.-L. Pinçon, A. Vaivads, M. F. Marcucci, A. Anastasiadis, M. Fujimoto, P. Escoubet, M. Taylor, S. Eckersley, E. Allouis, and M.-C. Perkinson (2008), Cross-scale: multi-scale coupling in space plasmas, *Exp. Astronomy*, 3–, doi:10.1007/s10686-008-9085-x.

[90] Smith, J. R., N. Hershkowitz, and P. Coakley (1979), Inflection-point method of interpreting emissive probe characteristics, *Rev. Sci. Instrum.*, *50*, 210–218.

[91] Sonwalkar, V. S., and U. S. Inan (1986), Measurements of Siple transmitter signals on the DE 1 satellite: Wave normal direction and antenna effective length, *J. Geophys. Res.*, *91*, 154–164, doi:10.1029/JA091iA01p00154.

[92] Spencer, E., S. Patra, T. Andriyas, C. Swenson, J. Ward, and A. Barjatya (2008), Electron density and electron neutral collision frequency in the ionosphere using plasma impedance probe measurements, *J. Geophys. Res.*, *113*, A09305, doi:10.1029/2007JA013004.

[93] Stix, T. H. (1992), *Waves in Plasmas*, American Institute of Physics, New York.

[94] Storey, L. R. O. (1953), An investigation of whistling atmospherics, *Phil. Trans. Roy. Soc.*, *246*, 113–141.

[95] Stutzman, W. L., and G. A. Thiele (1997), *Antenna Theory and Design*, 2nd ed., Wiley, New York.

[96] Taflove, A. (1995), *Computational Electrodynamics: The Finite-Difference-Time-Domain Method*, Artech House, Norwood, MA.

[97] Tajima, T., and Y. C. Lee (1981), Absorbing boundary condition and Budden turning point technique for electromagnetic plasma simulation, *J. Comput. Phys.*, *42*, 406–413, doi:10.1016/0021-9991(81)90254-0.

[98] Tsutsui, M., I. Nagano, H. Kojima, K. Hashimoto, H. Matsumoto, S. Yagitani, and T. Okada, (1997), Measurements and analysis of antenna impedance aboard the Geotail spacecraft, *Radio Sci.*, *32*, 1101–1126, doi:10.1029/97RS00396.

[99] Tu, J., P. Song, and B. W. Reinisch (2008), Plasma sheath structures around a radio frequency antenna, *J. Geophys. Res.*, *113*, A7223, doi:10.1029/2008JA013097.

[100] Ueda, H., Y. Omura, H. Matsumoto, and T. Okuzawa (1994), A study of the numerical heating in electrostatic particle simulations, *Comput. Phys. Commun.*, *79*, 249–259, doi:10.1016/0010-4655(94)90071-X.

[101] Umeda, T., Y. Omura, T. Tominaga, and H. Matsumoto (2003), A new charge conservation method in electromagnetic particle-in-cell simulations, *Comput. Phys. Commun.*, *156*, 73–85, doi:10.1016/S0010-4655(03)00437-5.

[102] Uno, T. (1998), *Finite Difference Time Domain method for electromagnetics and antennas*, Corona Pub. Co. Ltd., Tokyo (in Japanese).

[103] Usui, H. (1993), Study on the electrodynamic interaction between a tethered satellite system and space plasma, Ph.D thesis, Kyoto Univ., Kyoto, Japan.

[104] Usui, H., H. Matsumoto, K. Miyata, and Y. Omura (2004), Computer experiments on electromagnetic environment of plasma sheath at conducting surface, *Adv. Space Res.*, *34* , 2441–2444.

[105] Usui, H., Y. Miyake, M. Okada, Y. Omura, T. Sugiyama, K. T. Murata, D. Matsuoka, and H. O. Ueda, (2006), Development and application of Geospace Environment Simulator for the analysis of spacecraft–plasma interactions, *IEEE Trans. Plasma Sci.*, *34*, 2094–2102, doi:10.1109/TPS.2006.883290.

[106] Wakabayashi, M., and T. Ono (2006), Electron density measurement under the influence of auroral precipitation and electron beam injection during the DELTA campaign, *Earth, Planets, and Space*, *58*, 1147–1154, doi:10.1109/TAP.2005.851823.

[107] Ward, J., C. Swenson, and C. Furse (2005), The impedance of a short dipole antenna in a magnetized plasma via a finite difference time domain model, *IEEE Trans. Antenna Propag.*, *53*, 2711–2718, doi:10.1109/TAP.2005.851823.

[108] Whipple, E. C. (1981), Potentials of surfaces in space, *Rep. Prog. Phys.*, *44*, 1197–1250.

[109] Yee, K. S. (1966), Numerical solution of initial boundary value problems involving Maxwell's equations in isotropic media, *IEEE Trans. Antennas Propag.*, *14*, 302–307, doi:10.1109/TAP.1966.1138693.

Publication List

Major Publications

1. Usui, H., Y. Miyake, M. Okada, Y. Omura, T. Sugiyama, K. T. Murata, D. Matsuoka, and H. O. Ueda, Development and application of Geospace Environment Simulator for the analysis of spacecraft–plasma interactions, *IEEE Transactions on Plasma Science*, *34*(5), 2094-2102, doi:10.1109/TPS.2006.883290, 2006.

2. Miyake, Y., H. Usui, H. Kojima, Y. Omura, and H. Matsumoto, Electromagnetic Particle-In-Cell simulation on the impedance of a dipole antenna surrounded by an ion sheath, *Radio Science*, *43*, RS3004, doi:10.1029/2007RS003707, 2008.

3. Miyake, Y. and H. Usui, Analysis of photoelectron effect on the antenna impedance via Particle-In-Cell simulation, *Radio Science*, *43*, RS4006, doi:10.1029/2007RS003776, 2008.

4. Usui, H., Y. Sugisaki, S. Tomita, Y. Omura, Y. Miyake, M. Aoki, OpenMP parallelization method for current calculation in plasma particle simulation, *IPSJ Transaction on Advanced Computing Systems*, *1*(2), IPSJ-TACS0102024, 250–260, 2008.

5. Miyake, Y. and H. Usui, New electromagnetic particle simulation code for the analysis of spacecraft-plasma interactions, *Physics of Plasmas*, submitted, 2008.

Refereed Symposium Proceeding

1. Miyake, Y. and H. Usui, Particle-In-Cell simulation on the characteristics of a receiving antenna in space plasma environment, *Proceedings of 26th International Symposium on Rarefied Gas Dynamics (RGD)*, *1084*, 895–900, 2008.

Presentations in International Meetings

1. Miyake, Y., H. Usui, H. Kojima, and H. Matsumoto, Particle-In-Cell simulations on electric field antenna characteristics in space plasma, *7th International School/ Symposium for Space Plasma Simulations (ISSS)*, Kyoto, Mar. 2005.

2. Miyake, Y., H. Usui, H. Kojima, and H. Matsumoto, Particle-In-Cell simulations on electric field antenna characteristics in space plasma, *28th General Assembly of the International Union of Radio Science (URSI)*, New Delhi, India, Oct. 2005.

3. Miyake, Y., H. Usui, H. Kojima, Y. Omura, and H. Matsumoto, Particle-In-Cell simulations on the characteristics of electric field antenna in the spacecraft environment, *36th Scientific Assembly of Committee on Space Research (COSPAR)*, Beijing, China, Jul. 2006.

4. Miyake, Y., H. Usui, H. Kojima, Y. Omura, and H. Matsumoto, Computer experiments on the characteristics of electric field antenna in the spacecraft environment, *Inter-COE International Symposium on Energy System*, Tokyo, Oct. 2006.

5. Miyake, Y., H. Usui, H. Kojima, Y. Omura, and H. Matsumoto, Particle-In-Cell simulations on electric field antenna characteristics in the spacecraft environment, *American Geophysical Union (AGU) Fall Meeting*, San Francisco, USA, Dec. 2006.

6. Miyake, Y., H. Usui, H. Kojima, Y. Omura, and H. Matsumoto, Effect of photoelectrons on the impedance of an electric field antenna in the spacecraft environment, *8th ISSS*, Hawaii, USA, Feb. 2007.

7. Miyake, Y., H. Usui, H. Kojima, Y. Omura, and H. Matsumoto, Effect of photoelectrons on the impedance of the electric field antennas onboard spacecraft: EM-PIC simulation analysis, *24th General Assembly of International Union of Geophysics and Geodesy (IUGG)*, Perugia, Italy, Jul. 2007.

8. Miyake, Y., H. Usui, H. Kojima, Y. Omura, and H. Matsumoto, Effect of photoelectrons on the impedance of electric field antenna onboard spacecraft, *2007 International Symposium on Antennas and Propagation (ISAP)*, Niigata, Aug. 2007.

9. Miyake, Y., H. Usui, H. Kojima, and Y. Omura, EM-PIC simulation analysis on the characteristics of satellite-onboard antenna in space plasma, *Climate and Weather of the Sun-Earth System (CAWSES) International Symposium*, Kyoto, Oct. 2007.

10. Miyake, Y., H. Usui, H. Kojima, and Y. Omura, Numerical analysis on electric field antennas in space plasma environment via electromagnetic Particle-In-Cell simulation, *AGU Fall Meeting*, San Francisco, USA, Dec. 2007.

11. Miyake, Y., H. Usui, H. Kojima, and Y. Omura, Particle-In-Cell simulation on the effective length of a receiving antenna in space plasma environment, *Asia Oceania Geosciences Society (AOGS) 6th Annual General Meeting*, Busan, Korea, Jun. 2008.

12. Miyake, Y., H. Usui, H. Kojima, and Y. Omura, Particle-In-Cell simulation on the characteristics of a receiving antenna in space plasma environment, *26th RGD Symposium*, Kyoto, Jul. 2008.

13. Miyake, Y., H. Usui, H. Kojima, and Y. Omura, Analysis of receiving antenna characteristics in space plasma environment via particle-in-cell simulation, *29th URSI General Assembly*, Chicago, USA, Aug. 2008.

Awards

1. "URSI Young Scientist Award", Particle-In-Cell simulations on electric field antenna characteristics in space plasma, *28th URSI General Assembly*, 2005.

2. "AGU Outstanding Student Paper Award", Numerical analysis on electric field antennas in space plasma environment via electromagnetic Particle-In-Cell simulation, *2007 AGU Fall Meeting*, 2008.

3. "SGEPSS Student Presentation Award (Aurora Medal)", PIC Simulation on the characteristics of an electric field antenna for future magnetospheric mission (in Japanese), *124th Society of Geomagnetism and Earth, Planetary and Space Sciences (SGEPSS) Fall Meeting*, 2008.